

**ELECTRONIC AND STRUCTURAL  
PROPERTIES OF TWO DIMENSIONAL  
SEMICONDUCTORS AND OXIDES**

**THESIS SUBMITTED TO  
THE UNIVERSITY OF CALCUTTA  
FOR THE DEGREE OF  
DOCTOR OF PHILOSOPHY (SCIENCE)  
IN  
PHYSICS(THEORETICAL)  
SEPTEMBER, 2015**

**By**

**RUMA DAS**

**S. N. BOSE NATIONAL CENTRE FOR BASIC SCIENCES**

**JD BLOCK, SECTOR-III, SALLAKE**

**KOLKATA 700 098, INDIA**

**Dedicated to**  
**My Husband and Friends**

# Acknowledgement

I have spent more than six years as a Ph.D. student at S. N. Bose Centre (SNB) and this journey could not have been so enjoyable without continuous guidance, support, help and mentorship both related to work and personally from many individuals. Though words are not enough to express my gratitude to all those who have helped me in their own way, I would like to take this opportunity to express my sincere thanks to all of them.

First and foremost, I would like to extend my heartiest gratitude to my supervisor Prof. Priya Mahadevan for her continuous mentoring, supervising and guidance in the right direction throughout the period of my Ph.D. I have learnt a lot from her and without her valuable suggestions and help, I could not have finished my thesis successfully. Her vast scientific knowledge and insight into various problems always motivated me in the field of Nano science. The knowledge and exposures which I have gained from her will surely help me to grow in my research career.

I always enjoyed working in a group like PMG and I would like thank my current group members- Saikat (one day junior to me), Basudeb, Shishir, Sagar, Poonam (caring sister) and Joydeep as well as my seniors- Hirak da, Abhinav da, Bipul Da, Kapil da, Ashis da, Ravi not only for their support and contribution in my work but also for the nice time we have spent at bay, tea-break and treats. Thanks to Saikat and Shishir for technical support. I got many new ideas while presenting my works during the group-talks which have helped me to enrich my clarity and conceptualize the overall thought process towards the topics I have worked. I will specially remember the care which they have shown to me till date.

Now I would like to thank those people who have made me feel like a “Second Home” during my stay at SNB. The first name come to my mind is Ruma (Mandal), one of my best friends who has always supported me. I have also spent good times with Putul, Soma, Dilip, Anuradha, Tamisra, Rajasree, Semanti, Sandeep (Sing) da, Jena da, Rajiv da, Arka da and Prashant da.

Thanks to all of them for creating such joyfull and homelike environment which was beyond expectation. Among the non-academic staffs, Kakoli di will always be remembered. Apart from SNB friends I also thank Priyanka for supporting me as well. My journey at SNB would not have been so memorable and enjoyable without all of their presence and I will cherish all these wonderfull memories forever.

Now I would like to thank the computer centre of SNB as well as PMG, ATHENA, AMRU, HPC and PHOTON for the computational facilities. My sincere thanks go to Council of Scientific and Industrial Research (CSIR), Government of India for financial support.

Last but not the least I would like to thank my parents, brother, Bapi da and husband who were always with me throughout this journey. Special thanks to my beloved husband who has continuously supported me in every aspect from the first to the last day of Ph.D..

Ruma Das

Kolkata, India

September, 2015

# List of Publications

1. Effective mass driven structural transition in Mn-doped ZnS nanoplatelet, Celine Gerard\*, **Ruma Das**\*, Priya Mahadevan and D. D. Sarma, J. Phys. Chem. Lett. **4**, 1023 (2013).  
(\* = Equal contribution)
2. 3-D to 1-D quantum confinement in ZnS nanoplatelets as a function of lateral dimension, **Ruma Das** and Priya Mahadevan (Manuscript under preparation).
3. A microscopic model for the strain driven direct to indirect band gap transition in monolayer MoS<sub>2</sub> and ZnO, **Ruma Das**, Bipul Rakshit, Saikat Debnath and Priya Mahadevan, Phys. Rev. B **89**, 115201 (2014).
4. A model for the direct to indirect band gap transition in monolayer MoSe<sub>2</sub> under strain, **Ruma Das** and Priya Mahadevan, Pramana- J. Phys. **84**, 1033 (2015).
5. Understanding of the changeover from direct to indirect band gap in MoSe<sub>2</sub> and MoS<sub>2</sub> as a function of thickness, **Ruma Das** and Priya Mahadevan (Manuscript under preparation).

# Contents

<b>List of Figures</b>	<b>xvii</b>
<b>List of Tables</b>	<b>xx</b>
<b>1 Introduction</b>	<b>1</b>
<b>2 Theoretical Background</b>	<b>15</b>
2.1 Introduction to the Many Particle Hamiltonian . . . . .	15
2.2 Born-Oppenheimer (B-O) Approximation . . . . .	16
2.3 Single Particle Approximation . . . . .	17
2.4 The Hartree Approximation . . . . .	17
2.5 The Hartree-Fock Approximation . . . . .	18
2.6 The Correlation Energy . . . . .	20
2.7 The Density Functional Theory . . . . .	20
2.8 The Hohenberg-Kohn Theorems . . . . .	21
2.9 Kohn-Sham Formulation of Density Functional Theory . . . . .	24
2.10 The Exchange-Correlation Approximations . . . . .	27

2.10.1	The Local Density Approximation (LDA) . . . . .	27
2.10.2	The Generalized Gradient Approximation (GGA) . . . . .	29
2.10.3	The Hybrid Functional . . . . .	30
2.11	Methods for Electronic Structure Calculations . . . . .	30
2.11.1	Plane Wave Pseudopotential Method . . . . .	31
2.11.2	Projector Augmented Waves (PAWs) Method . . . . .	35
2.11.3	The Tight-Binding Approximation . . . . .	36
2.11.4	Wannier Functions . . . . .	39
<b>3</b>	<b>Effective Mass Driven Structural Transition in a Mn-Doped ZnS Nanoplatelet</b>	<b>43</b>
3.1	Introduction . . . . .	43
3.2	Methodology . . . . .	45
3.3	Results and Discussion . . . . .	47
3.4	Conclusion . . . . .	53
<b>4</b>	<b>3-D to 1-D Quantum Confinement in ZnS Nanoplatelets as a Function of Lateral Dimension</b>	<b>57</b>
4.1	Introduction . . . . .	57
4.2	Methodology . . . . .	58
4.3	Results and Discussion . . . . .	64
4.4	Conclusion . . . . .	73

<b>5</b>	<b>A Microscopic Model for the Strain Driven Direct to Indirect Band gap Transition in Monolayer MoS<sub>2</sub> and ZnO</b>	<b>76</b>
5.1	Introduction . . . . .	76
5.2	Methodology . . . . .	78
5.3	Results and Discussions . . . . .	80
5.4	Conclusion . . . . .	92
<b>6</b>	<b>A Model for the Direct to Indirect Band gap Transition in Monolayer MoSe<sub>2</sub> as a Function of Strain</b>	<b>95</b>
6.1	Introduction . . . . .	95
6.2	Methodology . . . . .	97
6.3	Results and Discussion . . . . .	98
6.4	Conclusion . . . . .	104
<b>7</b>	<b>Understanding of the Changeover from Direct to Indirect Band Gap in MoSe<sub>2</sub> and MoS<sub>2</sub> as a Function of Thickness</b>	<b>107</b>
7.1	Introduction . . . . .	107
7.2	Methodology . . . . .	109
7.3	Results and Discussion . . . . .	112
7.4	Conclusion . . . . .	128

# List of Figures

1.1	variation of percentage of bulk and surface atoms as a function of particle size of nanomaterials [8]. . . . .	2
1.2	Wave functions and energy levels of a particle in a box. The figure is adapted from [13]. . . . .	3
1.3	Different emission colors from different sizes of CdSe nanoparticles. The nanoparticles were capped with ZnSe. (Adapted from [15]). . . . .	4
1.4	Evolution of the density of states with dimensionality showing the variation of density of states with energy for the infinite bulk solid, a quantum film, a quantum wire and a quantum dot [8]. . . . .	5
1.5	Structure of Graphene. . . . .	6
1.6	Crystal structure of MoS <sub>2</sub> where Mo and S atoms are shown by violet and yellow. . . . .	7
2.1	Schematic representation of the construction of the pseudo-wave function $\phi(\mathbf{r})$ and pseudopotential $V^{PS}(\mathbf{r})$ , beginning with the real valence wave function $\phi(\mathbf{r})$ and Coulomb potential $V^{Coul}(\mathbf{r})$ ; ( $R_c$ ) is the cutoff radius beyond which the wave function and potential are not affected (taken from Atomic and Electronic Structure of Solids, E Kaxiras, Cambridge University Press) [8]. . . . .	34

3.1	(a) Wurtzite $\langle 0001 \rangle$ and (b) zinc blende $\langle 110 \rangle$ ZnS nanoplatelets of medium size. Magenta, cyan and red atoms are the Zn atoms which are 0, 1 and 2-fold coordinated with pseudo-hydrogens. . . . .	47
3.2	Charge density of Mn majority spin antibonding levels with $t_2$ symmetry for (a) wurtzite (wz) and zinc blende $\langle 110 \rangle$ (zb110) nanoplatelet and (b) wurtzite (wz) and zinc blende (zb) of bulk ZnS as a function of the distance from Mn along the Mn-S bond-length. In the inset the difference of the wz and zinc blende charge density of the respective graph is shown. It should be noted that since the charge density along a short distance of the bond is given, charge conservation doesnt seem to be apparent from the figure. . . . .	50
3.3	Movement of VBMs of wurtzite $\langle 0001 \rangle$ and zinc blende $\langle 110 \rangle$ due to quantum confinement effect. . . . .	53
4.1	Crystal structure of wz $\langle 0001 \rangle$ ZnS nanoplatelets. Zn, S and pseudo-hydrogens are shown by magenta, green and orange colours respectively. . . . .	59
4.2	Crystal structure of zb $\langle 001 \rangle$ ZnS nanoplatelets. Zn, S and pseudo-hydrogens are shown by magenta, green and orange colours respectively. . . . .	59
4.3	Crystal structure of zb $\langle 1\bar{1}0 \rangle$ ZnS nanoplatelets. Zn, S and pseudo-hydrogens are shown by magenta, green and orange colours respectively. . . . .	59
4.4	The atom and angular momentum projected partial density of states for Zn and S atoms of bulk wurtzite ZnS from <i>ab-initio</i> calculations using LDA potentials. Zero of energy corresponds to the Fermi energy. . . . .	62
4.5	The atom and angular momentum projected partial density of states for Zn and S atoms of bulk zinc blende ZnS from <i>ab-initio</i> calculations using LDA potentials. Zero of energy corresponds to the Fermi energy. . . . .	62

4.6	Comparison of <i>ab-initio</i> band dispersions (blue solid line) for bulk wurtzite ZnS at its experimental lattice constant, using hybrid functionals and the fitted tight binding bands (red line with circles), using a basis consisting of Zn <i>s,p,d</i> and S <i>s,p,d</i> states. The zero of energy is the valence band maximum. . . . .	65
4.7	Comparison of <i>ab-initio</i> band dispersions (blue solid line) for bulk zinc blende ZnS at its experimental lattice constant, using hybrid functionals and the fitted tight binding bands (red line with circles), using a basis consisting of Zn <i>s,p,d</i> and S <i>s,p,d</i> states. The zero of energy is the valence band maximum. . . . .	65
4.8	The density of states (DOS) of wz⟨0001⟩ with radius 4 Å and thickness 4 monolayer from <i>ab-initio</i> calculations using hybrid functionals (a) and from tight binding calculation (b). Zero of energy corresponds to the is the valence band maximum. 69	69
4.9	The density of states (DOS) of zb⟨11̄0⟩ with radius 4 Å and thickness 4 monolayer from <i>ab-initio</i> calculations using hybrid functionals (a) and from tight binding calculation (b). Zero of energy corresponds to the is the valence band maximum. 69	69
4.10	Variation of band gap of wz⟨0001⟩ nanoplatelets with respect to the bulk band gap as a function of their lateral dimension for thicknesses of 2,4 6 and 8-monolayers In the inset the variation of band gaps shift is shown by subtracting the band gap at Bohr exciton radius ( $E_B$ ). . . . .	71
4.11	Variation of band gap of zb⟨001⟩ nanoplatelet with respect to the bulk band gap as a function of it's lateral dimension for thickness of 4-monolayer. . . . .	72
4.12	Variation of band gap of zb⟨11̄0⟩ nanoplatelet with respect to the bulk band gap as a function of it's lateral dimension for thickness of 4-monolayer. . . . .	72
5.1	The atom and angular momentum projected partial density of states for (a) Mo and (b) S atoms from <i>ab-initio</i> calculations using GGA potentials. Zero of energy corresponds to the Fermi energy. . . . .	79

5.2	Crystal structure of a monolayer of MoS <sub>2</sub> where Mo and S atoms are shown by green and magenta colours. . . . .	80
5.3	<i>Ab-initio</i> band dispersions (solid line) for monolayer MoS <sub>2</sub> at its experimental lattice constant (0% biaxial tensile strain), using GGA potentials. The fitted tight binding bands (dashed line), using a basis consisting of Mo <i>d</i> and S <i>p</i> have been superposed. Here the radial part of the tight binding basis functions correspond to maximally localized Wannier functions. The zero of energy is the valence band maximum. . . . .	80
5.4	The charge density plot for monolayer MoS <sub>2</sub> for the highest occupied band at (a) $\Gamma$ and (b) at $\mathbf{K}$ symmetry points obtained from <i>ab-initio</i> calculations using GGA potentials at 0% strain. . . . .	81
5.5	<i>Ab-initio</i> band dispersions (solid line) for monolayer MoS <sub>2</sub> at its experimental lattice constant (2% biaxial tensile strain), using GGA potentials. The fitted tight binding bands (dashed line), using a basis consisting of Mo <i>d</i> and S <i>p</i> have been superposed. Here the radial part of the tight binding basis functions correspond to maximally localized Wannier functions. The zero of energy is the valence band maximum. . . . .	82
5.6	Comparison of <i>ab-initio</i> band dispersions (solid line) for monolayer MoS <sub>2</sub> at its experimental lattice constant(0% biaxial tensile strain), using GGA potentials and the fitted tight binding bands (dashed line), using a basis consisting of Mo <i>s,p,d</i> and S <i>s,p,d</i> states. The zero of energy is the valence band maximum. . . .	84
5.7	Comparison of <i>ab-initio</i> band dispersions (solid line) for monolayer MoS <sub>2</sub> at its experimental lattice constant(2% biaxial tensile strain), using GGA potentials and the fitted tight binding bands (dashed line), using a basis consisting of Mo <i>s,p,d</i> and S <i>s,p,d</i> states. The zero of energy is the valence band maximum. . . .	84
5.8	Crystal structure of a monolayer of ZnO where Zn and O atoms are shown by green and red colours. . . . .	88

5.9	<i>Ab-initio</i> band dispersions for monolayer ZnO within LDA+ <i>U</i> , <i>U</i> =8 eV at its experimental lattice constant. The zero of energy is the valence band maximum.	89
5.10	The charge density plot for monolayer ZnO for the highest occupied band at (a) $\Gamma$ and (b) at $\mathbf{K}$ high symmetry points. obtained from <i>ab-initio</i> calculations using LDA+ <i>U</i> , <i>U</i> =8 eV potentials at 0% strain. . . . .	89
5.11	The variation of the direct and the indirect band gap for monolayer ZnO at various biaxial tensile strain obtained within <i>ab-initio</i> calculations using LDA+ <i>U</i> , <i>U</i> =8 eV potentials. . . . .	90
5.12	The calculated phonon dispersion for ZnO at 10% biaxial tensile strain along various symmetry directions. . . . .	91
6.1	The atom and angular momentum projected partial density of states for Mo and Se atoms from <i>ab-initio</i> calculations using GGA potentials at 0% strain. The zero of energy corresponds to the valence band maximum. . . . .	97
6.2	Crystal structure of a monolayer of MoSe <sub>2</sub> . . . . .	98
6.3	Comparison of <i>ab-initio</i> band dispersions (solid line) for monolayer MoSe <sub>2</sub> at its experimental lattice constant(0 % biaxial tensile strain), using GGA potentials and the fitted tight binding bands (dashed line), using a basis consisting of Mo <i>s,p,d</i> and Se <i>s,p,d</i> states. The zero of energy corresponds to the valence band maximum. . . . .	99
6.4	The charge density plot for monolayer MoSe <sub>2</sub> for the highest occupied band at $\mathbf{K}$ point obtained from <i>ab-initio</i> calculations using GGA potentials at 0 % strain. .	100
6.5	The charge density plot for monolayer MoSe <sub>2</sub> for the highest occupied band at $\Gamma$ point obtained from <i>ab-initio</i> calculations using GGA potentials at 0 % strain.	100

6.6	Comparison of <i>ab-initio</i> band dispersions for monolayer MoSe <sub>2</sub> at its experimental lattice constant at 0 % biaxial tensile strain (solid line) and 3 % biaxial tensile strain (dashed line) using GGA potentials. The zero of energy corresponds to the valence band maximum. . . . .	102
6.7	Comparison of <i>ab-initio</i> band dispersions (solid line) for monolayer MoSe <sub>2</sub> at its experimental lattice constant(3 % biaxial tensile strain), using GGA potentials and the fitted tight binding bands (dashed line), using a basis consisting of Mo <i>s,p,d</i> and Se <i>s,p,d</i> states. The zero of energy corresponds to the valence band maximum. . . . .	103
7.1	Crystal structure of a 2H bilayer of MoSe <sub>2</sub> where magenta and green atoms are Mo and Se atoms respectively. In this figure (a) and (b) show the top and side view of this structure and (c) shows the unit cell. . . . .	110
7.2	The atom and angular momentum projected partial density of states for Mo and Se atoms from <i>ab-initio</i> calculations using GGA potentials. Zero of energy corresponds to the Fermi energy. . . . .	111
7.3	The <i>ab-initio</i> band dispersion for monolayer MoSe <sub>2</sub> at it's experimental lattice constant using GGA potentials. The arrow indicates that band gap is direct. The zero of energy is the valence band maximum. . . . .	113
7.4	The <i>ab-initio</i> band dispersion for bilayer MoSe <sub>2</sub> at it's experimental lattice constant using GGA potentials. The arrow indicates that band gap is indirect. The zero of energy is the valence band maximum. . . . .	114
7.5	The <i>ab-initio</i> band dispersion for bilayer MoSe <sub>2</sub> at it's experimental lattice constant using LDA potentials. The arrow indicates that band gap is indirect. The zero of energy is the valence band maximum. . . . .	114

7.6	Comparison of <i>ab-initio</i> band dispersions for monolayer MoSe <sub>2</sub> (black solid line) and bilayer MoSe <sub>2</sub> (red dashed line) at it's experimental lattice constant using GGA potentials. The zero of energy is the valence band maximum. . . . .	115
7.7	The charge density plot for bilayer MoSe <sub>2</sub> for the highest occupied band at (a) $\Gamma$ and and for the lowest unoccupied band at (b) $\mathbf{K}$ and (c) $\mathbf{T}$ symmetry points obtained from <i>ab-initio</i> calculations using GGA potentials. . . . .	116
7.8	Comparison of <i>ab-initio</i> band dispersions (black solid lines) for monolayer MoSe <sub>2</sub> at it's experimental lattice constant, using GGA potentials and the fitted tight binding bands (line with red circle), using a basis consisting of Mo <i>d</i> and Se <i>p</i> states. Here the radial part of the tight binding basis functions correspond to maximally localized Wannier functions. The zero of energy is the valence band maximum. . . . .	118
7.9	Comparison of <i>ab-initio</i> band dispersions (black solid line) for bilayer MoSe <sub>2</sub> at it's experimental lattice constant, using GGA potentials and the fitted tight binding bands (line with red circle), using a basis consisting of Mo <i>d</i> and Se <i>p</i> states. Here the radial part of the tight binding basis functions correspond to maximally localized Wannier functions. The zero of energy is the valence band maximum. . . . .	118
7.10	Comparison of <i>ab-initio</i> band dispersion of monolayer MoSe <sub>2</sub> (black solid line) at it's experimental lattice constant, using GGA potentials and band structure of bilayer MoSe <sub>2</sub> (red line) when the inter-layer hopping interactions are switched off. The zero of energy is the valence band maximum. . . . .	120
7.11	Comparison of <i>ab-initio</i> band dispersions (black solid line) for monolayer MoSe <sub>2</sub> at it's experimental lattice constant using GGA potentials and the fitted tight binding bands (red dashed line), using a basis consisting of Mo <i>s,p,d</i> and Se <i>s,p,d</i> states. The zero of energy is the valence band maximum. . . . .	121

7.12	Comparison of <i>ab-initio</i> band dispersions (black solid line) for bilayer MoSe <sub>2</sub> at it's experimental lattice constant using GGA potentials and the fitted tight binding bands (red dashed line), using a basis consisting of Mo <i>s,p,d</i> and Se <i>s,p,d</i> states. The zero of energy is the valence band maximum. . . . .	121
7.13	The <i>ab-initio</i> band dispersion for monolayer MoS <sub>2</sub> at it's experimental lattice constant using GGA potentials. The arrow indicates that band gap is direct. The zero of energy is the valence band maximum. . . . .	123
7.14	The <i>ab-initio</i> band dispersion for bilayer MoS <sub>2</sub> at it's experimental lattice constant using GGA potentials. The arrow indicates that band gap is indirect. The zero of energy is the valence band maximum. . . . .	124
7.15	The <i>ab-initio</i> band dispersion for bilayer MoS <sub>2</sub> at it's experimental lattice constant using LDA potentials. The arrow indicates that band gap is indirect. The zero of energy is the valence band maximum. . . . .	124
7.16	Comparison of <i>ab-initio</i> band dispersions for monolayer MoS <sub>2</sub> (black solid line) and bilayer MoS <sub>2</sub> (red dashed line) at it's experimental lattice constant using GGA potentials. The zero of energy is the valence band maximum. . . . .	125
7.17	Comparison of <i>ab-initio</i> band dispersions (black solid line) for monolayer MoS <sub>2</sub> at it's experimental lattice constant, using GGA potentials and the fitted tight binding bands (line with red circle), using a basis consisting of Mo <i>d</i> and S <i>p</i> states. Here the radial part of the tight binding basis functions correspond to maximally localized Wannier functions. The zero of energy is the valence band maximum. . . . .	126

7.18 Comparison of <i>ab-initio</i> band dispersions (black solid line) for bilayer MoS <sub>2</sub> at its experimental lattice constant, using GGA potentials and the fitted tight binding bands (line with red circle), using a basis consisting of Mo <i>d</i> and S <i>p</i> states. Here the radial part of the tight binding basis functions correspond to maximally localized Wannier functions. The zero of energy is the valence band maximum. . . . .	126
7.19 Comparison of <i>ab-initio</i> band dispersion (red dashed line) for monolayer MoS <sub>2</sub> at its experimental lattice constant, using GGA potentials and the bilayer bands (magenta line) when the inter-layer hopping interactions are switched off. The zero of energy is the valence band maximum. . . . .	127

# List of Tables

3.1	Relative binding energy of Mn at the most stable sites for different sizes of ZnS nanoplatelets with respect to corresponding wurtzite phase. . . . .	48
3.2	Positions of VBM of different sizes of nanoplatelets of ZnS as well as that bulk ZnS. The relative shifts of the VBM in the case of the wurtzite and zinc blende nanodisks with respect to the bulk values for the same structure have been provided in parentheses. . . . .	52
4.1	The radius ( $r$ ) and the corresponding number of atoms ( $N$ ) for all the ZnS nanoplatelets with 4-monolayer in thickness considered in our study. . . . .	61
4.2	Band gaps for different ZnS nanoplatelets with 4-monolayer in thickness considered in our study at different radii as well as the bulk band gaps from <i>ab-initio</i> calculations using LDA for the exchange-correlation functional. In brackets the <i>ab-initio</i> band gaps are given using hybrid functionals. The energies are in eV. . . . .	64
4.3	Parameters obtained from least-square error fitting of the <i>ab-initio</i> using hybrid functional band structure onto a tight binding model using $s, p, d$ orbitals of Zn and S for bulk wurtzite of ZnS. The energies are in eV. . . . .	67
4.4	Parameters obtained from least-square error fitting of the <i>ab-initio</i> using hybrid functional band structure onto a tight binding model using $s, p, d$ orbitals of Zn and S for bulk zinc blende of ZnS. The energies are in eV. . . . .	68

4.5	Parameters obtained from the fitting of the <i>ab-initio</i> band gap using hybrid functional to a tight binding model using <i>s, p</i> orbitals of Zn and S atoms and <i>s</i> orbital for pseudo-hydrogens (H1 and H2) for wurtzite and zinc blende nanoplatelets of ZnS. The energies are in eV. . . . .	70
5.1	Parameters obtained from least-square error fitting of the <i>ab-initio</i> band structure onto a tight binding model using <i>s, p, d</i> orbitals of Mo and S for monolayer MoS <sub>2</sub> at 0% biaxial tensile strain. The energies are in eV. . . . .	86
5.2	Parameters obtained from least-square error fitting of the <i>ab-initio</i> band structure onto a tight binding model using <i>s, p, d</i> orbitals of Mo and S for monolayer MoS <sub>2</sub> at 2% biaxial tensile strain. The energies are in eV. . . . .	87
5.3	Strain percentage at which the band gap crossover takes place and the energy difference of the VBM/CBM at $\Gamma$ ( $E(\Gamma)$ ) and $\mathbf{K}$ ( $E(\mathbf{K})$ ) at 0% strain of MoSe <sub>2</sub> , WSe <sub>2</sub> and BN monolayer. The energies are in eV. . . . .	91
6.1	Parameters obtained from least-squared-error fitting of the <i>ab-initio</i> band structure onto a tight binding model using <i>s, p, d</i> orbitals of Mo and Se for monolayer MoSe <sub>2</sub> at 0 % biaxial tensile strain. The energies are in eV. . . . .	101
6.2	The onsite energies obtained from least-squared-error fitting of the <i>ab-initio</i> band structure onto a tight binding model using <i>s, p, d</i> orbitals of Mo and Se for monolayer MoSe <sub>2</sub> at 3 % biaxial tensile strain. The energies are in eV. . . . .	104
7.1	Onsite energies obtained from tight binding fitting of the <i>ab-initio</i> band structure a basis consisting of Mo <i>d</i> and Se <i>p</i> for monolayer and bilayer MoSe <sub>2</sub> . The respective Se <i>p<sub>x</sub></i> is taken as reference for this energies and these in eV. . . . .	119

7.2 Parameters obtained from least-square-error fitting of the *ab-initio* band structure onto a tight binding model using *s, p, d* orbitals of Mo and Se for bilayer MoSe<sub>2</sub>. The radial part of the tight binding basis functions correspond to maximally localized Wannier functions. The distances between the neighbors are given in brackets in unit of Å. The energies (E) are in eV. . . . . 122

# Chapter 1

## Introduction

In the past few decades, modern research has acquired a new direction which is “nanoscale science and technology” [1] [2]. This area of research is driven by the ability to fabricate, model and manipulate objects with small number of atoms which has led to the investigation of material properties close to the atomic level. In electronics industry, the basic units of integrated circuits and storage media are approaching the size of few tens of nanometers. This trend of miniaturization has opened the door to new technologies for the fabrication of new materials and new devices. This class of materials is called “nanomaterials” which are sized between one to few tens of nm in atleast one dimension. In this size range, the nanomaterials frequently exhibit new properties at a level intermediate between atomic/molecular and bulk. They enter into a size regime where the properties of the materials become dependent on the size. Michael Faraday provided the first description of the changes in the optical properties of materials with the size in his classic paper in 1857 [3]. This makes them a very important class of materials to study. The variation of various material properties such as electric transport [4], field emission [5] and the Youngs modulus [6] have been studied at the nanosized regime. Nanomaterials have been successfully applied to technological roles, for example logic gates have been fabricated using semiconductor nanowire junctions [7], and have been shown to be capable of basic computation [7]. Gold nanostructures are very useful for early detection and

treatment of cancer. The interesting properties of nanomaterials have been praised with many great promising applications in near future.

The origin of this unique properties of nanomaterials which are entirely different from their bulk and those of a single atom are due to two reasons: the first one is the surface effect and the other one is the quantum confinement effect. Nanomaterials present an extremely high surface to volume ratio [9]. So, a large percentage of the atoms in this material is on its surface compared to it's bulk which is shown in Fig. 1.1. It is well known that surface atoms play an important role in governing the electronic, optical and thermodynamic properties in materials. As a result of this, the overall properties of the crystal is influenced. Since the percentage of surface atoms depends considerably on the size of the particle, it can give rise to size effects in physical and chemical properties such as chemical reactivity of these materials. For example, bulk cadmium sulfide has a melting point of about 1600 °C, whereas a nanocrystal with radii 25 Å of the same material has a melting temperature of about 400 °C [10].

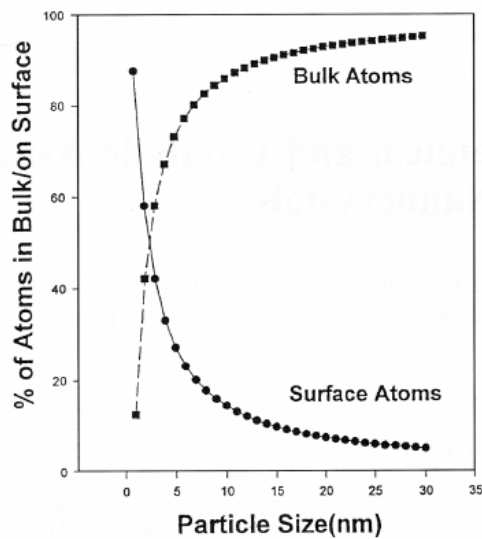


Figure 1.1: variation of percentage of bulk and surface atoms as a function of particle size of nanomaterials [8].

In semiconductors, electronic and optical properties change drastically below a critical size limit which depends on the material composition [11]. This size limit is comparable to the

Bohr exciton radius. In a semiconductor, an electron and a hole are formed upon excitation across the band gap and this bound state of an electron-hole pair due to a Coulomb interaction between them is called exciton. The average separation between the electron and the hole in the exciton is known as the Bohr exciton radius. In bulk semiconductors, the exciton can move freely in all directions. As the size of the material is reduced below this Bohr exciton radius, the electron and hole, confined in a space, cannot however be considered as independent particles and the exciton nature is enhanced. In addition, the wave function of the electron and hole feel the the effect of the boundary. As a result, the electronic energy levels get modified. This phenomenon is called quantum confinement [12].

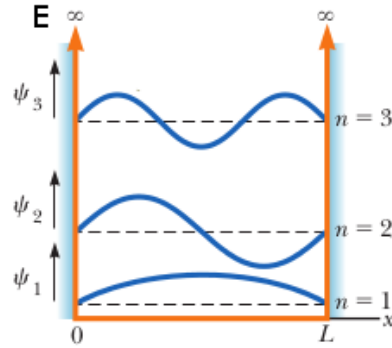


Figure 1.2: Wave functions and energy levels of a particle in a box. The figure is adapted from [13].

Particle-in-a-box treatment provides a simple way to understand the effect shown in Fig. 1.2. For this case, the eigen functions obtained by solving the Schrödinger equation are,

$$\Psi_n(x) = \sqrt{\frac{1}{2L}} \sin(k_n x), k_n = \frac{\pi n}{L} \quad (1.1)$$

and the corresponding eigen values are,

$$E_n = \frac{\hbar^2 k_n^2}{2m} = \frac{\hbar^2 \pi^2 n^2}{2mL^2} \quad (1.2)$$

More reduction in box size ( $L$ ) results in more confined electron-hole pairs which leads to a larger separation between the individual energy levels since it is inversely proportional to  $L^2$ . This effect is primarily driven by effective masses ( $m$ ) of electrons and holes. As a result of this effect, band gap of a semiconductor increases [14]. The size dependent band gap can be a useful tool for designing materials with well controlled-optical properties. The band gap variation with size has been confirmed with different semiconductor nanomaterial systems. One example of different sizes of CdSe nanoparticles capped with ZnSe is shown in Figure 1.3. The blue light emitting particles have the highest band gap as the particles size are the smallest in this case. The red light emitting particles have the smallest band gap because of the larger particle size. The size of the particles can be tuned in such a way that all the possible visible colors can be achieved.



Figure 1.3: Different emission colors from different sizes of CdSe nanoparticles. The nanoparticles were capped with ZnSe. (Adapted from [15]).

In nanoscale regime, dimensionality is one of the critical parameters to modulate physical and chemical properties of nanomaterials [16]. According to the direction of confinement of charge carriers nanomaterials can be classified into categories of two-dimensional films (2-D) [17], one-dimensional (1-D) [18] quantum wires and zero-dimensional (0-D) quantum dots or nanocrystals [19]. In two-dimensional nanomaterials, carriers are confined in only one direction which results in a dramatic change in the density of states from bulk. While going from 3-D (bulk) to 2-D, the density of state is recognized into steps shown in Fig. 1.4. In 1-D quantum wire, carriers can move freely only in one direction as now they are confined in two directions.

Finally in zero -dimensional quantum dot, carriers are confined in all three directions. The corresponding density of states for 1-D and 0-D nanomaterials are shown in the Fig. 1.4 which are drastically different from 3-D (bulk). In the present thesis, we focus on materials that are confined only in the one dimension i.e. 2-D quantum films or platelets.

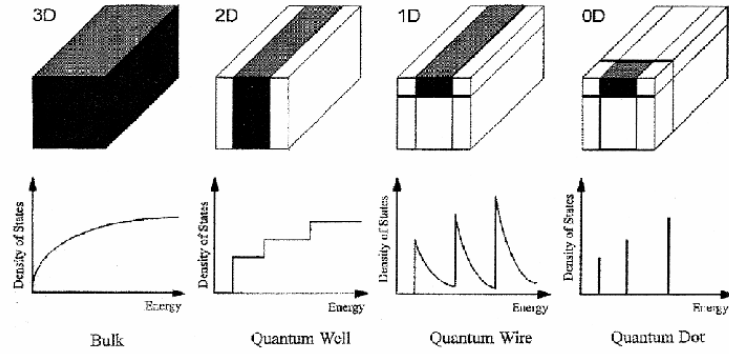


Figure 1.4: Evolution of the density of states with dimensionality showing the variation of density of states with energy for the infinite bulk solid, a quantum film, a quantum wire and a quantum dot [8].

Until now, most research on dimensionality controlled studies has been concentrated on the zero-dimensional quantum dot and one-dimensional quantum wires. Two-dimensionality in nanomaterials is emerging fast, exhibiting unexpected new phenomena which are absent from other dimensionalities. According to the early report of Geim and Novoselov and co-workers in 2004 [20], graphene is the first isolated two-dimensional nanomaterials with one-atom thick planar sheet of  $sp^2$ -bonded carbon in hexagonal structure arranged in a densely packed 2-D honeycomb lattice shown in Fig. 1.5 which has rapidly risen to be one of the hottest topics in materials science due to its fascinating properties and great potential applications. Owing to its zero band gap, super thin and flat structure, graphene exhibits remarkable electronic, thermal, optical and mechanical properties, such as superior thermal conductivity (  $5000 \text{ W m}^{-1} \text{ K}^{-1}$ ) [21], high optical transmittance (97.7%) [22], extremely high Young's modulus (  $1.1 \text{ TPa}$ ) [23] and fracture strength (125 GPa) [23], specific surface area (theoretically,  $2630 \text{ m}^2 \text{ g}^{-1}$ ) [24], high chemical stability, as well as excellent transport phenomena such as the quantum Hall effect [25] and ambipolar electric field effect. These intriguing properties endow graphene-

based materials with many applications, such as in ultra-strong lightweight components used in space shuttles to improve fuel efficiency. As a promising nanomaterial, graphene can also be used in catalysis, sensors, bio medicine and in reinforced composites [24]. The development of graphene will undoubtedly not only cause a revolution in understanding the fundamental properties of two dimensional structural materials with delocalized electrons, but will also transform the technology dramatically in future. However, the absence of a band gap has limited its applications and shifted the focus onto several layered transition metal disulphides and diselenides such as  $\text{MoS}_2$ ,  $\text{WSe}_2$  etc. colloidal nanoplatelets and monolayers of BN, ZnO etc.

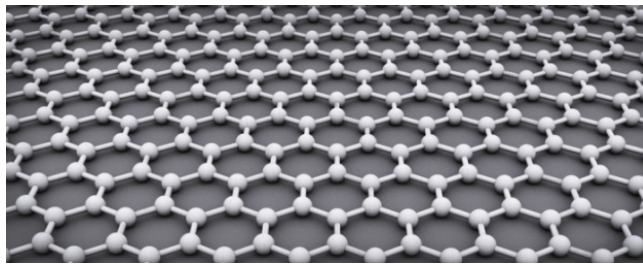


Figure 1.5: Structure of Graphene.

Similar to graphene, these two-dimensional transition metal dichalcogenides of  $\text{MX}_2$  type where M stands for the transition metal elements and X for the chalcogen elements ( $\text{M} = \text{Mo}, \text{W}, \text{Ti}$  etc.,  $\text{X} = \text{S}, \text{Se}$ , etc.) are based on the typical layered-structured compounds whose layers are bound by weak van der Waals forces. As an example of these materials, crystal structure of Molybdenum disulphide ( $\text{MoS}_2$ ) is shown in Fig. 1.6. Atomic scale thickness endows these two-dimensional semiconductors with peculiar and fascinating properties in contrast with those of their bulk parent compounds such as band gap crossover from direct to indirect band gap takes place as a function of strain [26] and thickness [27]. Such material characteristics can also be complementary to what is lacking from graphene which is essential for energy harvesting applications. However, this field is not well developed due to several experimental challenges and the lack of our understanding of their intrinsic properties.

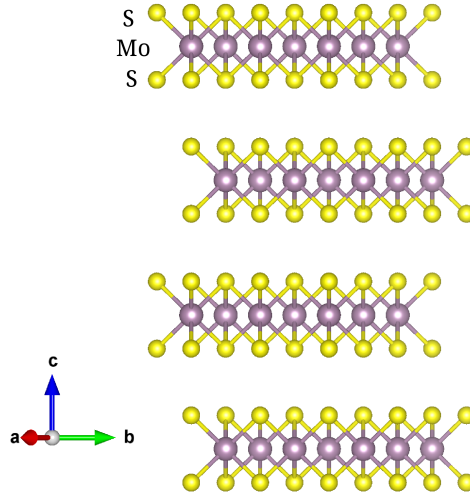


Figure 1.6: Crystal structure of MoS<sub>2</sub> where Mo and S atoms are shown by violet and yellow.

Apart from the transition metal dichalcogenides, two-dimensional colloidal anisotropic inorganic crystal nanostructures, with a thickness ( $<10$  nm) much smaller than their lateral dimensions (that can reach several micrometers), called nanoplatelets have recently emerged as a novel class of materials with exotic properties which are very useful in electronic and optical device applications [28] [29] [30]. There are enough reports on the synthesis and characterization of zero-dimensional quantum dots [31] and one-dimensional quantum wires and tubes [32] in the literature and they are well studied theoretically [33] as well as experimentally [34]. However, there are only few examples of the synthesis of the ultrathin 2-D colloidal nanoparticles with a strong motivation to develop new types of devices [35], such as the Bloch oscillator or quantum well lasers. Since then, new ultrathin 2-D nanoparticles such as metals (Ag [36], Au [37]), semiconductors [38] [39], metal oxides [40] etc. have been synthesized. 2-D semiconducting nanomaterials have acquired much more attention due to their optical properties useful for various industrial applications such as lasers and infrared detectors.

Earlier two-dimensional heterostructures of semiconductors were grown on a substrate using techniques such as beam epitaxy (MBE) [41], metal organic chemical vapor deposition (MOCVD) [42] [43], metal-organic vapor-phase epitaxy (MOVPE) [44]. The processing cost

in these cases were high, in addition to the fact that the films could not be separated from the substrate. The substrate has the disadvantage of limiting the process ability of the ultra-thin semiconductor layers, especially when assembly or orientation control is desired. Recently, nanoplatelets have been synthesized in free-standing form [45] [46] [47] which have the advantage of manipulating them without their substrate. Freestanding structures with 2-D geometry can be obtained using various techniques. For example, Ithurria and Dubertret have [48] grown 2-D colloidal CdSe nanoplatelets having zinc blende crystal structure in free-standing form. These nanoplatelets have lateral dimensions from 6 to 40 nm and thickness is found to be  $2.2 \pm 0.3$  nm observed in TEM images. In this process, the shape, aspect ratio and thickness of the platelets can be controlled by varying various reaction conditions.

Effective mass approximation (EMA) by Efros and Efros [49] was the the first theoretical approach for the explanation of quantum confinement effect on band gap as a function of size. In this approximation, the effective mass equation is solved variationally considering various choice of electron and hole wave functions. According to Brus [50], in the strong confinement regime, where the radius of a spherical nanocrystals is much smaller than the Bohr exciton radius, the band gap of a nanocrystal is inversely proportional to it's radius. This model is improved by Einevoll [51] and Nair *et al.* [52] considering bond-orbital model for hole wave function as the valence band of II-VI semiconductors is comprised of triply degenerate bands at  $\Gamma$  point whereas the electron wave function is described by a single band EMA. Even with these improvements, this model has some drawback due to the adjustments of finite potential for every system. There are other theoretical approaches which demonstrate the variation of band gap with size like *ab-initio* method [53], *k·p* [54], empirical pseudopotential method [55] [56], empirical tight binding method [17] [57] [58] etc. In *ab-initio* method, calculation of nanosystems is restricted to small sizes  $\sim 200$ -500 atoms. This limits the use of *ab-initio* calculations to only small sizes of clusters. Continuum models such as effective mass and *k·p*, ignore atomistic effects. Atomistic effects are included in empirical pseudopotential method as well as empirical tight binding method. We shall focus on the empirical tight binding method which we have used in parts of the thesis. Here a set of atomic orbitals are considered on each atom. The orbitals that are chosen in this model are those which contribute to the valence band. The onsite energies

as well as hopping interaction strengths are determined by fitting the *ab-initio* band structure along various symmetry directions.

In this thesis, I have studied the electronic and structural properties of two-dimensional semiconductors and oxides. The techniques that I have used to carry out our analysis includes a combination of *ab-initio* electronic structure calculations as well as model Hamiltonian methods. I have developed a code for real space tight binding model for nanostructures as well as several other codes for the analysis of the results during my PhD. My work is mainly focused on the study of various aspects of two-dimensional semiconductors such as nano-platelets of ZnS, monolayers and bilayers of MoS<sub>2</sub> and MoSe<sub>2</sub> and monolayer of ZnO. In **Chapter 2**, I have discussed the fundamental methods used in the electronic structure calculations performed in this thesis. We started with the many body Hamiltonian and discussed different approximations and approaches which are useful to understand the basic principles on which density function theory works.

Among binary semiconductors (III-V and II-VI groups), one finds that the more ionic members favor the wurtzite structure, while the covalent ones are found to favor the zinc blende form, with the other form (zinc blende and wurtzite, respectively) being available as a metastable state with an energy only a few meV per atom higher than the ground state. Since physical and chemical properties of any material depend critically on the specific crystal structure, such a low-lying metastable state holds out the interesting possibility of tilting the energy balance in favor of the metastable phase even under small perturbations, thereby drastically altering material properties. In **Chapter 3** we have shown that Mn doping in ZnS nanoplatelets can induce a structural transition from the wurtzite to the zinc blende phase. In order to understand the microscopic origin of such an unusual phase transformation, we use first principle electronic structure calculations carried out within the framework of density functional theory. Our results show that at a fundamental level, quantum confinement effects at the nanoscale are responsible for the observed phenomenon, the two structure types being discriminated by Mn incorporation/ejection essentially due to significantly different hole effective masses in the zinc blende and wurtzite phases. Our results also explain the absence of any such structural transformation above a certain size of the nanocrystal.

In **Chapter 4** we have considered a real space tight binding model to study the size dependence of the band gap of ZnS nanoplatelets. Confinement in both the lateral directions as well as the vertical direction have been examined. Although one has small variations in the band gap as the Bohr exciton radius of ZnS is approached in the lateral direction, significant changes in the band gap are seen due to confinement in the growth direction. We consider platelets with different number of layers in the growth direction and show that subtracting out the contribution from confinement in the growth direction results in the curves collapsing onto each other. This indicates the separability of the potential in the growth direction present even in a fully atomistic calculation.

At the monolayer limit both MoS<sub>2</sub> and the graphitic phase of ZnO have a direct band gap. Biaxial tensile strain has been found to induce a transition into an indirect band gap semiconductor with the strain percentage required for the transition equal to 0.83% for MoS<sub>2</sub> and 8% for ZnO, respectively. A low strain percentage is desirable for possible device applications. In **Chapter 5** we identify a simple design principle which could be used to identify materials requiring a small strain to induce such a transition. A scaling of the hopping interaction strengths according to Harrison's law within a tight binding model for MoS<sub>2</sub> is able to capture the effect. Similar analysis has been done in **Chapter 6** for MoSe<sub>2</sub>, which also shows that a modest biaxial tensile strain of 3% can drive it into an indirect band gap semiconductor with the valence band maximum (VBM) shifting from **K** point to **Γ** point.

In **Chapter 7** we have examined the electronic structure of a monolayer as well as a bilayer of MoS<sub>2</sub> and MoSe<sub>2</sub>. While a monolayer is found to be a direct band gap semiconductor in both systems, the bilayer has been found to be an indirect band gap semiconductor. As these materials are van der Waals heterostructures, inter-layer interaction is expected to be weak. Considering a tight binding model we are able to reproduce the band structure calculated within *ab-initio* calculations. Using the extracted parameters, we are able to determine the contribution from inter-layer interactions and charge transfer effects leading to the observed band gap variations.

# Bibliography

- [1] N. Lane, *Journal of Nanoparticle Research* **3**, 95 (2001).
- [2] R. F. Service, *Science* **290**, 1526 (2000).
- [3] M. Faraday, *Phil. Trans. Roy. Soc. London* **147**, 145 (1857).
- [4] Y. Xia, P. Yang, P. Sun, Y. Wu *et al.*, *Adv. Mater.* **15**, 353 (2003).
- [5] J. Tian, C. Hui, L. Bao *et al.*, *App. Phys. Lett.* **94**, 083101 (2009).
- [6] L. Calbri, N. Pugno, W. Ding *et al.*, *J. of Phys.: Cond. Matt.* **18**, 2175 (2006).
- [7] Y. Huang, X. Duan, Y. Cui *et al.*, *Science* **294**, 1313 (2001).
- [8] K. J. Klabunde and R. M. Richards, *Nanoscale Materials in Chemistry*, Wiley, (2001).
- [9] Günter and Schmid, *Nanoparticle: From Theory to Application*, Wiley-VCH, Germany (2004).
- [10] R. Elghanian, J. J. Storhoff, R. C. Mucic *et al.*, *Science* **277**, 1078 (1997).
- [11] C. Delerue and M. Lannoo, *Nanostructures: Theory and Modeling*, Springer (2004).
- [12] P. Harrison, *Quantum wells, wires and dots: Theoretical and computational physics*, John Wiley & Sons, USA (2000).
- [13] R.A. Serway, J. John, W. Jewett *et al.*, *Physics for Scientists and Engineers* (2010).
- [14] A. L. Efros and M. Rosen, *Annu. Rev. Mater. Sci.* **30**, 475 (2000).

- [15] B. O. Dabbousi, J. Rodriguez-Viejo, F. V. Mikulec *et al.*, J. Phys. Chem., **101**, 9463 (1997).
- [16] S. Kan, T. Mokari, E. Rothenberg *et al.*, Nat. Mater. **2**, 155 (2003).
- [17] G. Bastard, *Wave Mechanics Applied to Semiconductor Heterostructures*, Les Editions de Physique, Paris (1990).
- [18] K. -H. Hong, J. Kim, S. -H. Lee *et al.*, Nano Lett. **8**, 5 (2008).
- [19] L. Wang, A. Rastelli, S. Kiravittaya *et al.*, Adv. Mater. **21**, 2601 (2009).
- [20] K. S. Novoselov, A. K. Geim, S. V. Morozov *et al.*, Science **306**, 666 (2004).
- [21] A. A. Balandin, S. Ghosh, W. Bao *et al.*, Nano Lett. **8**, 902 (2008).
- [22] R. R. Nair, P. Blake, A. N. Grigorenko *et al.*, Science **320**, 1308 (2008).
- [23] C. Lee, X. Wei, W. Kysar *et al.*, Science **321**, 385 (2008).
- [24] M. D. Stoller, S. Park, Y. Zhu *et al.*, Nano Lett. **8**, 3498 (2008).
- [25] Y. Zhang, Y. W. Tan, H. L Stormer *et al.*, Nature **438**, 201 (2005).
- [26] H. Shi, H. Pan, Y. -W. Zhang *et al.*, Phys. Rev. B **87**, 155304 (2013).
- [27] W. S. Yun, S.W. Han, S.C. Hong *et al.*, Phys. Rev. B **85**, 033305 (2012).
- [28] A. P. Alivisatos, Science **271**, 933 (1996).
- [29] L. E. Brus, J. Phys. Chem. Solids **59**, 459 (1998).
- [30] U. Woggon, *Optical Properties of Semiconductor Quantum Dots*, Springer-Verlag, Berlin, (1997).
- [31] C. B. Murray, D. J. Norris and M. G. Bawendi, J. Am. Chem. Soc. **115**, 8706 (1993).
- [32] X. F. Duan and C. M. Lieber, Adv. Mater. **12**, 298 (2000).
- [33] G. Bester, J. Shumway and Alex Zunger, Phys. Rev. Lett. **93**, 4 (2004).

- [34] D. A. Williams and J. R. A. Cleaver, *App. Phys. Lett.* **86**, 012103 (2005)
- [35] L. Esakia and R. Tsu, *IBM J. Res. Dev.* **14**, 61 (1970).
- [36] R. C. Jin, Y. W. Cao, C. A. Mirkin *et al.*, *Science* **294**, 1901 (2001).
- [37] C. S. Ah, Y. J. Yun, H. J. Park *et al.*, *Chem. Mater.* **17**, 5558 (2005).
- [38] M. B. Sigman, A. Ghezelbash, T. Hanrath *et al.*, *J. Am. Chem. Soc.* **125**, 16050 (2003).
- [39] J. Joo, J. S. Son, S. G. Kwon *et al.*, *J. Am. Chem. Soc.* **128**, 5632 (2006).
- [40] Y. Chang and H. C. Zeng, *Cryst. Growth Des.* **4**, 397 (2004).
- [41] L. L. Chang and K. H. Ploog, *In Proceedings of the 1983 Summer School*, Erice, Italy (1983); L. L. Chang, K. Ploog, Eds.; Martinus Nijhoff: Leiden, The Netherlands (1985).
- [42] R. L. Moon and Y.-M. Houn, *In Chemical vapor deposition - Principles and applications*, Academic Press, London, (1993).
- [43] G. B. Stringfellow, *Organometallic vapor phase epitaxy: theory and practice*, Academic Press, Boston, (1989).
- [44] G. B. Stringfellow and H. T. Hall, *J. Crystal Growth* **43** 47 (1978).
- [45] Z. Y. Tang, Z. L. Zhang, Y. Wang *et al.*, *Science* **314**, 274 (2006).
- [46] M. Konagai, M. Sugimoto and K. J. Takahashi, *Cryst. Growth* **45**, 277 (1978).
- [47] J. Yoon, S. Jo, I. S. Chun *et al.*, *Nature* **465**, 329 (2010).
- [48] S. Ithurria and B. Dubertret, *J. Am. Chem. Soc.* **130**, 16504 (2008).
- [49] Al. L. Efros and A. L. Efros, *Sov. Phys. Semicond.* **16**, 772 (1982).
- [50] L. E. Brus, *J. Chem. Phys.* **80**, 4403 (1984).
- [51] G. T. Einevoll, *Phys. Rev. B* **45**, 3410 (1992).
- [52] S. V. Nair, L. M. Ramaniah and K. C. Rustagi, *Phys. Rev. B* **45**, 5969 (1992).

- [53] F. Buda, J. Kohanoff, and M. Parrinello, *Phys. Rev. Lett.* **69**, 1272 (1992).
- [54] G. Bastard. *Wave Mechanics Applied to Semiconductor Heterostructures*. Halstead, New York, (1988).
- [55] M. V. RamaKrishna and R. A. Friesner, *Phys. Rev. Lett.* **67**, 629 (1991).
- [56] H. Fu and A. Zunger, *Phys. Rev. B* **55**, 1642 (1997).
- [57] P. E. Lippens and M. Lannoo, *Phys. Rev. B* **39**, 10935 (1989).
- [58] G. Allan, Y. M. Niquet, and C. Delerue, *Appl. Phys. Lett.* **77**, 639 (2000).

# Chapter 2

## Theoretical Background

### 2.1 Introduction to the Many Particle Hamiltonian

The origin of the wide range of properties of solids arises from the mutual interaction of electrons and nuclei of the constituent atoms. An exact theory for such system is inherently quantum mechanical and is based on solving the many-body time independent Schrödinger equation of the form,  $H\Psi(\mathbf{R}_I; \mathbf{r}_i) = E\Psi(\mathbf{R}_I; \mathbf{r}_i)$

where  $H$  is the Hamiltonian of the system and  $E$  is the energy of the system;  $\Psi(\mathbf{R}_I; \mathbf{r}_i)$  is the many-body wave function that describes the state of the system;  $\mathbf{R}_I$  are the positions of the nuclei and  $\mathbf{r}_i$  are the variables that describe the electrons. The Hamiltonian of the many-body system is,

$$H = - \sum_i \frac{\hbar^2}{2m_e} \nabla_{\mathbf{r}_i}^2 - \sum_I \frac{\hbar^2}{2M_I} \nabla_{\mathbf{R}_I}^2 - \sum_{i,I} \frac{Z_I e^2}{|\mathbf{R}_I - \mathbf{r}_i|} + \frac{1}{2} \sum_{ij(i \neq j)} \frac{e^2}{|\mathbf{r}_i - \mathbf{r}_j|} + \frac{1}{2} \sum_{IJ(I \neq J)} \frac{Z_I Z_J e^2}{|\mathbf{R}_I - \mathbf{R}_J|} \quad (2.1)$$

In the above equation,  $\hbar$  is the Planck's constant divided by  $2\pi$ ;  $M_I$  is the mass and  $Z_I$  is the charge of nucleus  $I$ ;  $m_e$  is the mass and  $e$  is the charge of electron. The terms appearing in the above equation represent the kinetic energy of the electrons; the kinetic energy of the nuclei; the nucleus-electron attractive potential energy; the electron-electron and nucleus-nucleus

repulsive potential energies respectively. In pseudopotential method, the nucleus-electron interaction term is taken care of by convenient pseudopotentials replacing the true potential of the nuclei. The electron-electron interaction part of the Hamiltonian makes the many-body problem so hard that, in most of the cases it is impossible to get the exact solution. Almost all electronic structure calculation methods need some approximations which can simplify the electron-electron interaction.

## 2.2 Born-Oppenheimer (B-O) Approximation

The first and simplest approximation [1] of the Hamiltonian is to drop the kinetic energy term of the nuclei. As the mass of the nucleus is several times larger compared to the electrons, so the time scale of the motion of electrons is much larger than the nuclei and thus the response time of the electrons to any change in the positions of the nuclei is considered instantaneous. In this approximation, the nuclear positions  $\mathbf{R}_I$  become classical variables and the nuclei can be considered as fixed in a given selected configuration. In light of the Born-Oppenheimer approximation, the last term of the above Hamiltonian equation which is the nucleus-nucleus repulsive energy is simply a constant as far as the electronic degrees of freedom are concerned. So, under B-O approximation, the many-body Hamiltonian for a system of interacting electrons moving in the field of fixed ion cores, takes the form,

$$H = - \sum_i \frac{\hbar^2}{2m_e} \nabla_{\mathbf{r}_i}^2 + \sum_i V_{ion}(\mathbf{r}_i) + \frac{1}{2} \sum_{ij(i \neq j)} \frac{e^2}{|\mathbf{r}_i - \mathbf{r}_j|} \quad (2.2)$$

where

$$V_{ion}(\mathbf{r}_i) = - \sum_I \frac{Z_I e^2}{|\mathbf{R}_I - \mathbf{r}_i|} \quad (2.3)$$

This is the ionic potential that every electron experiences at the position  $\mathbf{r}_i$ . We can assume that a system consisting of electrons moving in the external potential  $V_{ion}(\mathbf{r})$  and this term is

replaced by a pseudopotential that takes into account the effects of core electrons. Later, we have discussed about the pseudopotentials in detail in Section. 2.11.1.

## 2.3 Single Particle Approximation

Even with the above simplifications, solving the Hamiltonian for  $\Psi(\mathbf{R}_I; \mathbf{r}_i)$  is a very difficult task. There are two properties of electrons which is responsible for the difficulty-one is the “exchange” property which is the manifestation of the *Pauli exclusion principle* and the other one is the “correlation” property of electron. So, we need further improvement to develop an effective single-particle picture, in which the system of interacting electrons can be mapped into a system of non-interacting quantum mechanical particles that approximates the behaviour of original system. Two distinct approaches have been put forward in this direction: one of them is the wave function approach and the other one is the density functional theory.

Wave function approach can correctly incorporate the *Pauli exclusion principle* for identical fermions. Here the total N-electron ground-state wave function is represented by the best antisymmetrized product of N one-electron spin-orbitals. This is called the Hartree-Fock approximation.

## 2.4 The Hartree Approximation

Hartree [2] proposed a simple way to solve the many-electron Hamiltonian equation. He suggested to rewrite equation (2.1) as a one-particle equation for an electron moving in an average potential from all the electrons. The wave function then becomes

$$\Psi^H(\{\mathbf{r}_i\}) = \phi_1(\mathbf{r}_1)\phi_2(\mathbf{r}_2)\dots\dots\phi_N(\mathbf{r}_N) \quad (2.4)$$

The  $\phi_i(\mathbf{r}_i)$  are N independent electron wave functions. These single particle states are normalized to unity. This is known as the Hartree approximation ( $\Psi^H$  stands for Hartree wave

function). A basic result in quantum mechanics states that if  $E_0$  is the ground state energy solution of the Schrödinger equation, for any wave function  $\varphi$ :

$$\frac{\langle \varphi | H | \varphi \rangle}{\langle \varphi | \varphi \rangle} \geq E_0 \quad (2.5)$$

This is called the variational principle. Using this variational argument in this context we obtain the following single particle equations within the Hartree approximation,

$$\left[ -\frac{\hbar^2}{2m_e} \nabla_r^2 + V_{ion}(\mathbf{r}) + e^2 \sum_{j \neq i} \langle \phi_j | \frac{1}{|\mathbf{r} - \mathbf{r}'|} | \phi_j \rangle \right] \phi_i(\mathbf{r}) = \epsilon_i \phi_i(\mathbf{r}) \quad (2.6)$$

In the Hartree approximation, each electron denoted by index  $i$  is treated independently moving in an effective potential determined by an integration over the wave functions of the other electrons. Thus, this approximation is a mean-field approximation replacing the complicated many-body problem by  $N$  simpler problems in a mean-field potential.

## 2.5 The Hartree-Fock Approximation

In the Hartree approximation, for the many-body wave function in terms of non-interacting single electron state, the antisymmetric nature of the electronic wave function was not considered. Electrons being fermions, the exact many-particle wave function needs to be antisymmetric under an exchange of electrons:

$$\Psi(\mathbf{r}_1, \mathbf{r}_2, \dots, \mathbf{r}_j, \dots, \mathbf{r}_k, \dots, \mathbf{r}_N) = -\Psi(\mathbf{r}_1, \mathbf{r}_2, \dots, \mathbf{r}_k, \dots, \mathbf{r}_j, \dots, \mathbf{r}_N) \quad (2.7)$$

Fock [3] has replaced the Hartree wave function by a Slater determinant to conserve the antisymmetric nature of electrons. This is known as Hartree-Fock approximation and the form of Slater determinant [4] is,

$$\Psi^{HF}(\{\mathbf{r}_i\}) = \frac{1}{\sqrt{N!}} \begin{vmatrix} \phi_1(\mathbf{r}_1) & \phi_1(\mathbf{r}_2) & \dots & \phi_1(\mathbf{r}_N) \\ \phi_2(\mathbf{r}_1) & \phi_2(\mathbf{r}_2) & \dots & \phi_2(\mathbf{r}_N) \\ \vdots & \vdots & \ddots & \vdots \\ \phi_N(\mathbf{r}_1) & \phi_N(\mathbf{r}_2) & \dots & \phi_N(\mathbf{r}_N) \end{vmatrix} \quad (2.8)$$

The total energy with the HartreeFock wave function is,

$$\begin{aligned} E^{HF} &= \langle \Psi^{HF} | H | \Psi^{HF} \rangle \\ &= \sum_i \langle \phi_i | -\frac{\hbar^2}{2m_e} \nabla_r^2 + V_{ion}(\mathbf{r}) | \phi_i \rangle \\ &\quad + \frac{e^2}{2} \sum_{ij(j \neq i)} \langle \phi_i \phi_j | \frac{1}{|\mathbf{r} - \mathbf{r}'|} | \phi_i \phi_j \rangle \\ &\quad - \frac{e^2}{2} \sum_{ij(j \neq i)} \langle \phi_i \phi_j | \frac{1}{|\mathbf{r} - \mathbf{r}'|} | \phi_j \phi_i \rangle \end{aligned} \quad (2.9)$$

Using the variational principle with this Hartree-Fock form of wave function, we obtain the single-particle Hartree-Fock equations,

$$\left[ -\frac{\hbar^2}{2m_e} \nabla_r^2 + V_{ion}(\mathbf{r}) + V_i^H(\mathbf{r}) \right] \phi_i(\mathbf{r}) + e^2 \sum_{j \neq i} \langle \phi_j | \frac{1}{|\mathbf{r} - \mathbf{r}'|} | \phi_i \rangle \phi_j(\mathbf{r}) = \epsilon_i \phi_i(\mathbf{r}) \quad (2.10)$$

The term  $V_i^H(\mathbf{r})$  is called the Hartree potential which takes the form,

$$V_i^H(\mathbf{r}) = e^2 \sum_{j \neq i} \langle \phi_j | \frac{1}{|\mathbf{r} - \mathbf{r}'|} | \phi_j \rangle \quad (2.11)$$

The above Hartree-Fock equation differ from the Hartree equation by one extra term, the last term which is called the “exchange” term. This “exchange” term is the manifestation of the effects of exchange between electrons.

## 2.6 The Correlation Energy

The Hartree-Fock approach which assumes the electrons independently moving in an effective potential is an approximation to the true many-body problem. The difference between the exact total energy and the total energy ( $E_{corr.} = E_{exact} - E^{HF}$ ) given by the Hartree-Fock method is generally called the correlation energy. Many methods exist to introduce this correlation energy very accurately.

## 2.7 The Density Functional Theory

Hohenberg and Kohn in 1964 developed an alternative approach for describing the ground state properties of many-body system more efficiently which is called the density functional theory (DFT). The fundamental concept of DFT is to deal with a formulation of the many-body Schrödinger equation (2.1) that involves the more manageable total density of electrons  $n(\mathbf{r})$  instead of using the many-body wave function  $\Psi(\mathbf{R}_I; \mathbf{r}_i)$ .

There is a huge simplification in DFT, as one can develop the appropriate single-particle equations in an exact manner and then introduce approximations as needed. Whereas in the previous cases one started with a drastic approximation for the behavior of the system (in case of the Hartree and HartreeFock wave functions represent). One can say, all ground state properties of the many electron system are functional of its ground state electron distribution. When the ground state electron distribution of the many electron system is determined, its external potential is also uniquely determined.

In DFT the electron density is the central quantity. In a system of  $N$  electrons the electron density is defined from the wave functions as follows,

$$n(\mathbf{r}) = \sum_{i=1}^N \int \dots \int d\mathbf{r}_1 \dots d\mathbf{r}_N \Psi^*(\mathbf{r}_1, \dots, \mathbf{r}_N) \delta(\mathbf{r}_i - \mathbf{r}) \Psi(\mathbf{r}_1, \dots, \mathbf{r}_N) \quad (2.12)$$

## 2.8 The Hohenberg-Kohn Theorems

Modern theory of DFT is based on the two Hohenberg-Kohn (HK) theorems [5]: the first theorem states that the many-body wave function can be replaced by the electron ground state density without any loss of information and the second theorem is more or less the equivalent of the variational principle in standard quantum mechanics.

The Hohenberg-Kohn theorems are:

**Theorem 1:** *For any system of interacting particles in an external potential  $V_{ext}(\mathbf{r})$ , the potential  $V_{ext}(\mathbf{r})$  is determined uniquely, except for a constant, by the ground state density  $n(\mathbf{r})$ .*

This implies a one-to-one correspondence between the external potential  $V_{ext}(\mathbf{r})$  of the system and the density  $n(\mathbf{r})$ . So, all the properties can thus be extracted from the exact ground state electron density.

Now, we will show that the density  $n(\mathbf{r})$  is uniquely defined given an external potential  $V_{ext}(\mathbf{r})$  for the electrons. Suppose there are two different external potentials  $V_{ext}(\mathbf{r})$  and  $V'_{ext}(\mathbf{r})$  which differ by more than a constant and lead to the same ground state density  $n_0(\mathbf{r})$ . We will prove that this is impossible. These two external potentials would correspond to two different Hamiltonians,  $H$  and  $H'$ . These two Hamiltonians have the same ground state density  $n_0(\mathbf{r})$  but have different ground state wave functions,  $\Psi$  and  $\Psi'$  and the total energies  $E_0$  and  $E'_0$  respectively. So, the Hamiltonian equations are:  $H\Psi = E_0\Psi$  and  $H'\Psi' = E'_0\Psi'$ .

From variational theorem, the energies can be expressed as,

$$E_0 = \langle \Psi | H | \Psi \rangle \quad (2.13)$$

and

$$E'_0 = \langle \Psi' | H' | \Psi' \rangle \quad (2.14)$$

Since,  $\Psi'$  is not the ground state of  $H$ ,

$$\begin{aligned}
E_0 &< \langle \Psi' | H | \Psi' \rangle \\
&< \langle \Psi' | H' | \Psi' \rangle + \langle \Psi' | H - H' | \Psi' \rangle \\
&< E'_0 + \int n_0(\mathbf{r}) [V_{ext}(\mathbf{r}) - V'_{ext}(\mathbf{r})] d\mathbf{r}
\end{aligned} \tag{2.15}$$

Similarly,

$$\begin{aligned}
E'_0 &< \langle \Psi | H' | \Psi \rangle \\
&< \langle \Psi | H | \Psi \rangle + \langle \Psi | H' - H | \Psi \rangle \\
&< E_0 + \int n_0(\mathbf{r}) [V'_{ext}(\mathbf{r}) - V_{ext}(\mathbf{r})] d\mathbf{r}
\end{aligned} \tag{2.16}$$

Adding the equations (2.15) and (2.16) lead to the inconsistency,

$$E_0 + E'_0 < E'_0 + E_0 \tag{2.17}$$

Therefore, we are able to show that no two different external potentials  $V_{ext}(\mathbf{r})$  can lead to the same ground state density  $n_0(\mathbf{r})$ , i.e., the ground state density determines the external potential  $V_{ext}(\mathbf{r})$ , except for a constant. This proves that there is a one-to-one correspondence between an external potential  $V_{ext}(\mathbf{r})$  and the density  $n_0(\mathbf{r})$ .

**Theorem 2:** *A universal functional for the energy  $E[n]$  in terms of the density  $n(\mathbf{r})$  can be defined, valid for any external potential  $V_{ext}(\mathbf{r})$ . The exact ground state energy of the system is the global minimum of this energy functional and the density that minimizes the functional is the exact ground state density  $n_0(\mathbf{r})$ .*

This simplifies the complex problem of finding all ground state physical properties of a system by estimating the minimum of the energy with respect to the electron density instead of wave function. So, if the electron density  $n(\mathbf{r})$  is known, each of the properties of the system can be viewed as a functional of  $n(\mathbf{r})$ , including the total energy functional given by,

$$\begin{aligned}
E[n(\mathbf{r})] &= \langle \Psi[n] | H | \Psi[n] \rangle \\
&= T[n] + E_{int}[n] + \int V_{ext}(\mathbf{r})n(\mathbf{r})d\mathbf{r} \\
&= F[n] + \int V_{ext}(\mathbf{r})n(\mathbf{r})d\mathbf{r}
\end{aligned} \tag{2.18}$$

Where  $F[n]$ , which is the sum of the kinetic energy  $T[n]$  and internal energy  $E_{int}[n]$ , are called Hohenberg- Kohn functional of the interacting electron system. This  $F[n]$  are same for all electron systems having unique density  $n(\mathbf{r})$ .

According to variational principle, for any wave function  $\Psi'$  , the energy functional  $E[\Psi']$  has its global minimum value only when  $\Psi'$  is the ground state wave function  $\Psi^0$ (corresponding to the ground state electron density  $n_0(\mathbf{r})$ ), with the constraint that the total number of the particles is conserved. Now, according to HK **theorem I**,  $\Psi'$  must correspond to a ground state with particle density  $n'(\mathbf{r})$  and external potential  $V'_{ext}(\mathbf{r})$ , then the total energy functional  $E[(n'(\mathbf{r}))]$  will be,

$$\begin{aligned}
E[n'(\mathbf{r})] &= \langle \Psi' | H | \Psi' \rangle \\
&= F[n'(\mathbf{r})] + \int V'_{ext}(\mathbf{r})n'(\mathbf{r})d\mathbf{r} \\
&> \langle \Psi^0 | H | \Psi^0 \rangle \\
&> F[n(\mathbf{r})] + \int V_{ext}(\mathbf{r})n(\mathbf{r})d\mathbf{r} \\
&> E[n(\mathbf{r})]
\end{aligned} \tag{2.19}$$

Thus the energy functional  $E[(n(\mathbf{r}))]$ , evaluated for the exact ground state density  $n_0(\mathbf{r})$  is certainly lower than the value of this functional for any other density  $E[(n(\mathbf{r}))]$ . Therefore by minimizing the total energy functional of the system with respect to variations in the density  $n(\mathbf{r})$ , one would find the exact ground state density and energy.

## 2.9 Kohn-Sham Formulation of Density Functional Theory

It is the Kohn-Sham (KS) [6] approach that puts Hohenberg-Kohn theorems into practical use and makes DFT calculations possible with even a personal computer. They proposed a method for computing the most important part of the kinetic energy functional to good accuracy. The idea is to replace the original many-body system by an auxiliary independent-particle system and assume that the two systems have exactly the same ground state density. In this approach, it maps the original interacting system with real potential onto a fictitious non-interacting system where the electrons move within an effective Kohn-Sham single-particle potential  $V_{KS}(\mathbf{r})$ . For the auxiliary independent-particle system, the auxiliary Hamiltonian is:

$$H_{KS} = -\frac{\hbar^2}{2m_e}\nabla^2 + V_{KS}(\mathbf{r}) \quad (2.20)$$

For a system with  $N$  independent electrons, the ground state is obtained by solving the  $N$  one-electron Schrödinger equations,

$$\left[-\frac{\hbar^2}{2m_e}\nabla^2 + V_{KS}(\mathbf{r})\right]\phi_i(\mathbf{r}) = \epsilon_i\phi_i(\mathbf{r}) \quad (2.21)$$

where there is one electron in each of the  $N$  orbitals  $\phi_i(\mathbf{r})$  with the lowest eigen values  $\epsilon_i$ . The single particle equations (2.21) are referred to as Kohn-Sham equations and the single particle orbitals  $\phi_i(\mathbf{r})$  which are the solutions of the above equations are called Kohn-Sham orbitals. The density of the auxiliary system is constructed from,

$$n(\mathbf{r}) = \sum_{i=1}^N |\phi_i(\mathbf{r})|^2 \quad (2.22)$$

which is subject to the conservation condition:

$$\int n(\mathbf{r})d\mathbf{r} = N \quad (2.23)$$

The non-interacting independent-particle kinetic energy  $T_S[n(\mathbf{r})]$  is given by,

$$\begin{aligned} T_S[n(\mathbf{r})] &= -\frac{\hbar^2}{2m_e} \sum_{i=1}^N \int \phi_i^*(\mathbf{r}) \nabla^2 \phi_i(\mathbf{r}) d(\mathbf{r}) \\ &= \sum_{i=1}^N \langle \phi_i(\mathbf{r}) | -\frac{\hbar^2}{2m_e} \nabla^2 | \phi_i(\mathbf{r}) \rangle \end{aligned} \quad (2.24)$$

Then the universal functional  $F[n(\mathbf{r})]$  can be rewritten as,

$$F[n(\mathbf{r})] = T_s[n(\mathbf{r})] + E_H[n(\mathbf{r})] \quad (2.25)$$

where  $E_H[n(\mathbf{r})]$  is the electron-electron Coulomb interaction energy (called Hartree energy),

$$\begin{aligned} E_H[n(\mathbf{r})] &= \frac{e^2}{2} \int \int \frac{n(\mathbf{r})n'(\mathbf{r}')}{|\mathbf{r} - \mathbf{r}'|} d\mathbf{r}d\mathbf{r}' \\ &= \frac{e^2}{2} \sum_{i,j(i \neq j)} \langle \phi_i(\mathbf{r})\phi_j(\mathbf{r}) | \frac{1}{|\mathbf{r} - \mathbf{r}'|} | \phi_i(\mathbf{r})\phi_j(\mathbf{r}) \rangle \end{aligned} \quad (2.26)$$

Now the Hohenberg-Kohn functional  $E[n(\mathbf{r})]$  is written as,

$$E[n(\mathbf{r})] = T_s[n(\mathbf{r})] + E_H[n(\mathbf{r})] + \int V_{ext}(\mathbf{r})n(\mathbf{r})d\mathbf{r} + E_{XC}[n(\mathbf{r})] \quad (2.27)$$

Here,  $E_{XC}[n(\mathbf{r})]$  is the exchange-correlation functional [7] [8], energy, which contains the difference between the exact and non-interacting kinetic energies.

Since the ground state energy of a many-electron system can be obtained by minimizing the energy functional  $E[n(\mathbf{r})] = F[n(\mathbf{r})] + \int n(\mathbf{r})V_{ext}(\mathbf{r})d\mathbf{r}$ , subject to the constraint that the number of electrons  $N$  is conserved,

$$\delta\{F[n(\mathbf{r})] + \int n(\mathbf{r})V_{ext}(\mathbf{r})d\mathbf{r} - \mu(\int n(\mathbf{r})d(\mathbf{r}) - N)\} = 0 \quad (2.28)$$

The results which we get from the above equation is,

$$\begin{aligned} \mu &= \frac{\delta F[n(\mathbf{r})]}{\delta n(\mathbf{r})} + V_{ext}(\mathbf{r}) \\ &= \frac{\delta T_S[n(\mathbf{r})]}{\delta n(\mathbf{r})} + V_{KS}(\mathbf{r}) \end{aligned} \quad (2.29)$$

where  $\mu$  is the chemical potential.

Now, Kohn Sham single particle potential  $V_{KS}(\mathbf{r})$  is given by,

$$\begin{aligned} V_{KS}(\mathbf{r}) &= V_{ext}(\mathbf{r}) + V_H(\mathbf{r}, n(\mathbf{r})) + V_{XC}(\mathbf{r}, n(\mathbf{r})) \\ &= V_{ext}(\mathbf{r}) + \frac{\delta E_H[n(\mathbf{r})]}{\delta n(\mathbf{r})} + \frac{\delta E_{XC}[n(\mathbf{r})]}{\delta n(\mathbf{r})} \end{aligned} \quad (2.30)$$

From the equations (2.28) and (2.30), the Hartree potential  $V_H(\mathbf{r})$  can be expressed as,

$$\begin{aligned} V_H(\mathbf{r}) &= \frac{\delta E_H[n(\mathbf{r})]}{\delta n(\mathbf{r})} \\ &= \int \frac{n(\mathbf{r}')}{|\mathbf{r} - \mathbf{r}'|} d\mathbf{r}' \end{aligned} \quad (2.31)$$

and similarly, the exchange-correlation (XC) potential  $V_{XC}(\mathbf{r})$  can also be expressed as,

$$V_{XC}(\mathbf{r}) = \frac{\delta E_{XC}[n(\mathbf{r})]}{\delta n(\mathbf{r})} \quad (2.32)$$

Using the well-known KS equations the KS potential can be expressed as,

$$V_{KS}(\mathbf{r}) = V_{ext}(\mathbf{r}) + \int \frac{n(\mathbf{r}')}{|\mathbf{r} - \mathbf{r}'|} d\mathbf{r}' + \frac{\delta E_{XC}[n(\mathbf{r})]}{\delta n(\mathbf{r})} \quad (2.33)$$

Since the KS potential is a function of the density, which is obtained from equation (2.22) and hence depends on all the single-particle states, we need to solve these equations by iteration until we reach self-consistency.

The KS equations, must be solved self-consistently because,  $V_{KS}$  potential is a function of the density, which is obtained from equation (2.22) as well as all the single-particle KS orbitals. Solving the KS orbitals is not a significant problem. A more critical issue is the exact form of  $E_{XC}[n(\mathbf{r})]$  which is unknown. It is very important to have an accurate (XC) energy functional  $E_{XC}[n(\mathbf{r})]$  in order to give a satisfactory description of a realistic condensed-matter system. The most widely used approximations for the XC potential are the local density approximation (LDA), the generalized-gradient approximation (GGA) and hybrid functionals.

## 2.10 The Exchange-Correlation Approximations

### 2.10.1 The Local Density Approximation (LDA)

The simplest physical way to approximate the exchange-correlation energy is the Local Density Approximation (LDA). Although the exact XC energy functional  $E_{XC}[n(\mathbf{r})]$  is very complicated, simplest but successful approximations to it have been made by Kohn and Sham [6], which not only to predict various properties of many systems reasonably well but also greatly reduce computational costs. It leads to the wide use of DFT for electronic structure calculations. In this approximation two assumptions are made: i) the local exchange-correlation energy per particle only depends on the local density (hence the name of the approximation) and ii) is equal to the exchange-correlation energy per particle of a homogeneous electron gas (HEG), that has the same density, in a neutralizing positive background (jellium background). The total exchange-correlation functional  $E_{XC}[n(\mathbf{r})]$  can be written as,

$$E_{XC}^{LDA}[n(\mathbf{r})] = \int n(\mathbf{r})\epsilon_{XC}[n(\mathbf{r})]d\mathbf{r} \quad (2.34)$$

where  $\epsilon_{XC}[n(\mathbf{r})]$  is the exchange-correlation energy per particle of a uniform electron gas of density  $n(\mathbf{r})$ . So, the XC potential [9] may be written as,

$$\begin{aligned} V_{XC}^{LDA}(\mathbf{r}) &= \frac{\delta E_{XC}^{LDA}[n(\mathbf{r})]}{\delta n(\mathbf{r})} \\ &= \epsilon_{XC}[n(\mathbf{r})] + n(\mathbf{r}) \frac{d\epsilon_{XC}[n(\mathbf{r})]}{dn(\mathbf{r})} \end{aligned} \quad (2.35)$$

For unpolarized HEG system, the quantity  $\epsilon_{XC}[n(\mathbf{r})]$  can be further split into exchange and correlation contributions,

$$\epsilon_{XC}[n(\mathbf{r})] = \epsilon_X[n(\mathbf{r})] + \epsilon_C[n(\mathbf{r})] \quad (2.36)$$

The exchange energy,  $\epsilon_X[n(\mathbf{r})]$ , represents the exchange energy of an electron in a homogeneous electron gas. It is derived analytically by Dirac [10] and is given by,

$$\epsilon_X[n(\mathbf{r})] = -\frac{3}{4}e^2\left(\frac{3n(\mathbf{r})}{\pi}\right)^{1/3} \quad (2.37)$$

Analytic expressions for the correlation energy,  $\epsilon_C[n(\mathbf{r})]$  of the HEG is unknown except in the high and low density limits corresponding to infinitely weak and infinitely strong correlations. The expression of the correlation energy density of the HEG at high density limit has the form,

$$\epsilon_X^h[n(\mathbf{r})] = A_1 + A_2\mathbf{r}_s + [A_3 + A_4\mathbf{r}_s] \ln \mathbf{r}_s \quad (2.38)$$

and the low density limit takes the form,

$$\epsilon_X^l[n(\mathbf{r})] = \frac{1}{2}\left[\frac{a_1}{\mathbf{r}_s} + \frac{a_2}{\mathbf{r}_s^{3/2}} + \dots\right] \quad (2.39)$$

where the Wigner-Seitz radius  $\mathbf{r}_s$  is related to the density as,

$$\frac{4}{3}\pi\mathbf{r}_s^3 = \frac{1}{n} \quad (2.40)$$

Accurate values of the correlation energy density at intermediate density can be obtained from quantum Monte Carlo (QMC) calculations [11]. Most local density approximations to the correlation energy density interpolate these accurate values from QMC calculations while reproducing the exactly known limiting behavior. Depending on the analytic forms used for  $\epsilon_C[n(\mathbf{r})]$ , different local density approximations were proposed including Vosko-Wilk-Nusair [12] (VWM), Perdew-Zunger [13] (PZ81), Cole-Perdew [14] (CP) and Perdew-Wang [15] (PW92).

In general, LDA almost always gives a correct picture of binding trends across the periodic table. The structures, bond lengths, vibrational energies, phonon spectra and other properties are predicted correctly, or with a systematic deviation. Binding energies of solids and molecules are usually overestimated, which leads to an underestimation of the bond lengths as well as the band gaps.

### 2.10.2 The Generalized Gradient Approximation (GGA)

The exchange-correlation energy of inhomogeneous charge density can be significantly different from the HEG result. But, LDA neglects the inhomogeneities of the real charge density. So, one can try to improve the LDA expression for the exchange-correlation energy, equation (2.34), by introducing density gradient corrections and higher spatial derivatives of the electron density and this gives better results than LDA in many cases. In a generalized gradient approximation, the functional depends on the density and its gradient,

$$E_{XC}^{GGA}[n(\mathbf{r})] = \int n(\mathbf{r})\epsilon_{XC}[n(\mathbf{r}), |\nabla n(\mathbf{r})|]d\mathbf{r} \quad (2.41)$$

Three most widely used GGAs are the forms proposed by Becke [16] (B88), Perdew *et al.* [17], and Perdew, Burke and Enzerhof [18] (PBE). In comparison to LDA, GGA tend to improve total energies, atomization energies, energy barriers and structural energy differences [18], while

retaining all the correct features of LDA. GGA expand and soften bonds, an effect that sometimes corrects and sometimes overcorrects the LDA prediction. Especially in systems where the charge density is rapidly varying, GGA works better than LDA.

### 2.10.3 The Hybrid Functional

The LDA or GGA approximation can predict the structural properties such as lattice constants and bulk moduli accurately, but these approximations give lower accurate results for the electronic properties such as band gaps. Further improvements in the description of band gaps is achieved by introducing the so-called hybrid functionals [19] which are obtained by admixing a fixed amount of the Hartree-Fock (HF) exchange to an explicit density functional. which takes the effect of Screened Coulomb potential for the exchange interaction. The exchange potential employed in HSE06 is divided into short- and long-range parts, and HF exchange is mixed with Perdew-Burke-Ernzerhof (PBE) exchange in the short-range part. The form of HSE exchange-correlation functional may be expressed as,

$$E_{XC}^{HSE} = aE_X^{HF,SR} + (1 - a)E_X^{PBE,SR} + E_X^{PBE,LR} + E_C^{PBE}[n] \quad (2.42)$$

where  $E_X^{HF,SR}$  and  $E_X^{PBE,SR}$  are the short range and  $E_X^{PBE,LR}$  is the long range exchange interactions. This method fulfills the need for a universally applicable method that is computationally feasible for a wide range of systems and nowadays becomes a popular choice for calculating the structural properties and the band gaps.

## 2.11 Methods for Electronic Structure Calculations

There are a number of methods to solve the single-particle Kohn-Sham equation (2.21) and to obtain the eigen values (band structure) and eigen functions. Among these methods, some are based on k-space approach others are real space approach. In this section we will briefly discuss the some of the most popular methods that are used to calculate the electronic band structure.

### 2.11.1 Plane Wave Pseudopotential Method

Till now, we have shown how to determine the single-particle wave functions by solving the many-body Schrödinger equation for electrons in a solid using proper approximations. When actually solving the single-particle equations in a solid, we need to specify the ionic potential. For an atom in the solid, we only deal with the valence electrons as the core electrons are mostly unaffected. These valence electrons actively participate in determining the most of the chemical and physical properties of molecules and solids. It is well known that the contribution of the valence states to the total electron density is negligible within the core region and dominant beyond it. To separate the valence and core electron states, a highly effective approach has been developed which is the well known pseudopotential method. This method was developed by Phillips and Kleinman [8] which allows us to take the core electrons out of the picture and to create a smoother potential for the valence electrons.

In order to develop the pseudopotential for a specific atom, let us separate explicitly the single-particle states into valence and core sets, denoted as  $|\psi^v\rangle$  and  $|\psi^c\rangle$  respectively. These states satisfy the single particle Schrödinger equations with an approximate potential  $V^{SP}$  which includes the external potential due to the nucleus as well as all the other terms arising from the electron-electron interactions.

Now, a new set of single-particle valence states  $|\phi^v\rangle$  can be defined as,

$$|\psi^v\rangle = |\phi^v\rangle + \sum_c \alpha_c |\psi^c(\mathbf{r})\rangle \quad (2.43)$$

where  $\alpha_c$  can be determined from the condition that  $|\psi^v\rangle$  and  $|\psi^c\rangle$  are orthogonal to each other i.e  $\langle \psi^c | \psi^v \rangle = \alpha_c \delta_{cv}$ , which gives  $\alpha_c = -\langle \psi^v | \phi^c \rangle$ .

Operating the single-particle Hamiltonian  $H^{SP}$  on the new wave functions, we get,

$$H^{SP}[|\phi^v\rangle + \sum_c \alpha_c |\psi^c(\mathbf{r})\rangle] = \varepsilon^v [|\phi^v\rangle + \sum_c \alpha_c |\psi^c(\mathbf{r})\rangle] \quad (2.44)$$

For single particle states of the valence and core electrons, we can write,

$$H^{SP}|\psi^c\rangle = \varepsilon^c|\psi^c\rangle \quad (2.45)$$

$$H^{SP}|\psi^v\rangle = \varepsilon^v|\psi^v\rangle \quad (2.46)$$

From the equations (2.43) and (2.44), we obtain,

$$[H^{SP} + \sum_c (\varepsilon^v - \varepsilon^c)|\psi^c\rangle\langle\psi^c|]|\phi^v\rangle = \varepsilon^v|\phi^v\rangle \quad (2.47)$$

Therefore, the new states  $|\phi^v\rangle$  obey a single-particle equation with a modified potential, but have the same eigen values  $\varepsilon^v$  as the original valence states  $|\psi^v\rangle$ . The modified potential for these states is called the “pseudopotential” shown in Fig. 2.1, which can be expressed as,

$$V^{PS} = V^{SP} + \sum_c (\varepsilon^v - \varepsilon^c)|\psi^c\rangle\langle\psi^c| \quad (2.48)$$

and the corresponding, new states  $|\phi^v\rangle$ 's are called “pseudo-wave functions”. These new valence states project out of the valence wave functions any overlap they have with the core wave functions, thereby having zero overlap with the core states. One can say, through the pseudopotential formulation, we have created a new set of valence states, which experience a weaker potential near the atomic nucleus, but the proper ionic potential away from the core region. Since it is this region in which the valence electrons interact to form bonds that hold the solid together, the pseudo-wave functions preserve all the physical and chemical properties of solids.

Based on the concept of pseudo-potential techniques several methods have been developed to obtain the electronic structure of molecule and solids more accurately. One of the main aims to produce the pseudo-potential is to construct the pseudo-wave functions smoother as well as accurate to make the calculations easier and to get the correct electronic structure of the solids. There are many pseudopotential techniques, one of them is norm-conserving pseudopotential.

The norm-conserving pseudo wave functions are normalized and are solutions of the model pseudo-potential which preserve all the characteristics of valence electrons in an all electron calculations. The valence pseudo-wave functions satisfy the orthonormal conditions as,

$$\langle \psi_i^{\sigma,PS} | \psi_j^{\sigma',PS} \rangle = \delta_{ij} \delta_{\sigma\sigma'} \quad (2.49)$$

Therefore the single particle Schrödinger equations would have the form,

$$H^{\sigma,SP} | \psi_i^{\sigma,SP} \rangle = \varepsilon_i | \psi_i^{\sigma,SP} \rangle \quad (2.50)$$

where,  $H^{\sigma,SP}$  is the Kohn-Sham Hamiltonian with pseudo-potential approximation. There are certain conditions, imposed during the formation of norm-conserving pseudo-potentials as suggested by Harman, Schluter and Chiang (HSC) [20]: one electron Schrödinger equations with pseudo-wave functions are only valid beyond a chosen core radius ( $R_c$ ), The integrated charge inside  $R_c$  for each wave function satisfies the norm-conservation and the logarithmic derivatives of all electron pseudo-wave functions are satisfied at ( $R_c$ ). The pseudo-wave functions constructed with these conditions can well describe the strongly localized systems (3d rare-earth elements) but are no more good to describe the light elements (e.g. first row elements of periodic table). A different approach known as ultrasoft-pseudopotential, first developed by Vanderbilt [21] where the norm-conserving constraint is relaxed and the pseudo-wave functions become smooth with an auxiliary function around each ion core that includes the rapidly varying part of the density. In this method a new form of nonlocal-potential is taken that involves a smooth function  $\phi = r\psi$  which is not norm-conserving. This potentials need very large cutoff energies for localized electrons. The advantage of relaxing the normconserving condition is that each smooth pseudo-wave function may be formed independently with a chosen cutoff radius which is much larger than that of norm-conserving pseudo-potentials.

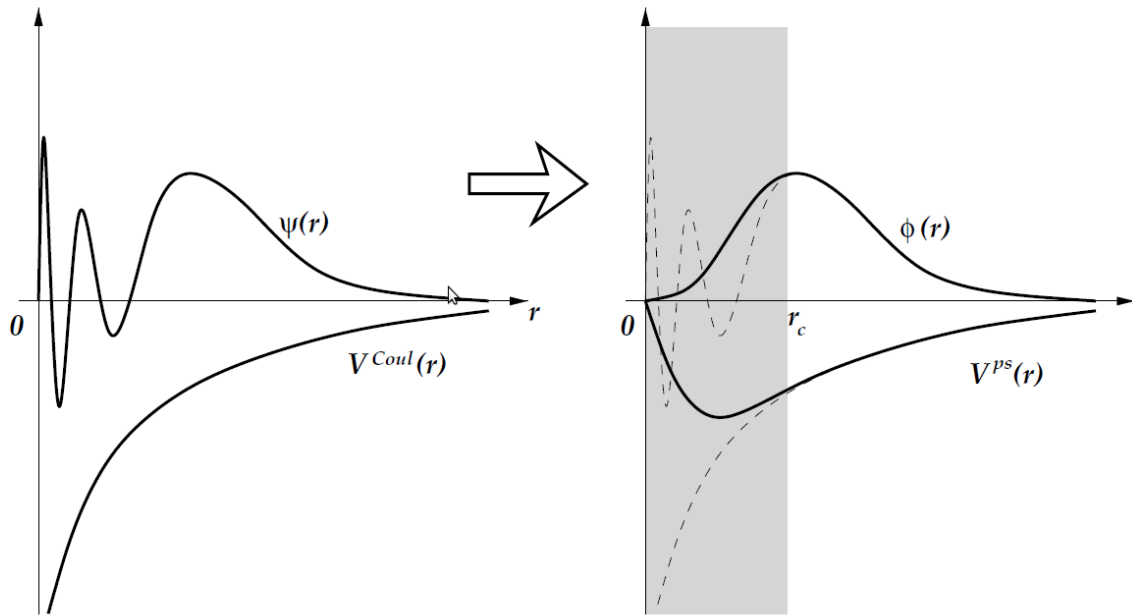


Figure 2.1: Schematic representation of the construction of the pseudo-wave function  $\phi(\mathbf{r})$  and pseudopotential  $V^{PS}(\mathbf{r})$ , beginning with the real valence wave function  $\psi(\mathbf{r})$  and Coulomb potential  $V^{Coul}(\mathbf{r})$ ; ( $R_c$ ) is the cutoff radius beyond which the wave function and potential are not affected (taken from Atomic and Electronic Structure of Solids, E Kaxiras, Cambridge University Press) [8].

## 2.11.2 Projector Augmented Waves (PAWs) Method

Another kind of pseudo-potential technique is the projector augmented wave (PAW) method introduced by Blöchl [22] where the projectors and auxiliary localized functions are introduced in the wave functions. This approach retains the all-electron character, but it includes a decomposition of the all-electron (AE) wave function in terms of a smooth pseudo-wave (PS) function, and a rapidly varying contribution localized within the core region. So here the total wave function is constructed by a combination of the valence wave functions  $\tilde{\psi}_i^v(\mathbf{r})$  and a linear transformation function that relates the set of all-electron valence function  $\psi_j^v(\mathbf{r})$  to  $\tilde{\psi}_i^v(\mathbf{r})$ , that is

$$|\psi_j^v\rangle = |\tilde{\psi}_j^v\rangle + \sum_i (|\phi_i\rangle - |\tilde{\phi}_i\rangle) \langle \tilde{p}_i | \tilde{\Psi}_n \rangle \quad (2.51)$$

The index  $i$  is a shorthand for the atomic site  $R$ , the angular momentum numbers  $L = (l, m)$  and an additional index  $k$  referring to the reference energy  $\varepsilon_{kl}$ . The all electron partial waves  $\phi_i$  are the solutions of the radial Schrödinger equation for the isolated atom, and the PS partial waves  $\tilde{\phi}_i$  are equivalent to the AE partial waves outside a core radius  $R_c$  and match with value and derivative at  $R_c$ . The projector function  $\tilde{p}_i$  for each PS partial wave localized within the core radius, obeys the relation  $\langle \tilde{p}_i | \tilde{\phi}_i \rangle = \delta_{ij}$ . From equation (2.51), it is possible to show that in the PAW method, the AE charge density is given by,

$$n(\mathbf{r}) = \tilde{n}(\mathbf{r}) + n^1(\mathbf{r}) - \tilde{n}^1(\mathbf{r}) \quad (2.52)$$

where,  $n(\mathbf{r})$  is the soft pseudo-charge density calculated directly from the pseudo wave functions on a plane wave grid:

$$\tilde{n}(\mathbf{r}) = \sum_i f_i |\tilde{\psi}_i(\mathbf{r})|^2 \quad (2.53)$$

and the on-site charge densities  $n^1(\mathbf{r})$  and  $\tilde{n}^1(\mathbf{r})$  are treated on a radial support grids localized around each atom. They are defined as,

$$n^1(\mathbf{r}) = \sum_{n,(ij)} f_n \langle \tilde{\Psi}_n | \tilde{p}_i \rangle \langle \phi_i(\mathbf{r}) | \phi_j(\mathbf{r}) \rangle \langle \tilde{p}_j | \tilde{\Psi}_n \rangle \quad (2.54)$$

and

$$\tilde{n}^1(\mathbf{r}) = \sum_{n,(ij)} f_n \langle \tilde{\Psi}_n | \tilde{p}_i \rangle \langle \tilde{\phi}_i(\mathbf{r}) | \tilde{\phi}_j(\mathbf{r}) \rangle \langle \tilde{p}_j | \tilde{\Psi}_n \rangle \quad (2.55)$$

It is to be noted that the charge density  $\tilde{n}^1(\mathbf{r})$  is exactly the same as  $\tilde{n}(\mathbf{r})$  within the augmentation spheres around each atom. In PAW approach, an additional density, called compensation charge density is added to both auxiliary densities  $\tilde{n}(\mathbf{r})$  and  $\tilde{n}^1(\mathbf{r})$  so that the multi-pole moments of the terms  $\tilde{n}(\mathbf{r}) - \tilde{n}^1(\mathbf{r})$  in equation (2.52) vanish.

### 2.11.3 The Tight-Binding Approximation

The tight binding approximation (TBA) is the simplest method for calculating band structures and ground state energy, both conceptually and computationally which was first introduced by Blöch [23]. The basic assumption in TBA is to expand the wave function in terms of atomic orbitals of isolated atoms at each atomic site, or in terms of other local orbitals (e.g.: Wannier functions). This method is also referred to as linear combination of atomic orbital (LCAO) approach and applies to non-crystalline materials and crystalline materials.

Let us first start with a set of atomic wave functions,  $\phi_l(\mathbf{r} - \mathbf{t}_i)$  where  $t_i$  is the position of atom with  $i$  in the periodic unit cell, and  $\phi_l(\mathbf{r})$  is one of the atomic states associated with this atom. The index  $l$  represent the values for the angular momentum character  $s, p, d, \dots$  etc.

A basis state  $\Phi_{\mathbf{k},l,i}(\mathbf{r})$  with wave vector  $\mathbf{k}$  (restricted to the first Brillouin zone) can be constructed from the atomic orbitals  $\phi_l(\mathbf{r} - \mathbf{t}_i)$ , according to Blöch theorem,

$$\Phi_{\mathbf{k},l,i}(\mathbf{r}) = \frac{1}{\sqrt{N}} \sum_{\mathbf{R}'} e^{i\mathbf{k}\cdot\mathbf{R}'} \phi_l(\mathbf{r} - \mathbf{t}_i - \mathbf{R}') \quad (2.56)$$

where  $N$  is the total number of unit cells in the crystal and  $\mathbf{R}'$  is the lattice vector of the periodic lattice. It is easy to show that  $\Phi_{\mathbf{k},l,i}(\mathbf{r})$  satisfies the Bloch theorem.

$$\begin{aligned} \Phi_{\mathbf{k},l,i}(\mathbf{r} + \mathbf{R}) &= \frac{1}{\sqrt{N}} \sum_{\mathbf{R}'} e^{i\mathbf{k}\cdot(\mathbf{R}'-\mathbf{R})} e^{i\mathbf{k}\cdot\mathbf{R}} \phi_l((\mathbf{r} + \mathbf{R}) - \mathbf{t}_i - \mathbf{R}') \\ &= e^{i\mathbf{k}\cdot\mathbf{R}} \frac{1}{\sqrt{N}} \sum_{\mathbf{R}'} e^{i\mathbf{k}\cdot(\mathbf{R}'-\mathbf{R})} \phi_l((\mathbf{r} + \mathbf{R}) - \mathbf{t}_i - \mathbf{R}') \\ &= e^{i\mathbf{k}\cdot\mathbf{R}} \frac{1}{\sqrt{N}} \sum_{\mathbf{R}''} e^{i\mathbf{k}\cdot\mathbf{R}''} \phi_l((\mathbf{r} - \mathbf{t}_i - \mathbf{R}'')) \\ &= e^{i\mathbf{k}\cdot\mathbf{R}} \Phi_{\mathbf{k},l,i}(\mathbf{r}) \end{aligned} \quad (2.57)$$

Now, we can expand the single-particle eigen states in this basis as,

$$\psi_{\mathbf{k}}^n(\mathbf{r}) = \sum_{i,j} c_{\mathbf{k},l,i}^n \Phi_{\mathbf{k},l,i}(\mathbf{r}) \quad (2.58)$$

The coefficients  $c_{\mathbf{k},l,i}^n$  can be determined assuming that  $\psi_{\mathbf{k}}^n(\mathbf{r})$  are solutions of single particle Schrödinger equations,

$$\begin{aligned} H^{SP} \psi_{\mathbf{k}}^n(\mathbf{r}) &= \varepsilon_{\mathbf{k}}^n \psi_{\mathbf{k}}^n(\mathbf{r}) \\ \Rightarrow \sum_{l,i} [\langle \Phi_{\mathbf{k},m,j} | H^{SP} | \Phi_{\mathbf{k},l,i} \rangle - \varepsilon_{\mathbf{k}}^n \langle \Phi_{\mathbf{k},m,j} | \Phi_{\mathbf{k},l,i} \rangle] &= 0 \end{aligned} \quad (2.59)$$

Considering the orthogonality conditions,

$$\langle \psi_{\mathbf{k}}^n | \psi_{\mathbf{k}'}^n \rangle = \delta(\mathbf{k} - \mathbf{k}') \quad (2.60)$$

where we are the values of  $\mathbf{k}, \mathbf{k}'$  are restricted to the first Brillouin zone. So, we have to solve the secular equation (2.59) which has size equal to the number of solutions (bands) that we can

expect at each k-point. In order to solve this linear system we need to be able to evaluate the following integrals,

$$\langle \Phi_{\mathbf{k},m,j} | \Phi_{\mathbf{k},l,i} \rangle = \sum_{\mathbf{R}} e^{i\mathbf{k}\cdot\mathbf{R}} \langle \phi_m(\mathbf{r} - \mathbf{t}_j) | \phi_l(\mathbf{r} - \mathbf{t}_i - \mathbf{R}) \rangle \quad (2.61)$$

The last expression in equation (2.61) is called the “overlap matrix elements” between atomic states. Similar to the way we have evaluated the above integral, we obtain,

$$\langle \Phi_{\mathbf{k},m,j} | H^{SP} | \Phi_{\mathbf{k},l,i} \rangle = \sum_{\mathbf{R}} e^{i\mathbf{k}\cdot\mathbf{R}} \langle \phi_m(\mathbf{r} - \mathbf{t}_j) | H^{SP} | \phi_l(\mathbf{r} - \mathbf{t}_i - \mathbf{R}) \rangle \quad (2.62)$$

and the brackets on the right-hand side of equation (2.62) is called the “Hamiltonian matrix elements” between atomic states.

At this point we introduce the most important approximation of TBA: the overlap matrix elements in equation (2.61) is non-zero only for the same orbitals on the same atom i.e. we use the orthogonality condition between different orbitals,

$$\langle \phi_m(\mathbf{r} - \mathbf{t}_j) | \phi_l(\mathbf{r} - \mathbf{t}_i - \mathbf{R}) \rangle = \delta_{lm} \delta_{ij} \delta(\mathbf{R}) \quad (2.63)$$

Similarly, we take the Hamiltonian matrix elements in equation (2.62) to be non-zero only if the orbitals are on the same atom, which are called the “on-site energies”:

$$\langle \phi_m(\mathbf{r} - \mathbf{t}_j) | H^{SP} | \phi_l(\mathbf{r} - \mathbf{t}_i - \mathbf{R}) \rangle = \delta_{lm} \delta_{ij} \delta(\mathbf{R}) \varepsilon_l \quad (2.64)$$

and if the orbitals are from the nearest neighbor atoms, then they ( $V_{lm,ij}$ ) are called “hopping matrix elements”:

$$\langle \phi_m(\mathbf{r} - \mathbf{t}_j) | H^{SP} | \phi_l(\mathbf{r} - \mathbf{t}_i - \mathbf{R}) \rangle = \delta((\mathbf{t}_j - \mathbf{t}_i - \mathbf{R}) - \mathbf{d}_{\mathbf{nn}}) V_{lm,ij} \quad (2.65)$$

where,  $\mathbf{d}_{\mathbf{nn}}$  is the position vector of nearest neighbor atoms from the reference atom.

Even with this approximation, the values of the matrix elements are to be calculated. The parametrization of the Hamiltonian matrix is efficiently started with the work of Harrison [24] and still it is continuing as an active area of research. There is also a two-center approximation introduced by Slater and Koster [25] for calculating these matrix elements.

### 2.11.4 Wannier Functions

The Bloch wave functions can also be expanded using local orbitals instead of atomic orbitals (in tight binding method). Wannier functions, first proposed by G. Wannier [26], is a candidate of such local orbitals, although they are not localized in some cases when the bandwidths are large, but the Wannier functions are not like the atomic wave functions at all. Technically, Wannier functions are Fourier transformations of Bloch wave functions  $\Phi_{\mathbf{k},n}(\mathbf{r})$ . Since  $\Phi_{\mathbf{k},n}(\mathbf{r})$  is periodic in the reciprocal lattice, i.e.,  $\Phi_{\mathbf{k}+\mathbf{G},n}(\mathbf{r}) = \Phi_{\mathbf{k},n}(\mathbf{r})$ , where  $\mathbf{G}$  is a reciprocal lattice vector,  $\Phi_{\mathbf{k},n}(\mathbf{r})$  can be expanded in plane waves as,

$$\Phi_{\mathbf{k},n}(\mathbf{r}) = \sum_{\mathbf{R}} w_n(\mathbf{r} - \mathbf{R}) e^{i\mathbf{k}\cdot\mathbf{R}} \quad (2.66)$$

where, the coefficients  $w_n(\mathbf{r} - \mathbf{R})$  are Wannier functions and can be obtained by inverse transformation,

$$w_n(\mathbf{r} - \mathbf{R}) = \frac{V_{cell}}{(2\pi)^3} \int_{BZ} e^{-i\mathbf{k}\cdot\mathbf{R}} \Phi_{\mathbf{k},n}(\mathbf{r}) d\mathbf{k} \quad (2.67)$$

where  $V_{cell}$  is the volume of the real-space primitive cell of the crystal. The Wannier functions are not unique because any Bloch function  $\Phi_{\mathbf{k},n}(\mathbf{r})$  doesn't undergo a "gauge transformation",

$$\Phi_{\mathbf{k},n}(\mathbf{r}) \rightarrow \tilde{\Phi}_{\mathbf{k},n}(\mathbf{r}) = e^{i\phi_n(\mathbf{k})} \Phi_{\mathbf{k},n}(\mathbf{r}) \quad (2.68)$$

In addition to the freedom in the choice of phase factor  $\phi_n(\mathbf{k})$ , there is also a degree of freedom associated with the choice of a full unitary matrix  $U_{nm}^{\mathbf{k}}$ , which transforms the  $N$  Bloch wave

functions  $\Phi_{\mathbf{k},n}(\mathbf{r})$  between themselves at every wave vector  $k$ , but the electronic energy functional (in an insulator) remains invariant. The most general form of the Wannier functions is given by,

$$w_n(\mathbf{r} - \mathbf{R}) = \frac{V_{cell}}{(2\pi)^3} \int_{BZ} \sum_{m=1}^N U_{nm}^{\mathbf{k}} e^{-i\mathbf{k}\cdot\mathbf{R}} \Phi_{m\mathbf{k}}(\mathbf{r}) d\mathbf{k} \quad (2.69)$$

$U^{\mathbf{k}}$  is a unitary matrix that mixes the Bloch states at each  $\mathbf{k}$  point.  $U^{\mathbf{k}}$  is not uniquely defined and different choices will lead to wave functions with varying spatial localizations. A widely used way of constructing Wannier functions is the maximally localized Wannier functions proposed by Vanderbilt and coworkers [27] [28], in which the quantity

$$\Omega = \sum_{n=1}^N [\langle \mathbf{r}^2 \rangle_n - \langle \mathbf{r} \rangle_n^2] \quad (2.70)$$

is minimized by choosing appropriate  $U^{\mathbf{k}}$ , where  $\langle \dots \rangle$  is the expectation value over the  $n$ -th Wannier function in the unit cell.

The Wannier functions  $w_n(\mathbf{r} - \mathbf{R})$  are completely orthogonal to each other. so, one can write,

$$\int w_m(\mathbf{r} - \mathbf{R}_i) w_n(\mathbf{r} - \mathbf{R}_j) = \delta_{mn} \delta_{ij} \quad (2.71)$$

In the tight binding approach, if Wannier functions are used as the local orbitals, the overlap matrix and hopping matrix elements are greatly simplified. This is a main advantage to use Wannier functions in tight binding method.

In practice, Wannier functions are constructed from the results of DFT calculations and after that those are used as the local orbitals in tight binding method. The hopping parameters and the on-site energies are obtained by fitting the bands from the tight binding method to the band structures of DFT calculations. The hopping parameters are then used to construct model Hamiltonians to study many-body systems.

# Bibliography

- [1] M. Born and J. R. Oppenheimer, *Zur Quantentheorie der Molekeln*, Ann. Physik **84**, 457 (1927).
- [2] D. R. Hartree, *The wave mechanics of an atom with non-coulombic central field: Parts I, II, III*. Proc. Cambridge Phil. Soc. **24**, 89, 111, 426 (1928).
- [3] V. Fock, *Naherungsmethode zur Losung des quanten-mechanischen Mehrkorperprobleme*, Z. Phys. **61**, 126 (1930).
- [4] J. C. Slater, *The Theory of Complex Spectra*, Phys. Rev. **34**,1293 (1929).
- [5] P. Hohenberg and W. Kohn, Phys. Rev. **136**, B684 (1964).
- [6] W. Kohn and L. J. Sham, Phys. Rev. **140**, A1133 (1965).
- [7] A. D. Becke, J. Chem. Phys. **98**, 5648 (1993).
- [8] E. Kaxiras, *Atomic and Electronic Structure of Solids*, Cambridge University Press, UK (2003).
- [9] J. P. Perdew, E. R. McMullen and A. Zunger, Phys. Rev. A **23**, 2785 (1981).
- [10] P. A. M. Dirac, Proc. Cambridge Phil. Roy. Soc. **26**, 376(1930).
- [11] D. M. Ceperly and B.J. Alder, Phys. Rev. Lett. **45**, 566 (1980).
- [12] S. H. Vosko, L. Wilk and M. Nusair, Can. J. Phys. **58**, 1200 (1980).

- [13] J. P. Perdew and A. Zunger, Phys. Rev. B **23**, 5048 (1981).
- [14] L. A. Cole and J. P. Perdew, Phys. Rev. A **25**, 1265 (1982).
- [15] J. P. Perdew and Y. Wang, Phys. Rev. B **45**, 13244 (1992).
- [16] A. D. Becke, Phys. Rev. A **38**, 3098 (1988).
- [17] J. P. Perdew, J. A. Chevary, S. H. Vosko *et al.*, Phys. Rev. B **46**, 6671 (1992).
- [18] J. P. Perdew, K. Burke, and M. Ernzerhof, Phys. Rev. Lett. **77**, 3865 (1996).
- [19] J. Heyd, G. E. Scuseria and M. Ernzerhof, J. Chem. Phys. **118**, 8207 (2003).
- [20] D. R. Hamann, M. Schluter and C. Chiang, Phys. Rev. Lett. **43**, 1494 (1979).
- [21] D. Vanderbilt, Phys. Rev. B **41**, 7892 (1985).
- [22] P. E. Blöchl, Phys. Rev. B **50**, 17953 (1994).
- [23] F. Bloch, Z. Physik **52**, 555 (1928).
- [24] W. A. Harrison, *Electronic Structure and the Properties of Solids* W.H. Freeman, San Francisco, (1980).
- [25] J. C. Slater and G. F. Koster, Phys. Rev. **94**, 1498 (1954).
- [26] G. H. Wannier, Phys. Rev. **52**, 191 (1937).
- [27] N. Marzari and D. Vanderbilt, Phys. Rev. B **56**, 12847 (1997).
- [28] I. Souza, N. Marzari, and D. Vanderbilt, Phys. Rev. B **65**, 035109 (2001).

# Chapter 3

## Effective Mass Driven Structural Transition in a Mn-Doped ZnS Nanoplatelet

### 3.1 Introduction

Among binary semiconductors, formed by elements of the III-V and II-VI groups, one finds that the more ionic members favor the wurtzite structure, while the covalent ones are found to favor the zinc blende form [1], with the other form (zinc blende and wurtzite, respectively) being available as a metastable state with an energy only a few meV per atom higher than the ground state [2]. Since physical and chemical properties of any material depend critically on the specific crystal structure, such a low-lying metastable state holds out the interesting possibility of tilting the energy balance in favor of the metastable phase even under small perturbations, thereby drastically altering material properties. The strong interplay between the structure of binary semiconductors and its consequent properties has been actively investigated for bulk materials over several decades now, using external parameters such as pressure and temperature [3]. At the nano regime, the large surface to volume ratio provides additional

control parameters that have been effectively used in recent times to tune the structure of such binary semiconductor nanocrystals; such crystal structure transformations have been achieved by tuning growth conditions [4], choice of surface ligands [5] [6] or even just the size of the nanoparticles [7]. These results are easily understood in terms of the large contribution of the surface energy to the total energy of a nanoparticle in the small size regime. For example, the binding energy of a ligand attachment on the surface of a nanoparticle can be significantly different depending on its crystal structure [5]; thus, attaching ligands to most of the surface sites can significantly alter the total energy of a nanoparticle depending on its structure. Interestingly, there has been a recent report of a different class of structural transitions, namely; reversible structural transformation of ZnS nanoplatelets that cannot be understood in terms of such relatively simple energy considerations, because, among other reasons, it is reported to be triggered by the smallest level of reversible doping of Mn in the host [8]. We summarize below the essential and striking aspects of the experimental observations reported in Ref. [8].

It is found [8] that different sizes of the undoped ZnS nanoplatelets could be formed under certain synthesis conditions of carrying out the reaction in a solvent at an elevated temperature of 300 °C. These nanoplatelets invariably formed in the wurtzite structure independent of any subsequent temperature cycling of the reaction mixture or of the extracted nanocrystals redispersed in the solvent. Surprisingly, however, in the presence of a low concentration of Mn<sup>2+</sup> ions in the solvent with redispersed ZnS nanoplatelets, it is found that the ZnS nanoplatelets transformed to the zinc blende structure at an elevated temperature of the solvent (< 180 °C) accompanied by the insertion of Mn<sup>2+</sup> ions into the host ZnS matrix, as evidenced from the appearance of the characteristic intense Mn<sup>2+</sup> photo luminescence emission on exciting the ZnS host and from electron paramagnetic resonance (EPR) studies [8]. Curiously, this transformation is found to be reversible with respect to a cycling of the temperature with Mn<sup>2+</sup> ions being ejected from the host ZnS nanoplatelet and the crystal structure of the host reverting back to the wurtzite one on lowering the temperature below 180 °C. It is also reported in Ref. [8] that similar effects are not observed either for spherical ZnS nanoparticles as well as ZnS nanoplatelets with sizes larger than 14 nm in diameter.

It is to be noted that there is no evidence of stacking faults in these nanocrystals in either of the two crystallographic forms, though transformations between wurtzite and zinc blende structures are known [9] to be usually driven by such stacking faults. Though a wurtzite to zinc blende transformation involving carrier doping has been suggested on the basis of theoretical investigations in certain bulk semiconductors [10] [11], such a mechanism cannot be invoked here, since  $\text{Mn}^{2+}$  ions substitute the Zn ions isovalently without involving any carrier doping. In order to understand the microscopic origin of such an unusual phase transformation, we use first principle electronic structure calculations carried out within the framework of density functional theory. In this chapter, the results show that at a fundamental level, quantum confinement effects at the nanoscale are responsible for the observed phenomenon, the two structure types being discriminated by Mn incorporation/ejection essentially due to significantly different hole effective masses in the zinc blende and wurtzite phases. Our results also explain the absence of any such structural transformation above a certain size of the nanocrystal.

## 3.2 Methodology

Nanoplatelets are constructed in the present investigation in accordance with the experimental observations [9] as follows: The growth direction for the wurtzite nanoplatelet has been taken as  $\langle 111 \rangle$  as observed experimentally, while both directions  $\langle 110 \rangle$  and  $\langle 111 \rangle$  are studied for the zinc blende nanoplatelet. Two different nanoplatelets with diameters of 0.75 nm and 1.5 nm have been investigated in the present study; both these platelets have 4 monolayer thickness. The results are compared with corresponding results for the bulk. The bulk lattice constants of  $a = 5.41 \text{ \AA}$  for the zinc blende case [12] as well as  $a = 3.82 \text{ \AA}$  and  $c = 6.24 \text{ \AA}$  for the wurtzite case [12] are used for constructing the supercells corresponding to nanoplatelets of a given size. 12  $\text{\AA}$  of vacuum is used along the x, y and z directions to ensure negligible interactions between the supercell units. We use projected augmented wave potentials [13] within a plane wave implementation of density functional theory in VASP code [14] with the LDA approximation [15] for the exchange-correlation functional. A plane wave cutoff energy for the basis sets of 280 eV has been used for the electronic structure calculations which are performed at  $\Gamma$  point only.

Besides two different sized nanoplatelets for each structure type and two differently oriented platelets for the zinc blende, we had to carry out a large number of calculations for each such constructed nanoplatelet, placing a  $\text{Mn}^{2+}$  ion at each of the nonequivalent  $\text{Zn}^{2+}$  sites to study the impact of Mn incorporation in these nanoplatelets. However, we have not attempted calculations with multiple Zn sites being simultaneously replaced by Mn ions, since experimental findings indicated [8] that even a very dilute presence of Mn is sufficient to cause the structural transformation; moreover, the number of symmetry inequivalent positions for incorporating even two Mn ions in a given nanoplatelet will make the number of calculations hopelessly large. It is to be noted that a complete optimization of all internal coordinates within the supercell for every doped and undoped nanoplatelet is carried out till the force on each atom is less than  $0.005 \text{ eV}/\text{\AA}$ . As usual, the surface Zn and S atoms are passivated with pseudo-hydrogens. Spheres of radii  $1 \text{ \AA}$  are constructed about each atom to calculate the atom and orbital-projected density of states. We first calculated the formation energy of nanoplatelets as well as that for bulk ZnS in the two crystallographic forms. Calculated results are found to be in agreement with experimental observations. For example, the nanoplatelet of  $0.75 \text{ nm}$  diameter is found to be the most stable in the wurtzite form compared to the zinc blende form by about  $100\text{-}200 \text{ meV}$  per atom depending on the specific orientation ( $\langle 110 \rangle$  or  $\langle 111 \rangle$ ) of the zinc blende nanoplatelets. In contrast, the zinc blende structure is found to be slightly (by  $\sim 3 \text{ meV}$  per atom) stabler compared to the wurtzite structure for the bulk ZnS, thus establishing a structural transition as a function of size for ZnS. With the correct structure predicted for the undoped nanoplatelets, we probe the implication of doping Mn in these systems. We note that the formation energy for one Mn incorporation is given by  $E_c(\text{ZnS}: \text{Mn}) - E_c(\text{ZnS}) - \mu_{\text{Zn}} - \mu_{\text{S}}$  where  $\mu$ 's are the chemical potentials for the corresponding atoms and  $E_c(\text{ZnS}: \text{Mn})$  and  $E_c(\text{ZnS})$  are the total energies of the nanoplatelets with and without Mn doping in a given crystal structure, indicated by the subscript  $c$ ; we use  $c = w$  or  $z$  to denote the wurtzite or the zinc blende structure, respectively. Since  $\mu_{\text{Zn}}$  and  $\mu_{\text{S}}$  refer to the atom and therefore, are independent of the structure, it suffices to compare the relative binding energy, defined as  $\Delta E_c = E_c(\text{ZnS}: \text{Mn}) - E_c(\text{ZnS})$ , for different crystal structures and orientations, in order to understand the relative stabilities of different forms of nanoplatelets. In order to obtain important insights in the reactivity in each case,

we also analyze the wave function corresponding to the valence band maximum (VBM) or the highest occupied molecular orbital. In the absence of a common reference frame, the energy position of the VBM for each case has been determined by referencing its energy to the averaged electrostatic potential associated with the central atom calculated assuming a unit charge within a sphere of radius 1 Å.

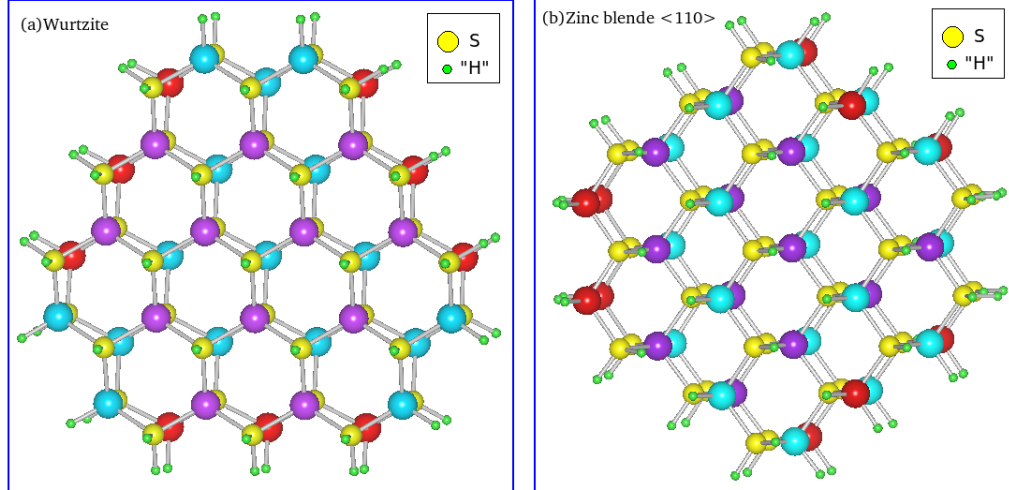


Figure 3.1: (a) Wurtzite  $\langle 0001 \rangle$  and (b) zinc blende  $\langle 110 \rangle$  ZnS nanoplatelets of medium size. Magenta, cyan and red atoms are the Zn atoms which are 0, 1 and 2-fold coordinated with pseudo-hydrogens.

### 3.3 Results and Discussion

At the surface of these nanoplatelets, Zn sites are coordinated to either one or two pseudohydrogens. Evaluating the binding energy of Mn doping on the surface of the ZnS nanocrystals, we find that Mn is much more likely to attach itself at a site that has only one pseudo-hydrogen and three sulphur bonds independent of the structure or the growth direction. In order to understand the mechanism of Mn incorporation in the experimentally observed zinc blende  $\langle 110 \rangle$  oriented nanoplatelets, we have evaluated the relative binding energy of Mn doping at different surface sites. The dopant sites for the 1.5 nm sized nanoplatelet are shown in Fig.

Table 3.1: Relative binding energy of Mn at the most stable sites for different sizes of ZnS nanoplatelets with respect to corresponding wurtzite phase.

Platelet Size	$\Delta E_w$ (eV)	$\Delta E_{z\langle 110 \rangle}$ (eV)	$\Delta E_{z\langle 110 \rangle}$ (eV)
Small	0	-40	-8
Medium	0	-15	+11
Bulk	0	+5	+5

3.1. Our results show that the relative binding energy is the highest for Mn incorporation at a near edge position. This would suggest that the Mn incorporation in ZnS nanoplatelets may begin with the incorporation of Mn at a near edge site, as the preferred site. This finds experimental support in the observation that the Mn doping induced phase transformation begins near the edge of the nanocrystal, as evidenced by transmission electron micrograph of nanoplatelets with arrested, incomplete structural transformation reported in ref. [8]. However, experimental evidence points to eventual incorporation of the Mn ion into a subsurface tetrahedrally coordinated site in the ground state as deduced on the basis of EPR results [8]. In order to understand this result specifically, and the relative binding energy of Mn at various sites of different nanoplatelets in general, we have carried out a large number of calculations with Mn at different inequivalent sites of the different nanoplatelets. We have tabulated the largest binding energy found in each size, namely the small, medium nanoplatelets and the bulk, for different crystal structures, as shown in Table 3.1; in each size we give the results with respect to the wurtzite case. Table 3.1 shows that Mn incorporation lowers the energy the most, for zinc blende nanoplatelets with the  $\langle 110 \rangle$  orientation, representing a stability of 40 meV and 15 meV over the wurtzite phase for the small and the medium sized nanoplatelets, respectively. This reflects accurately the experimentally observed conversion of the undoped wurtzite nanoplatelet to the zinc blende  $\langle 110 \rangle$  oriented nanoplatelets on being doped by Mn; the strongest binding site for Mn in all these cases is invariably found to be a subsurface site, in agreement with the EPR evidence.

Interestingly, the energy stability associated with the formation of the zinc blende structure on Mn doping is obviously size dependent, with the smallest sized nanoplatelet exhibiting the maximum stability of 40 meV over the wurtzite nanoplatelet. With an increase in the size to a 1.5 nm diameter platelet, the energy stability of the zinc blende phase over the wurtzite one decreases rapidly to 15 meV. While it proved impossible to carry out similar calculations for larger sized nano-platelets due to computational limitations, we find that for a bulk ZnS system, Mn incorporation stabilizes the wurtzite structure, reversing the trend observed for the small nanoplatelets of ZnS. This systematic trend with the size is consistent with the experimental observation that the crystallographic phase transformation from the wurtzite to the zinc blende phase does not take place for large sized nanoplatelets. We have further carried out exploratory investigations on spherical nanoparticles of ZnS; our results indicate that Mn-doped ZnS in the zinc blende form is not stabilized over the wurtzite form for spherical nanoparticles, once again consistent with the experimental report [8].

Encouraged by the above mentioned close correspondence between experimental observations and our results in every aspect, we have attempted to obtain a microscopic understanding of this size dependent, doping induced structural transition, driven apparently by certain size dependent, quantum confinement effects. We first analyze the bonding of Mn at the substitutional site by investigating Mn charge density along the Mn-S bond direction for various cases. We focus on changes in the charge density distribution in the zinc blende structure compared to the corresponding wurtzite charge density distribution. Fig. 3.2(a) shows the results for the smallest nanoplatelets considered here. This figure shows that the charge density for the zinc blende case is substantially depleted near the Mn site, being pushed out towards the S site along the bond-length compared to the wurtzite case. This clearly establishes a more covalent Mn-S bond in the zinc blende  $\langle 110 \rangle$  nanoplatelet compared to the same sized wurtzite  $\langle 0001 \rangle$  nanoplatelet. The larger sized nanoplatelets show a similar effect, though less pronounced compared to the case of the smaller sized nanoplatelet. Looking at the bulk case, we find that one has a reversal of the trend with the charge density being more localized on the Mn in the zinc blende case, as shown in Fig. 3.2(b). Thus, the enhanced binding energy

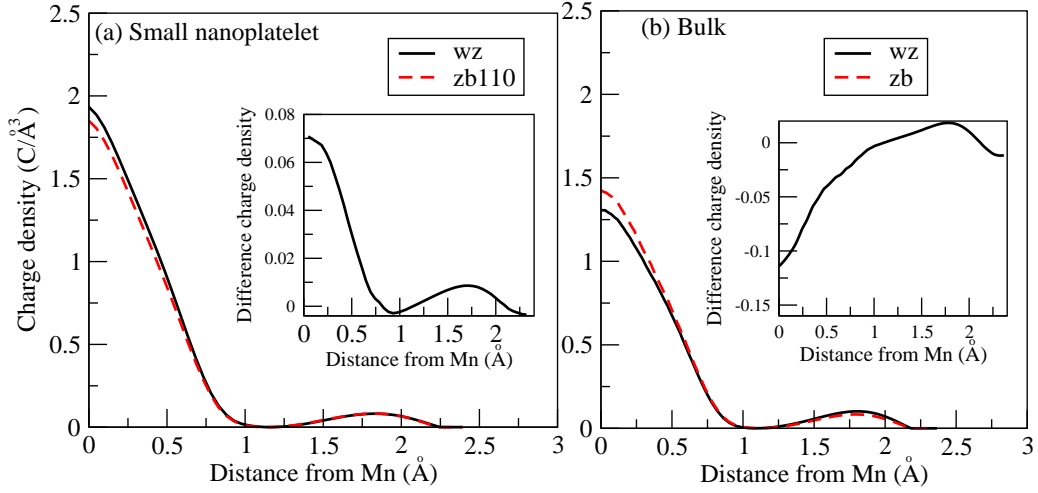


Figure 3.2: Charge density of Mn majority spin antibonding levels with  $t_2$  symmetry for (a) wurtzite (wz) and zinc blende  $\langle 110 \rangle$  (zb110) nanoplatelet and (b) wurtzite (wz) and zinc blende (zb) of bulk ZnS as a function of the distance from Mn along the Mn-S bond-length. In the inset the difference of the wz and zinc blende charge density of the respective graph is shown. It should be noted that since the charge density along a short distance of the bond is given, charge conservation doesn't seem to be apparent from the figure.

of Mn incorporation in the zinc blende  $\langle 110 \rangle$  nanoplatelet (see Table 3.1), responsible for the structural transformation observed experimentally, is driven by a change in the covalency of the Mn-S bond in the two crystallographic forms as a function of the nanoplatelet size. The systematic enhancement of the covalency of the Mn-S bond for the zinc blende structure with the decreasing size is responsible for the doped nanoplatelet favoring the zinc blende structure in the small size regime.

The covalency of any given bond is controlled by two parameters, namely the energy difference and the hopping or the hybridization strength between the two orbitals participating in the bonding. The hybridization strength is a function of the inter-atomic distance or the bond-length, the functional form depending on the nature of the orbitals involved. In this specific case, our calculations show that Mn-S bond-lengths do not change perceptibly between the bulk and various nanoplatelets; consequently, we do not expect any significant change in the Mn  $d$  S  $p$  hybridization strength. Therefore, the reversal of the Mn binding energy trend between the bulk and nanoplatelets shown in Table 3.1 cannot be associated with any change in the hopping strength leading to a change in the covalency. In order to understand the effect of the size on the remaining parameter, which is the energy difference between the Mn  $d$  and S  $p$  states, it is important to note here that Mn  $d$  levels, being essentially localized in nature, will not be affected significantly by the size of the cluster [16] [17] [18] [19]. Therefore, we may consider the energy of Mn  $d$  levels to be practically constant for all cases considered here. In contrast, the S  $p$  levels are expected to be strongly influenced by the quantum confinement effect increasingly for smaller sized clusters [20] [21] [22] [23]. We find a direct evidence of this quantum confinement effect in the energy position of the VBM with dominantly S  $p$  character.

Valence band maxima referenced to the average electrostatic potential at the central Zn site for different cases are given in Table 3.2, exhibiting a pronounced dependence on the size for both crystallographic forms. Each type of system, be it wurtzite, zinc blende  $\langle 110 \rangle$  or zinc blende  $\langle 111 \rangle$ , shows a systematic decrease of the energy of the VBM with a decrease in size. This can be ascribed to quantum confinement effects as has already been observed for both the VBM and the conduction band minimum (CBM) [20] [21] [22] [23] for a wide variety of semiconductor materials. However, it is important to notice that the stabilization of the VBM

Table 3.2: Positions of VBM of different sizes of nanoplatelets of ZnS as well as that bulk ZnS. The relative shifts of the VBM in the case of the wurtzite and zinc blende nanodisks with respect to the bulk values for the same structure have been provided in parentheses.

Platelet Size	$\Delta E_w$ (eV)	$\Delta E_{z\langle 110 \rangle}$ (eV)	$\Delta E_{z\langle 111 \rangle}$ (eV)
Small	38.480(0.908)	38.530(0.530)	38.446(0.929)
Medium	38.905(0.483)	38.967(0.408)	38.872(0.503)
Bulk	39.388(0.000)	39.375(0.000)	39.375(0.000)

compared to the bulk VBM, shown in brackets in Table 3.2, is more rapid, for the wurtzite structure and the zinc blende nanoplatelet with  $\langle 111 \rangle$  orientation compared to the zinc blende  $\langle 110 \rangle$  oriented nanoplatelet. As a consequence, the VBM has the highest energy for the zinc blende  $\langle 110 \rangle$  nanoplatelets (e.g. 38.530 eV for the small size) compared to those with the wurtzite structure (38.480 eV for the small size) and the zinc blende  $\langle 111 \rangle$  one (38.446 eV for the small size) at any given size. Since Mn  $d$  level lies above the VBM, a decreasing size implies that the energy separation between two will increase more rapidly for the wurtzite and the zinc blende  $\langle 111 \rangle$  nanoplatelets making Mn-S bond more ionic, when compared to the relatively more covalently bonded Mn-S in the zinc blende  $\langle 110 \rangle$  nanoplatelet due to the smallest Mn  $d$ -VBM energy separation in the latter. This is exactly what is reflected in the difference charge density plot in Fig. 3.2, underlining the enhanced stability of Mn-doped zinc blende nanoplatelets with  $\langle 110 \rangle$  orientation. Thus, we only need to understand the microscopic origin of the trend of quantum confinement effects on the position of the VBM given in Table 3.2, to obtain a complete understanding of the puzzling phenomenon.

In order to understand the origin of this more pronounced quantum confinement effect of the VBM for the wurtzite and zinc blende  $\langle 111 \rangle$  nanoplatelets compared to the zinc blende  $\langle 110 \rangle$  nanoplatelets, we first note that the shift in energies in such confined systems is inversely related to the relevant effective hole mass. Thus, we have computed the effective hole mass in several directions for the bulk zinc blende and wurtzite unit cells. However, the confinement in

nanoplatelets is primarily determined by the effective hole mass in the growth direction, since we have just four monolayers in thickness defining the smallest dimension in the problem. The effective hole masses along  $\langle 0001 \rangle$  direction in the wurtzite structure and those along the  $\langle 111 \rangle$  and  $\langle 110 \rangle$  direction in the zinc blende structure are  $1.2 m_e$ ,  $1.5 m_e$  and  $3.5 m_e$ , respectively. As the hole effective mass ( $1.2 m_e$ ) for wurtzite along the  $\langle 0001 \rangle$  direction and that ( $1.5 m_e$ ) for the zinc blende along the  $\langle 111 \rangle$  direction are smaller than that ( $3.5 m_e$ ) for zinc blende in the  $\langle 110 \rangle$  direction, the VBMs get pushed down more rapidly for the wurtzite and the zinc blende  $\langle 111 \rangle$  cases compared to that for the zinc blende  $\langle 110 \rangle$  case which is shown schematically in Fig. 3.3, providing the final microscopic explanation of the observed unusual structural transition in ZnS nanoplatelets induced by Mn doping.

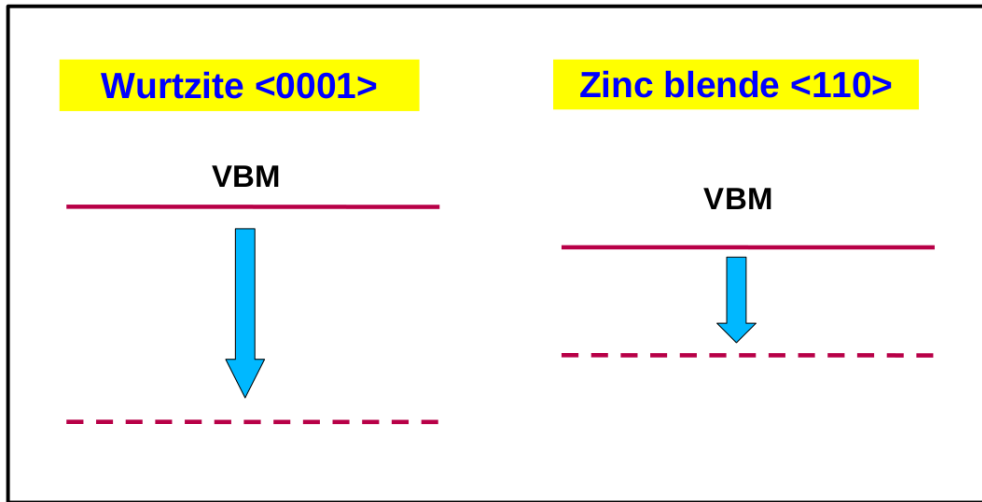


Figure 3.3: Movement of VBMs of wurtzite  $\langle 0001 \rangle$  and zinc blende  $\langle 110 \rangle$  due to quantum confinement effect.

### 3.4 Conclusion

Mn doping in ZnS nanoplatelets has been shown to induce a structural transition from the wurtzite to the zinc blende phase. We trace the origin of this transition to quantum confinement

effects, which shift the VBM of the wurtzite and zinc blende polymorphs of ZnS at different rates as a function of the nanocrystal size, arising from different effective hole masses in the two structures. This modifies the covalency associated with Mn incorporation and is reflected in the size-dependent binding energy difference for the two structures. Thus, it appears that differences in the relevant effective masses in the bulk semiconductor control the Mn-dopant induced crystal structure transformation in ZnS nanoplatelets via quantum confinement effects. This fact, though rarely appreciated in the past, must be operational in a large number of other contexts, besides such structural transformations, since changing covalency of chemical bonds influences a wide range of chemical properties.

# Bibliography

- [1] T. Ito, Jpn. J. Appl. Phys. **37**, L1217 (1998).
- [2] C. -Y. Yeh, Z. W. Lu, S. Froyen *et al.*, Phys. Rev. B **45**, 12130 (1992).
- [3] A. Mujica, A. Rubio, A. Muñoz *et al.*, Rev. Mod. Phys. **75**, 863 (2003).
- [4] M. Kruszynska, H. Borchert, J. Parisi *et al.*, J. Am. Chem. Soc. **132**, 15976 (2010).
- [5] A. Nag, A. Hazarika, K. V. Shanavas *et al.*, J. Phys. Chem. Lett. **2**, 706 (2011).
- [6] J. Huang, M. V. Kovalenko and D. V. Talapin, J. Am. Chem. Soc. **132**, 15866 (2010).
- [7] M. J. Polking, J. J. Urban, D. J. Milliron *et al.*, Nano Lett. **11**, 1147 (2011).
- [8] N. S. Karan, S. Sarkar, D. D. Sarma *et al.*, J. Am. Chem. Soc. **133**, 1666 (2011).
- [9] K. Takahashi and T. Morizumi, Jpn. J. Appl. Phys. **5**, L1217 (1998).
- [10] G. M. Dalpian and S.-H. Wei, Phys. Rev. Lett. **93**, 216401 (2004).
- [11] E. -A. Choi, J. Kang and K. J. Chang, Phys. Rev. B **74**, 245218 (2006).
- [12] G. Bergerhoff and I. D. Brown, *Crystallographic Databases*, F. H. Allen, G. Bergerhoff and R. Sievers, *Eds.; International Union of Crystallography*: Chester, U.K. (1987).
- [13] G. Kresse and D. Joubert, Phys. Rev. B **59**, 1758 (1999).
- [14] G. Kresse and J. Furthmuller, Phys. Rev. B **54**, 11169 (1996).
- [15] J. P. Perdew and A. Zunger, Phys. Rev. B **23**, 5048 (1981).

- [16] R. Cherian and P. Mahadevan, Phys. Rev. B **76**, 075205 (2007).
- [17] M. J. Caldas, A. Fazzio and A. Zunger, Appl. Phys. Lett. **45**, 671 (1984).
- [18] X. Huang, A. Makmal, J. R. Chelikowsky *et al.*, Phys. Rev. Lett. **94**, 236801 (2005).
- [19] N. S. Norberg, G. M. Dalpian, J. R. Chelikowsky *et al.*, Nano Lett. **6**, 2887 (2006).
- [20] S. Sapra and D. D. Sarma, Phys. Rev. B **69**, 125304 (2004).
- [21] S. Sapra, N. Shanthi and D. D. Sarma, Phys. Rev. B **66**, 205202 (2002).
- [22] R. Viswanatha, S. Sapra, T. Saha-Dasgupta *et al.*, Phys. Rev. B **72**, 045333 (2005).
- [23] R. Viswanatha and D. D. Sarma, Chem. Asian J. **4**, 904 (2009).

# Chapter 4

## 3-D to 1-D Quantum Confinement in ZnS Nanoplatelets as a Function of Lateral Dimension

### 4.1 Introduction

Recent advances in growth techniques have led to the growth of two-dimensional platelets of semiconductors by colloidal methods [1]. The platelets grown by this technique achieve almost atomic layer precision in the growth of some materials, something which was earlier possible only in molecular beam epitaxy growth [2]. The other advantage of this technique has been that one could entirely do away with the substrate and generate free-standing films [3] [4]. Colloidal nanoparticles have been intensely studied for their optical properties which can be tuned by size [5] [6] as well as by doping transition metal atoms [7] [8]. The advantage of the nanoplatelets is the wide variety of their lateral dimensions which results in crystalline nanoplatelets even though they are only a few monolayers thick. This results in well-resolved emission with full width at half maximum less than 40 meV even at room temperature [9]. Additionally fluorescence yields are large as 60% [10]. The materials that have been synthesized in the

platelet form include various semiconductors such as CdS, CdSe, CdTe, In<sub>2</sub>Se<sub>3</sub>, SnS to name a few [9] [10] [11] [12]. The microscopic considerations which lead to the formation of layered platelets instead of three-dimensionally confined nanocrystals are still not well understood. Control on the thickness have been achieved from 4 to 11 monolayers [9]. This leads to strongly confined excitons which are able even at room temperature.

These materials offer a playground where quantum confinement physics can be probed. We consider the example of ZnS which has a small Bohr exciton radii and examine the band gap changes within a parametrized tight binding model as the lateral dimensions of the platelets are changed. This has been done for several thicknesses. One finds that for sizes of nanoplatelets with radii atleast 5 Å less than the Bohr exciton radii, the changes in the band gap are small. As a result of the confinement in the vertical direction, there is however a deviation in the band gap from it's bulk value. If we consider each of the thicknesses and subtract out the band gap at the Bohr exciton radius, we find that all the curves almost collapse onto each other for radii in the range 18-25 Å and beyond. This implies that one can talk of separability of the potential in the lateral as well as in the vertical direction only when one has weak confinement in the lateral direction but not otherwise.

## 4.2 Methodology

ZnS nanoplatelets which we have studied in his chapter are grown along  $\langle 0001 \rangle$  direction for wurtzite the structure ( $wz\langle 0001 \rangle$ ) and two growth directions  $\langle 001 \rangle$  and  $\langle 1\bar{1}0 \rangle$  are considered for the zinc blende structure ( $zb\langle 001 \rangle$  and  $zb\langle 1\bar{1}0 \rangle$ ) shown in Figs. 4.1, 4.2 and 4.3. The experimental lattice constants are used for generating the nanoplatelets and are equal to  $a=3.82$  Å and  $c=6.24$  Å [13] for wurtzite and  $a=5.41$  Å [13]for the zinc blende structures. We have started constructing the nanoplatelets from a radius of 3 Å (except for  $zb\langle 1\bar{1}0 \rangle$ ) and go upto the bulk limit of 25 Å as this is the Bohr exciton radius for ZnS.

The atoms on the surfaces of the nanoplatelets have dangling bonds which generate surface states near the band gap region. To get rid of these states, the Zn and S atoms on the surfaces

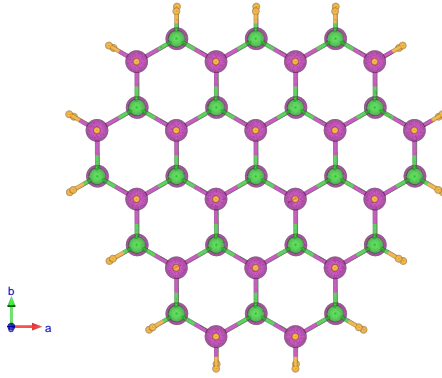


Figure 4.1: Crystal structure of  $wz\langle 0001 \rangle$  ZnS nanoplatelets. Zn, S and pseudo-hydrogens are shown by magenta, green and orange colours respectively.

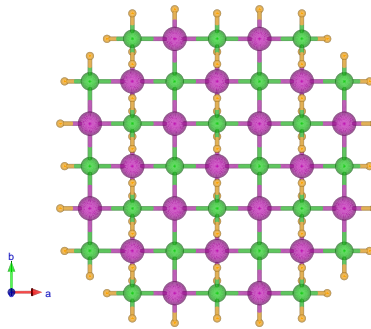


Figure 4.2: Crystal structure of  $zb\langle 001 \rangle$  ZnS nanoplatelets. Zn, S and pseudo-hydrogens are shown by magenta, green and orange colours respectively.

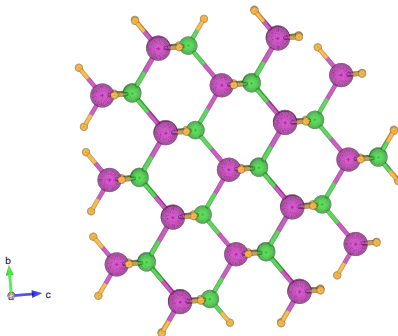


Figure 4.3: Crystal structure of  $zb\langle 1\bar{1}0 \rangle$  ZnS nanoplatelets. Zn, S and pseudo-hydrogens are shown by magenta, green and orange colours respectively.

of the nanoplatelets are passivated by pseudo-hydrogens with fractional charges 1.5e and 0.5e respectively [14]. The number of atoms and the corresponding radius for each of the sizes of nanoplatelets along different growth directions considered in our study are shown in Table 4.1. For the *ab-initio* calculation of the electronic structure of these nanoplatelets 12 Å of vacuum is used along the x, y and z directions to ensure negligible interactions between the supercell units. We use projected augmented wave potentials [15] within a plane wave implementation of density functional theory in VASP code [16] with the LDA approximation [17] for the exchange-correlation functional. We have carried out the same calculation of the nanoplatelets in some cases using hybrid functionals, HSE06 [18] for the exchange as it can capture the experimental band gap more accurately in most of the materials whereas LDA usually underestimates the band gap. A plane wave cutoff energy for the basis sets of 280 eV has been used for the electronic structure calculations which are performed at  $\Gamma$  point only. All the positions of the unit cell are relaxed till the force on each atom is less than 0.005 eV/Å.

In order to investigate the variation of band gap as a function of size, we have calculated the band gaps of the nanoplatelets by tight binding method. The tight binding Hamiltonian is given by,

$$H = \sum_{il} \epsilon_{il} a_{il}^\dagger a_{il} + \sum_{ij} \sum_{lm} (t_{ij}^{lm} a_{il}^\dagger a_{jm} + H.c.) \quad (4.1)$$

where  $a_{il}^\dagger$  and  $a_{il}$  are the creation and annihilation operators respectively for electrons at the atomic site,  $i$  in the  $l$ th orbital. The onsite energy for the orbital  $l$  at the site  $i$  is given by  $\epsilon_{il}$  and the hopping interaction strengths  $t_{ij}^{lm}$  depend on the type of orbitals and geometry of the lattice and are parametrized in terms of the Slater-Koster parametrization [19].

To set up the tight binding model for the nanoplatelets, the input parameters namely the onsite energies and the hopping interaction strengths for Zn and S atoms are derived by fitting the band dispersion obtained from tight binding Hamiltonian in equation 4.1 to the *ab-initio* band dispersions using hybrid functionals for wurtzite and zinc blende structures of bulk ZnS. In order to determine the appropriate basis functions for the tight binding model of bulk wurtzite and

Table 4.1: The radius ( $r$ ) and the corresponding number of atoms ( $N$ ) for all the ZnS nanoplatelets with 4-monolayer in thickness considered in our study.

	wz $\langle 0001 \rangle$	zb $\langle 001 \rangle$	zb $\langle 1\bar{1}0 \rangle$
$r$ (Å)	$N$	$N$	$N$
3	26	-	17
4	50	-	47
5	56	57	55
6	92	69	75
7	104	93	105
8	140	109	127
9	158	145	161
10	194	169	215
11	218	225	223
12	260	261	245
13	296	317	309
14	368	349	357
15	380	401	407
16	470	473	461
17	494	533	505
18	560	581	563
19	608	637	593
20	692	713	705
21	716	777	729
22	800	873	827
23	842	941	883
24	882	1037	949
25	900	1142	1024

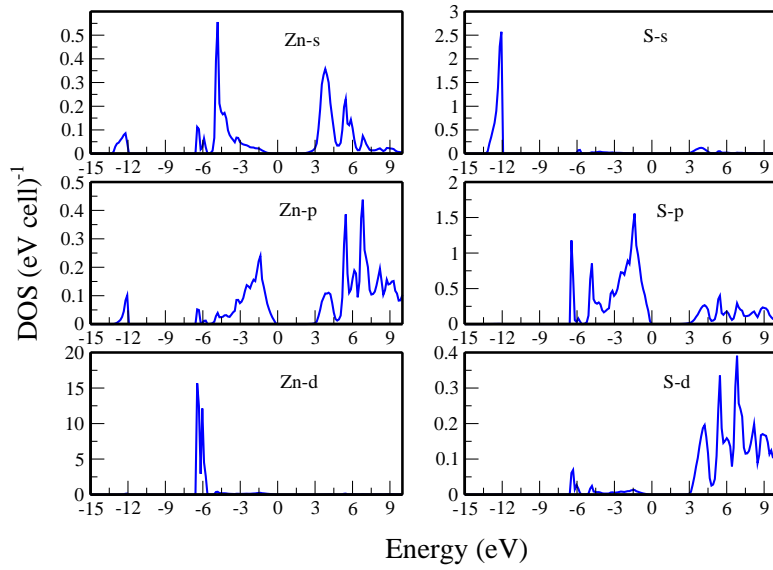


Figure 4.4: The atom and angular momentum projected partial density of states for Zn and S atoms of bulk wurtzite ZnS from *ab-initio* calculations using LDA potentials. Zero of energy corresponds to the Fermi energy.

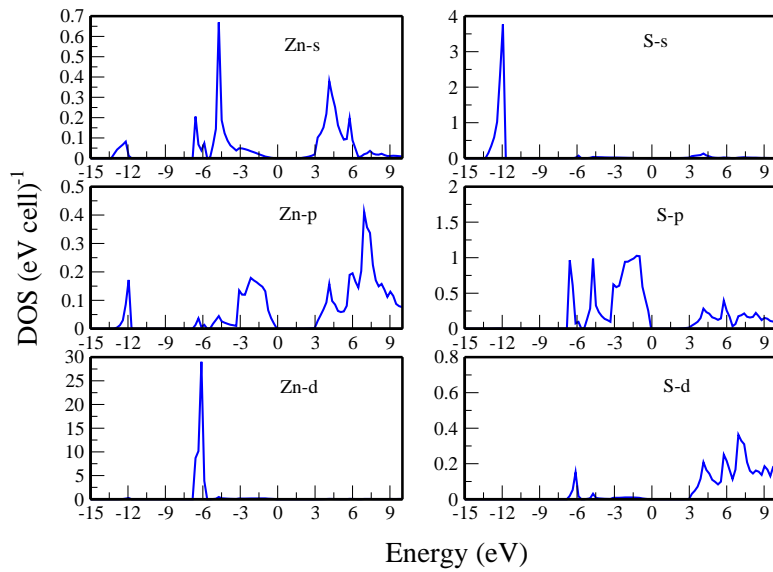


Figure 4.5: The atom and angular momentum projected partial density of states for Zn and S atoms of bulk zinc blende ZnS from *ab-initio* calculations using LDA potentials. Zero of energy corresponds to the Fermi energy.

zinc blende ZnS, the projected density of states (PDOS) are calculated for both the structures which are shown in Fig. 4.4 and 4.5. The zero of the energy in the figures is the Fermi energy. The PDOS show that the dominant contribution is coming from Zn  $s, d$  and S  $p$  states while non-zero contribution is coming from other states. So, we setup the tight binding model with Zn  $s, p, d$  and S  $s, p, d$  states as the basis states. The *ab-initio* calculations for the bulk ZnS are carried out in the frame work of density functional theory in VASP code [16]. Projected augmented wave [15] potentials are used to solve the electronic structure self-consistently using a k-mesh of  $16 \times 16 \times 16$  for both wurtzite and zinc blende structures respectively. Plane wave cut-off energy for the basis sets of 280 eV are used for both wurtzite and zinc blende structures respectively. All the positions of the unit cell are relaxed till the force on each atom is less than  $0.005 \text{ eV}/\text{\AA}$ . For the tight binding calculation of the bulk ZnS for both the structures, we have considered  $s, p, d$  orbitals of Zn and S atoms as the basis states. Now, the tight binding parameters are determined by a least-square error minimization [20] of the bands from the tight binding Hamiltonian given by equation 4.1 to fit the *ab-initio* bands. A Harrison's type scaling [21] of all the hopping integrals of the form  $1/r^{l+l'+1}$  has been assumed for the interactions for deviations upto  $0.1 \text{ \AA}$  about the distance at which the hopping interaction strength is defined while the onsite energies are allowed to vary. Now, the onsite energies of the passivants and the hopping interaction strengths between the passivants and surface atoms (Zn and S) are chosen in such a way that the band gaps obtained from the tight binding calculation of the nanoplatelets reproduce the band gap from the *ab-initio* calculation using hybrid functionals considering one size (radius= $4 \text{ \AA}$ ) for each nanoplatelet of  $wz\langle 0001 \rangle$  and  $zb\langle 001 \rangle$ .

Now, considering the extracted onsite and hopping parameters of the Zn, S and the passivants the band gap of the nanoplatelets are calculated as a function of radius by a tight binding method. The  $s$  and  $p$  orbitals of all the Zn and S atoms in the cluster as well as the  $s$  orbital of the pseudo-hydrogens are considered as basis states. In this model, the contribution to the Hamiltonian are considered till second neighbors for the Zn and S atoms and for pseudo-hydrogens, the contribution is taken till first neighbors only in the cluster.

Table 4.2: Band gaps for different ZnS nanoplatelets with 4-monolayer in thickness considered in our study at different radii as well as the bulk band gaps from *ab-initio* calculations using LDA for the exchange-correlation functional. In brackets the *ab-initio* band gaps are given using hybrid functionals. The energies are in eV.

$r$ (Å)	wz⟨0001⟩	$r$ (Å)	zb⟨001⟩	$r$ (Å)	zb⟨11̄0⟩
4	4.79(6.09)	4	5.35(6.93)	5	4.92(6.58)
5	4.62	5	4.82	6	4.73
Bulk	1.95(3.44)	Bulk	1.86(3.34)		

### 4.3 Results and Discussion

The *ab-initio*(LDA) band gaps of small sized ZnS nanoplatelets along different growth directions considered in our present study are tabulated in Table 4.2. The values for a few cases have been obtained using hybrid functionals and these have been given in parantheses. To compare these band gaps with their bulk values, we have also shown the bulk band gaps of wurtzite and zinc blende ZnS in Table 4.2 obtained within *ab-initio* calculations using LDA potentials for the exchange-correlation functional. From the table it is apparent that the band gaps of the nanoplatelets are much larger than their respective bulk values of 1.95 eV and 1.86 eV for wurtzite and zinc blende (LDA). These results reveal that, as the lateral dimensions (radius) of the nanoplatelets is reduced, quantum confinement along the planes of the nanoplatelets is enhanced which brings about these larger band gaps. Now, one needs to investigate the variation of band gaps of the considered nanoplatelets as a function of their lateral dimensions (radius). As the *ab-initio* calculations for large systems are highly time consuming and expensive, we have examined the variation of band gap with size of the considered nanoplatelets using the tight binding model.

In order to obtain the parameters for the tight binding model of nanoplatelets, we fit the tight binding bands of bulk ZnS for both wurtzite and zinc blende structures to the bands obtained

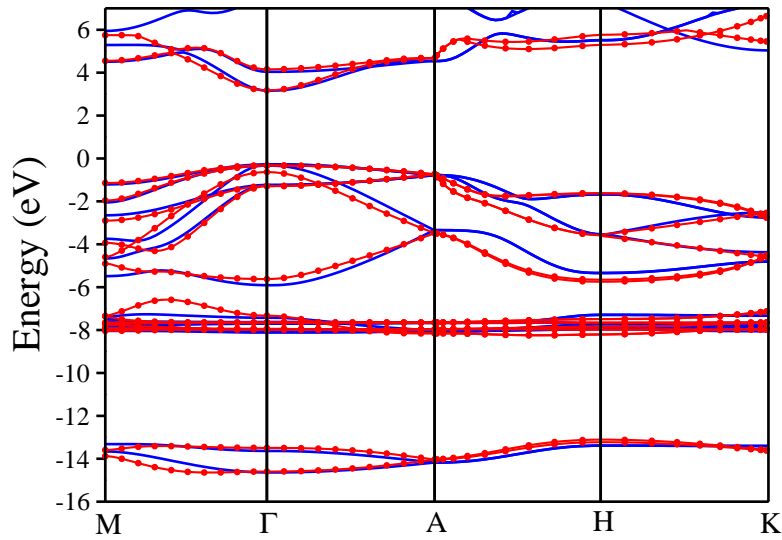


Figure 4.6: Comparison of *ab-initio* band dispersions (blue solid line) for bulk wurtzite ZnS at its experimental lattice constant, using hybrid functionals and the fitted tight binding bands (red line with circles), using a basis consisting of Zn  $s,p,d$  and S  $s,p,d$  states. The zero of energy is the valence band maximum.

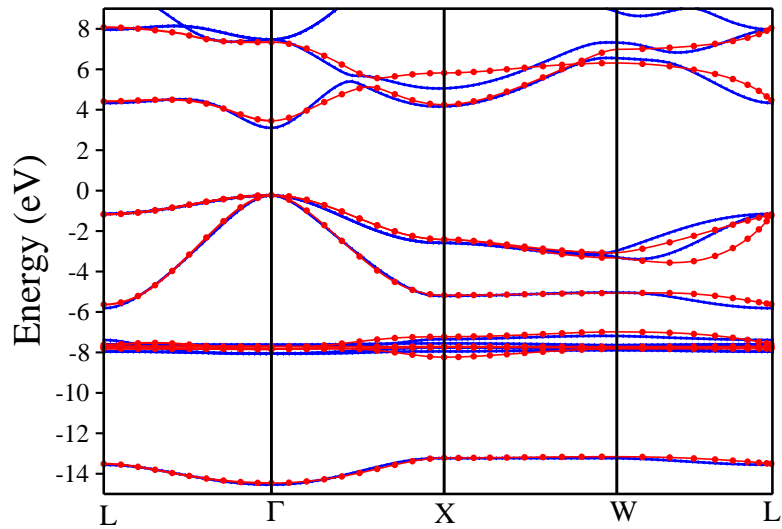


Figure 4.7: Comparison of *ab-initio* band dispersions (blue solid line) for bulk zinc blende ZnS at its experimental lattice constant, using hybrid functionals and the fitted tight binding bands (red line with circles), using a basis consisting of Zn  $s,p,d$  and S  $s,p,d$  states. The zero of energy is the valence band maximum.

from *ab-initio* calculations using hybrid functionals [18] through a least-square error minimization process [20]. The superposition of the *ab-initio* and the tight binding band structures along various symmetry directions are shown in Figs. 4.6 and 4.7 for wurtzite and zinc blende structures of bulk ZnS respectively. These figures show that bulk wurtzite and zinc blende ZnS are direct band gap semiconductors with band gaps of 3.44 eV and 3.34 eV respectively, almost capturing the experimental values of 3.9 eV and 3.8 eV [22]. The onsite energies and the Slater-Koster parameters derived from the tight binding fitting are tabulated in Table 4.3 and 4.4 for wurtzite and zinc blende structures of ZnS. Although the parameters have been extracted by fitting the bulk band dispersions, transferrability is assumed to the nanoregime, proof of this is discussed later in this chapter. The surface of the nanoplatelets are passivated by pseudo-hydrogens. In our tight binding model, we use pseudo-hydrogen atoms with *s* orbitals on them. The interaction between the pseudo-hydrogens and the surface atoms could modify the band gap. Hence their choice becomes important.

In our study the onsite energies of the passivating atoms and the Slater-Koster parameters between the passivants and surface atoms (Zn and S) are chosen in such a way that the band gaps obtained by the tight binding method with these chosen parameters reproduces the band gaps obtained from the *ab-initio* calculations using hybrid functionals for some sizes of the nanoplatelet. In Fig. 4.8 and 4.9, the density of states (DOS) are plotted from *ab-initio* calculation using hybrid functionals as well as from tight binding calculations for ZnS wz<0001> and zb<1 $\bar{1}$ 0> nanoplatelets with thickness 4-monolayer of radius 4 Å respectively. As, calculations using LDA as exchange-correlation functional underestimates the band gap, the *ab-initio* calculations are performed using hybrid functionals [18] and the band gaps are found to be 6.09 eV and 6.58 eV for wz<0001> and zb<1 $\bar{1}$ 0>. Comparing these values of band gaps with their respective values 6.08 eV and 6.56 eV from tight binding calculation, the band gaps from both the calculations are in good agreement with each other. This gives us confidence in the extracted parameters and we use it to calculate the electronic structure of other sizes of the nanoplatelets. The extracted onsite energies and the hopping interaction strengths for the passivants (H1 and H2) are listed in Table 4.5. The parameters obtained from these considered sizes are used for the other sizes of their respective structures.

Table 4.3: Parameters obtained from least-square error fitting of the *ab-initio* using hybrid functional band structure onto a tight binding model using *s, p, d* orbitals of Zn and S for bulk wurtzite of ZnS. The energies are in eV.

	$E_s$	$E_p$	$E_d$
Zn	4.64	12.19	-5.97
S	-9.23	-0.29	13.78
	$E(Zn,Zn)$	$E(Zn,S)$	$E(S,S)$
<i>ss</i> $\sigma$	-0.19	-1.29	-0.09
<i>sp</i> $\sigma$	0.19	2.95	0.38
<i>sd</i> $\sigma$	0.00	-0.67	-0.62
<i>pp</i> $\sigma$	0.55	2.05	0.39
<i>pp</i> $\pi$	-0.01	-0.97	-0.03
<i>pd</i> $\sigma$	0.00	-1.89	0.00
<i>pd</i> $\pi$	0.00	2.52	0.00
<i>dd</i> $\sigma$	0.00	0.00	0.00
<i>dd</i> $\pi$	0.00	0.00	0.00
<i>dd</i> $\delta$	0.00	0.00	0.00
<i>ps</i> $\sigma$	-0.19	-1.01	-0.38
<i>ds</i> $\sigma$	0.00	-1.55	-0.62
<i>dp</i> $\sigma$	0.00	0.96	0.00
<i>dp</i> $\pi$	0.00	-0.19	0.00

Table 4.4: Parameters obtained from least-square error fitting of the *ab-initio* using hybrid functional band structure onto a tight binding model using *s, p, d* orbitals of Zn and S for bulk zinc blende of ZnS. The energies are in eV.

	$E_s$	$E_p$	$E_d$
Zn	1.74	11.07	-6.15
S	-7.83	1.80	12.94
	$E(Zn,Zn)$	$E(Zn,S)$	$E(S,S)$
<i>ss</i> $\sigma$	-0.13	-1.98	-0.02
<i>sp</i> $\sigma$	0.01	2.98	0.19
<i>sd</i> $\sigma$	0.00	-1.01	0.00
<i>pp</i> $\sigma$	0.21	4.07	0.55
<i>pp</i> $\pi$	-0.12	-0.42	-0.05
<i>pd</i> $\sigma$	0.00	-0.68	0.00
<i>pd</i> $\pi$	0.00	2.51	0.00
<i>dd</i> $\sigma$	0.00	0.00	0.00
<i>dd</i> $\pi$	0.00	0.00	0.00
<i>dd</i> $\delta$	0.00	0.00	0.00
<i>ps</i> $\sigma$	-0.01	-2.04	-0.19
<i>ds</i> $\sigma$	0.00	-1.71	0.00
<i>dp</i> $\sigma$	0.00	0.50	0.00
<i>dp</i> $\pi$	0.00	-0.25	0.00

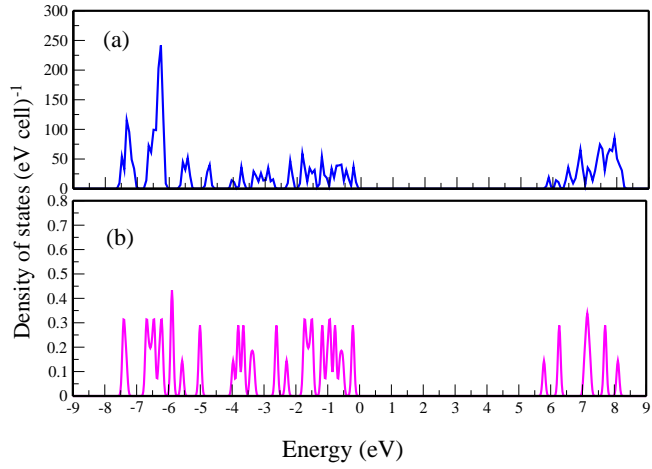


Figure 4.8: The density of states (DOS) of  $wz\langle 0001 \rangle$  with radius  $4 \text{ \AA}$  and thickness 4 monolayer from *ab-initio* calculations using hybrid functionals (a) and from tight binding calculation (b). Zero of energy corresponds to the is the valence band maximum.

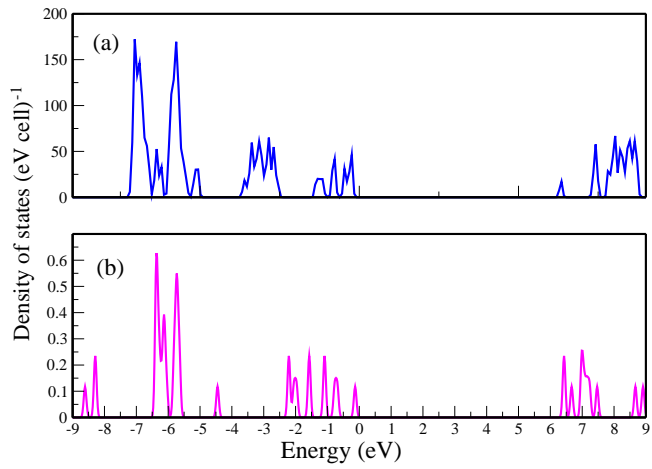


Figure 4.9: The density of states (DOS) of  $zb\langle 1\bar{1}0 \rangle$  with radius  $4 \text{ \AA}$  and thickness 4 monolayer from *ab-initio* calculations using hybrid functionals (a) and from tight binding calculation (b). Zero of energy corresponds to the is the valence band maximum.

Table 4.5: Parameters obtained from the fitting of the *ab-initio* band gap using hybrid functional to a tight binding model using *s, p* orbitals of Zn and S atoms and *s* orbital for pseudo-hydrogens (H1 and H2) for wurtzite and zinc blende nanoplatelets of ZnS. The energies are in eV.

	$E_s(wz)$	$E_s(zb)$		
H1	-5.0	-4.0		
H2	12.0	5.0		
	$E(Zn, H1)_{wz}$	$E(S, H2)_{wz}$	$E(Zn, H1)_{zb}$	$E(S, H2)_{zb}$
<i>ss</i> $\sigma$	-1.80	-2.50	-4.0	-1.00
<i>ps</i> $\sigma$	-2.20	-2.00	-3.0	-2.50

Now, with all the required input parameters (onsite and hopping strengths), the band gaps of the nanoplatelets of  $wz\langle 0001 \rangle$ ,  $zb\langle 001 \rangle$  and  $zb\langle 1\bar{1}0 \rangle$  are calculated with the tight binding model considering *s, p* orbitals of Zn and S atoms as well as *s* orbital of passivants as the basis functions. Fig. 4.10, shows the variation of band gaps of  $wz\langle 0001 \rangle$  with respect to its bulk band gap of 3.44 eV (HSE06) as a function of their lateral dimensions (radius) for four different thicknesses consisting of 2,4,6 and 8 monolayers. On the other hand, the radii is varied from 3 Å to the Bohr exciton radius (25 Å) as it is the bulk limit of ZnS semiconductors. Each of the curves in Fig. 4.10, clearly shows that the band gap decreases as the radius of the nanoplatelet increases. This variation of band gap with radius suggest that as the radius of the nanoplatelet increases, the quantum confinement in the lateral direction becomes smaller and as a result of this band gap decreases. For example, Fig. 4.10 shows that the values of band gaps at radius of 3 Å with thickness 4-monolayers is 6.58 eV which is much larger compared to its bulk band gap of 3.44 eV. It is also observed that, beyond a radius of 15 Å, much less than the Bohr exciton radius, the variation of band gaps are small. This implies that beyond this radius, the quantum confinement effect is very small in the lateral direction. In contrast, near the small radii region, the electrons and holes are confined in all three directions (x,y and z) and as we go to higher radii, the confinement in the lateral direction (x and y) of the nanoplatelets

continuously decreases and we have only confinement in the z-direction. So, we move from the regime of three-dimensional confinement to one where one has one-dimensional confinement.

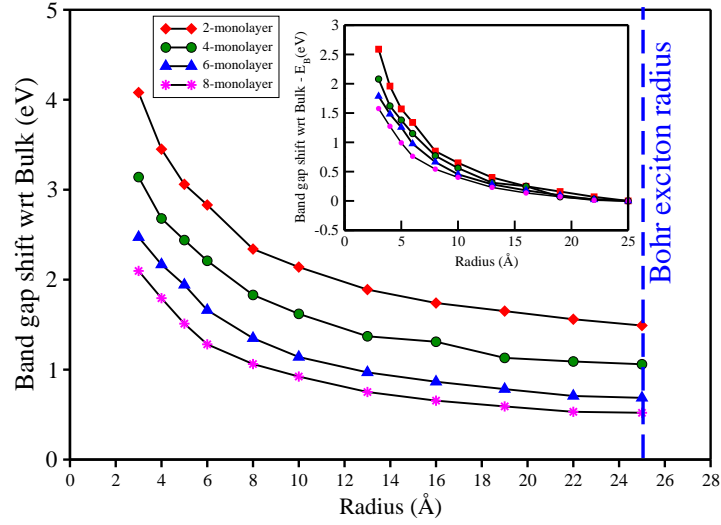


Figure 4.10: Variation of band gap of  $wz\langle 0001 \rangle$  nanoplatelets with respect to the bulk band gap as a function of their lateral dimension for thicknesses of 2, 4, 6 and 8-monolayers. In the inset the variation of band gap shift is shown by subtracting the band gap at Bohr exciton radius ( $E_B$ ).

In the inset of Fig. 4.10 the variation of band gap shift of  $wz\langle 0001 \rangle$  with different thicknesses is shown as a function of their lateral dimension subtracting out the contribution of confinement ( $E_B$ ) in the growth direction. The contribution to the band gap due to confinement in the growth direction is taken as the value at the Bohr exciton radii for a given thickness. This is subtracted out from the band gap shift and plotted in the inset of Fig. 4.1. This subtraction results in the collapse of the curves for different thicknesses onto each other. This indicates the separation of the confinement potential, in the growth direction as well as in the lateral directions and this effect is most prominent above a radius of  $\sim 15 \text{ \AA}$ .

As, we move on to band gap variation of  $zb\langle 001 \rangle$  and  $zb\langle 1\bar{1}0 \rangle$  nanoplatelets as a function of lateral dimension (radius) shown in Figs. 4.11 and 4.12 with respect to its bulk band gap (3.34

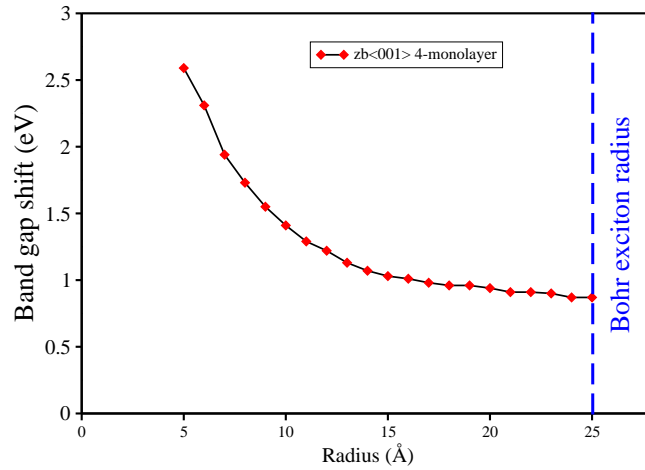


Figure 4.11: Variation of band gap of  $zb\langle 001 \rangle$  nanoplatelet with respect to the bulk band gap as a function of its lateral dimension for thickness of 4-monolayer.

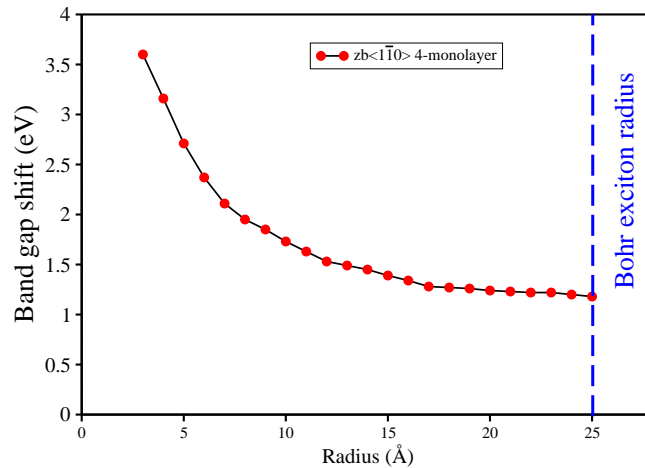


Figure 4.12: Variation of band gap of  $zb\langle 1\bar{1}0 \rangle$  nanoplatelet with respect to the bulk band gap as a function of its lateral dimension for thickness of 4-monolayer.

eV), we find that the band gap decreases as the radii increases which means the trend of band gap variation is similar to  $wz\langle 0001 \rangle$ . Similar explanation holds for these case of  $zb\langle 001\bar{1}0 \rangle$  and  $zb\langle 1\bar{1}0 \rangle$  nanoplatelets which have the band gaps of 4.21 eV and 4.52 eV at the radii of 25 Å. The values of band gaps for the above mentioned nanoplatelets at their smallest sizes are 5.93 eV (radius=5 Å) and 6.94 eV (radius=3 Å). So, in these cases also, near the small size region,

the excitons are confined in three dimensions and as the radii increases the confinement effect decreases. Near the Bohr exciton radii, the carriers are confined only in only one direction i.e. along the growth directions ( $\langle 001 \rangle$  and  $\langle 1\bar{1}0 \rangle$ ). So, we see that there is a 3-D to 1-D quantum confinement occurs as a function of lateral dimension of the nanoplatelets.

## 4.4 Conclusion

We have considered a real space tight binding model to study the size dependence of the band gap of ZnS nanoplatelets. Confinement in both the lateral directions as well as the vertical direction have been examined. Although one has small variations in the band gap as the Bohr exciton radius of ZnS is approached in the lateral direction, significant changes in the band gap are seen due to confinement in the growth direction. We consider platelets with different number of layers in the growth direction and show that subtracting out the contribution from confinement in the growth direction results in the curves collapsing onto each other. This indicates the separability of the potential in the growth direction present even in a fully atomistic calculation.

# Bibliography

- [1] S. Ithurria and B. Dubertret, *J. Am. Chem. Soc.* **130**, 16504 (2008).
- [2] L. L. Chang and K. H. Ploog, *In Proceedings of the 1983 Summer School*, Erice, Italy (1983); L. L. Chang, K. Ploog, Eds.; Martinus Nijhoff: Leiden, The Netherlands (1985).
- [3] Z. Y. Tang, Z. L. Zhang, Y. Wang *et al.*, *Science* **314**, 274 (2006).
- [4] J. Yoon, S. Jo, I. S. Chun *et al.*, *Nature* **465**, 329 (2010).
- [5] P. Podsiadlo, G. Krylova, B. Lee *et al.*, *J. Am. Chem. Soc.* **132**, 8953 (2010).
- [6] M. Li, J. C. Li and Q. Jiang, *Int. J. Mod. Phys. B* **24**, 2297 (2010).
- [7] N. Pradhan and X. Peng, *J. Phys. Chem. Lett.* **129**, 3339 (2007).
- [8] A. Hazarika, A. Layek, S. De *et al.*, *Phys. Rev. Lett.* **110**, 267401 (2013).
- [9] S. Ithurria, M. D. Tessier, B. Mahler *et al.*, *Nature Mater.* **10**, 936 (2011).
- [10] C. Bouet, M. D. Tessier, S. Ithurria *et al.*, *Chem. Mater.* **25**, 1262 (2013).
- [11] J. Joo, J. S. Son, S. G. Kwon *et al.*, *J. Am. Chem. Soc.* **128**, 5632 (2006).
- [12] J. S. Son, K. Park, S. G. Kwon *et al.*, *Small* **8**, 2394 (2012).
- [13] G. Bergerhoff and I. D. Brown, *Crystallographic Databases*; F. H. Allen, G. Bergerhoff and R. Sievers, Eds.; International Union of Crystallography: Chester, U.K. (1987).
- [14] K. A. Shiraishi, *J. Phys. Soc. Jpn.* **59**, 3455 (1990).

- [15] G. Kresse and D. Joubert, Phys. Rev. B **59**, 1758 (1999).
- [16] G. Kresse and J. Furthmuller, Phys. Rev. B **54**, 11169 (1996).
- [17] J. P. Perdew and A. Zunger, Phys. Rev. B **23**, 5048 (1981).
- [18] J. Heyd, G. E. Scuseria, and M. Ernzerhof, J. Chem. Phys. **118**, 8207 (2003).
- [19] J. C. Slater and G. F. Koster, Phys. Rev. **94**, 1498 (1954).
- [20] P. Mahadevan, N. Shanthi and D. D. Sarma, Phys. Rev. B **11**, 199 (1996).
- [21] W. A. Harrison, *Electronic structure and the properties of solids: the physics of the chemical bond*, Dover, New York, USA, (1967).
- [22] *Numerical Data and Functiona/ Relationships in Science and Technology*, Landolt-Bornstein, New Series Group III, Vol. 17a and 22a, edited by K.-H. Hellwege and O. Madelung (Springer, New York, 1982).

# Chapter 5

## A Microscopic Model for the Strain Driven Direct to Indirect Band gap Transition in Monolayer MoS<sub>2</sub> and ZnO

### 5.1 Introduction

The isolation of the first two dimensional crystal, graphene [1] [2], generated a huge interest in the study of these materials. A major focus of the research on graphene has been on possible applications in the electronics industry [3] [4] [5] with the approach to tune the properties that has been adopted, to be by doping [6]. However, the absence of a band gap has limited its applications and shifted the focus onto several layered transition metal disulphides and diselenides such as MoS<sub>2</sub>, WSe<sub>2</sub> etc. [7] [8] [9] [10] MoS<sub>2</sub> has been found to have a bulk band gap of 1.3 eV [11] which is an indirect one. A single monolayer on the other hand is found to have a direct band gap which is 1.9 eV [12] [13]. Similar thickness dependent changes from a direct band gap semiconductor to an indirect band gap one have been seen in other materials such as (Mo/W)X<sub>2</sub>(X=S, Se, Te) [14] and ZnO [15]. Recently strain has been shown to be an important parameter in tuning the band gap. Varying the strain from 0% to 9%, the magnitude

of the band gap has been found to change by almost 1 eV or more in MoS<sub>2</sub> [16], depending on the choice of the exchange-correlation functionals used. In addition a strain dependent direct to indirect band gap transition was found even at a modest value of the strain [17] [18]. The strain dependent direct to indirect band gap transition have been seen in other transition metal dichalcogenides also [19].

In this chapter we consider the case of two materials - MoS<sub>2</sub> and ZnO which represent contrasting limits of their behavior under biaxial tensile strain at the monolayer limit and study the variation of the band gap. In both cases one has a direct band gap at zero strain. Under biaxial tensile strain, a transition is found to take place at just 0.83% in MoS<sub>2</sub> to an indirect band gap material. However a strain of 8% is required in the case of ZnO. Modest values of strain for bringing about the crossover are preferable for use in various devices, and so it would be useful to have a microscopic understanding of the differences in the critical strain required in the two systems.

In order to understand this, we mapped the *ab-initio* band structure onto a tight binding model. The highest occupied band at  $\Gamma$  point in MoS<sub>2</sub> is found to emerge from Mo *d* - S *p* interactions while that at  $\mathbf{K}$  point emerges from Mo *d* - Mo *d* interactions. The fact that we have two different sets of interactions contributing to the highest occupied band at the two symmetry points suggests the role that strain can play in changing the valence band maxima (VBM) position. The distance (*r*) dependence of the hopping interactions are expected to vary as  $1/r^{l+l'+1}$  from an empirical scaling law put forth by Harrison [20]. Here *l* and *l'* are the angular momenta of the orbitals which are involved. Accompanying the strain induced modifications of the interaction strengths, one also has a charge transfer between the atoms involved. Accounting for these two aspects we find that our tight binding model can capture the strain driven direct to indirect band gap transition found in MoS<sub>2</sub>. Moving on to the case of ZnO, we find that the highest occupied band at  $\Gamma$  and  $\mathbf{K}$  points are both contributed by Zn *d*-O *p* interactions. Hence, as the same set of interactions contribute to both symmetry points, tunability to the extent possible in MoS<sub>2</sub> cannot be achieved here, as biaxial tensile strain modifies the energies of the VBM at both symmetry points to almost the same extent. Hence the present paper provides a facile route to identify systems which can be suitable for

band gap engineering via strain. The ideas are then tested for three other systems- MoSe<sub>2</sub>, WSe<sub>2</sub> and BN with success in each case.

## 5.2 Methodology

The electronic structure of MoS<sub>2</sub> and ZnO are calculated within a plane wave implementation of density functional theory using VASP [21] code. The experimental crystal structure [22] has been taken in the case of MoS<sub>2</sub> and a vacuum of 20 Å is used between successive MoS<sub>2</sub> monolayers to minimize interactions between images in the periodic supercell method that we use. While the lattice parameters are kept fixed at the experimental values [22], the internal positions are optimized in each case. Projected augmented wave potentials [23] [24] [25] are used to solve the electronic structures self-consistently using a k-points mesh of 12×12×1. PBE [26] potentials are used for the exchange-correlation functionals and the calculations are performed as a function of biaxial tensile strain. The transition from direct to indirect band gap semiconductor are contrasted with the results for ZnO monolayer. We have used the experimental lattice constant,  $a = 3.099$  Å for a monolayer of ZnO [27]. The details of the calculations are similar to what is done for MoS<sub>2</sub> except that one use LDA+ $U$  potentials with a  $U$  of 8 eV on the Zn  $d$ -states. A  $U$  of 8 eV has been found to be necessary [28] for correcting the self-interaction error. In the absence of this correction, one has a significant admixture of Zn  $d$  states in the valence band. The *ab-initio* band structure calculated at 0% biaxial tensile strain as well as at 2% biaxial tensile strain for MoS<sub>2</sub> are mapped onto a tight binding model for carrying out further analysis.

In order to determine the appropriate basis functions to be included on Mo and S, the Mo  $s, p, d$  as well as S  $s, p, d$  contributions to the partial density of states are shown in Fig. 7.2. We find that the dominant contributions are from Mo  $d$  as well as S  $p$  states with non-zero contributions from other states. Initially we considered a model with Mo  $d$  and S  $p$  states in the basis. The radial parts of the basis functions are considered to be maximally localized Wannier functions [29]. All onsite energies and hopping interaction strengths in this case are determined

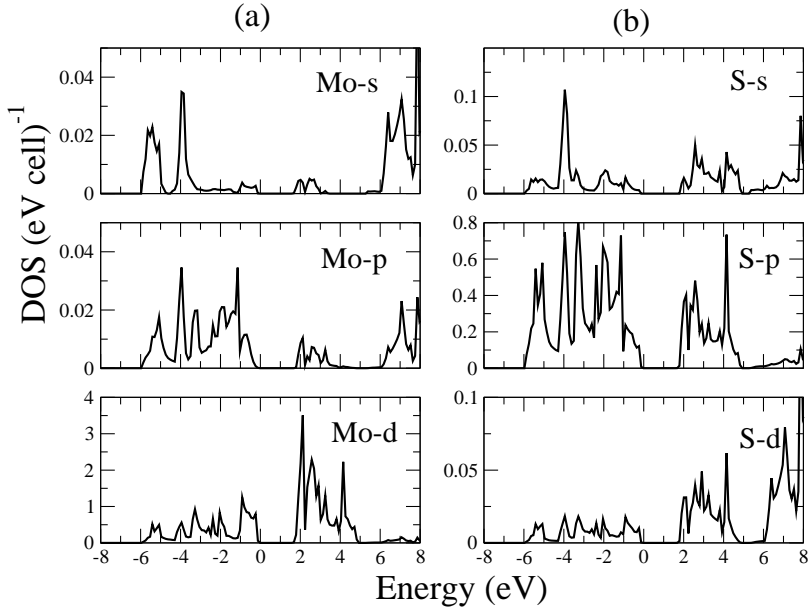


Figure 5.1: The atom and angular momentum projected partial density of states for (a) Mo and (b) S atoms from *ab-initio* calculations using GGA potentials. Zero of energy corresponds to the Fermi energy.

from the interface of VASP to Wannier90 [30]. While an excellent mapping of the *ab-initio* band structure is obtained within the model Hamiltonian, one found that the extracted values of the hopping interaction strengths depended on the pair of orbitals considered, making a mapping onto a consistent set of Slater-Koster parameters difficult. In another model that we considered, we included the Mo *s, p, d* as well as the S *s, p, d* states in the basis. The tight binding parameters are determined by a least-square error minimization. A Harrison's type scaling [20] of the hopping integrals of the form  $1/r^{l+l'+1}$  has been assumed for the Mo *d* - Mo *d* as well as the Mo *d* - S *p* interactions for deviations upto 0.1 Å about the distance at which the hopping interaction strength is defined. The ideas built from our analysis for ZnO and MoS<sub>2</sub> are used to examine the band gap dependence under strain of MoSe<sub>2</sub> [31], WSe<sub>2</sub> [31] as well as BN [32]. The experimental lattice constants used are 3.254 Å, 3.325 Å and 2.511 Å for MoSe<sub>2</sub>, WSe<sub>2</sub> and BN respectively.

### 5.3 Results and Discussions

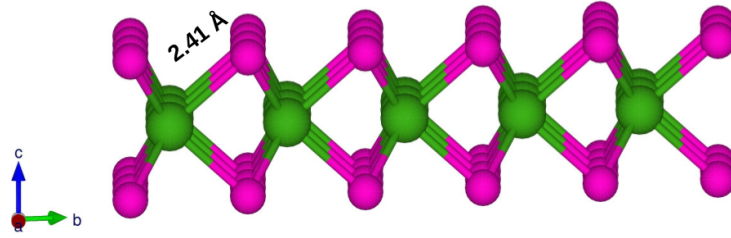


Figure 5.2: Crystal structure of a monolayer of  $\text{MoS}_2$  where Mo and S atoms are shown by green and magenta colours.

The structure of monolayer  $\text{MoS}_2$  is shown in Fig. 5.2. The Mo-S and Mo-Mo(S-S) bond-lengths at the experimental lattice constants are found to be 2.41 Å and 3.16 Å.

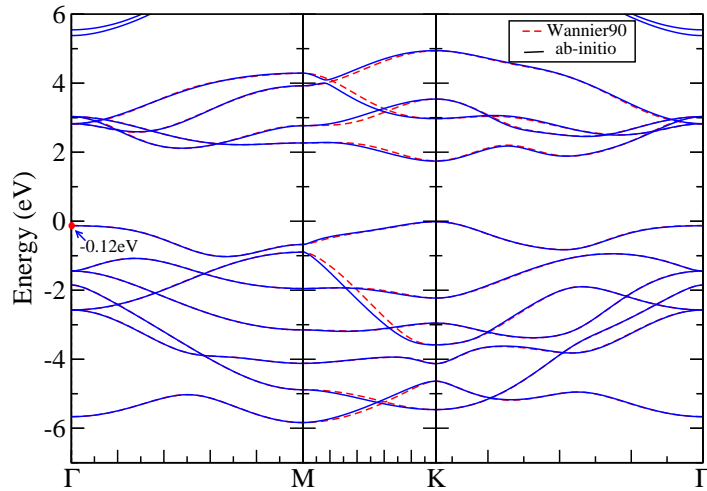


Figure 5.3: *Ab-initio* band dispersions (solid line) for monolayer  $\text{MoS}_2$  at its experimental lattice constant (0% biaxial tensile strain), using GGA potentials. The fitted tight binding bands (dashed line), using a basis consisting of Mo  $d$  and S  $p$  have been superposed. Here the radial part of the tight binding basis functions correspond to maximally localized Wannier functions. The zero of energy is the valence band maximum.

The band dispersions calculated along various symmetry directions for monolayer MoS<sub>2</sub> are given in Fig. 5.3. The VBM is found to be at  $\mathbf{K}$  point while the highest occupied band at  $\mathbf{\Gamma}$  is found to be 0.12 eV lower. The conduction band bottom is found to be at  $\mathbf{K}$  point. Hence, consistent with experiment, one finds a direct band gap of 1.76 eV in MoS<sub>2</sub> in our calculations. This value is slightly underestimated from the experimental value of 1.9 eV [12] [13]. Although an underestimation of the band gap is a well-known drawback of the density functional theory based calculations, the small underestimation here seems fortuitous.

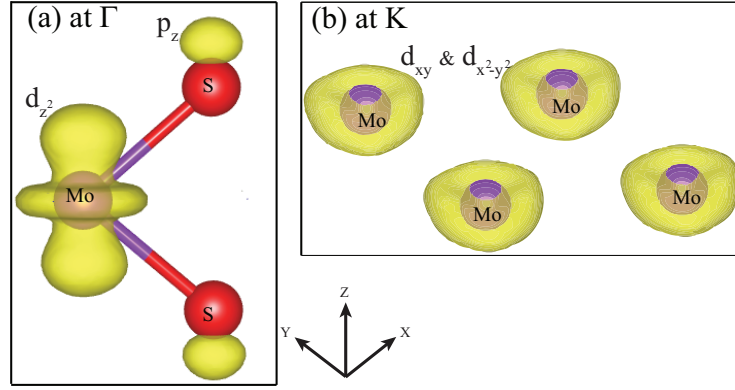


Figure 5.4: The charge density plot for monolayer MoS<sub>2</sub> for the highest occupied band at (a)  $\mathbf{\Gamma}$  and (b) at  $\mathbf{K}$  symmetry points obtained from *ab-initio* calculations using GGA potentials at 0% strain.

We then go on to examine the nature of the interactions that contribute to the VBM at both symmetry points  $\mathbf{\Gamma}$  and  $\mathbf{K}$ . This is done by examining the charge density at these two symmetry points. As evident from Fig. 5.4(a), the highest occupied band at  $\mathbf{\Gamma}$  point is found to emerge from the interactions between the  $d_{z^2}$  orbitals on Mo and the  $p_z$  orbitals on S. The highest occupied band at  $\mathbf{K}$  point is on the other hand derived from direct  $d-d$  interactions between the Mo atoms in the plane which is shown in the Fig. 5.4(b).

We then go on to examine the effect of biaxial tensile strain on the electronic structure of MoS<sub>2</sub>. At a biaxial tensile strain of 2% (Fig. 5.5), we find that the highest occupied band shifts to  $\mathbf{\Gamma}$  while the lowest unoccupied band remains at  $\mathbf{K}$  point. The highest occupied band at  $\mathbf{K}$

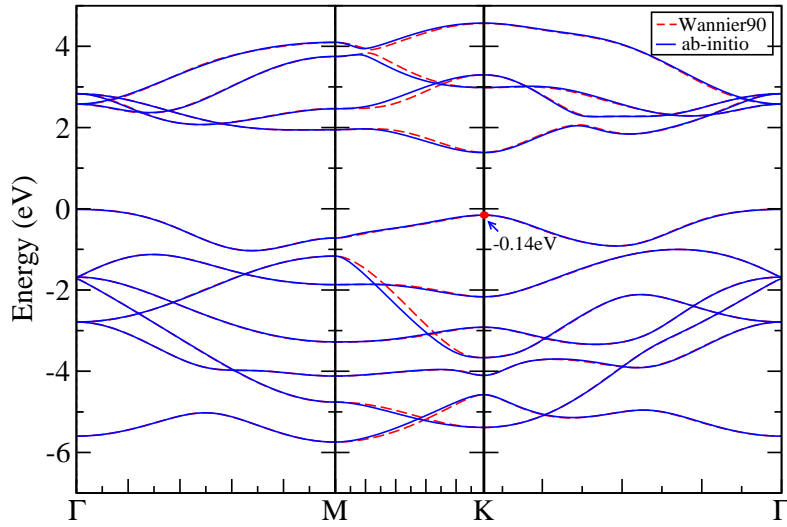


Figure 5.5: *Ab-initio* band dispersions (solid line) for monolayer MoS<sub>2</sub> at its experimental lattice constant (2% biaxial tensile strain), using GGA potentials. The fitted tight binding bands (dashed line), using a basis consisting of Mo *d* and S *p* have been superposed. Here the radial part of the tight binding basis functions correspond to maximally localized Wannier functions. The zero of energy is the valence band maximum.

point is now 0.14 eV lower than that at  $\Gamma$  point. Hence biaxial tensile strain has been found to drive a transition from a direct band gap semiconductor into an indirect band gap one as has been seen earlier [17] [18]. We then go on to examine what are the changes that take place in the bond-lengths under strain. A 2% biaxial tensile strain is found to change the in-plane first neighbor Mo-Mo bond-lengths from 3.16 Å to 3.22 Å, while the Mo-S bond-lengths change only marginally from 2.41 to 2.42 Å. This has the effect of decreasing the Mo-Mo interactions while not having any effect on the Mo-S interaction. As a result, the highest occupied band at  $\mathbf{K}$  point, which is derived from Mo-Mo interactions moves deeper into the valence band and is no longer the location of the VBM for the system. As a result we have the observed transition from a direct to an indirect band gap semiconductor.

In order to understand the role of various microscopic interactions in bringing about the crossover, we have used the VASP to Wannier90 interface to map the *ab-initio* band structure onto a tight binding model with Mo *d* and S *p* states as the basis functions. The fitted tight binding bands are superposed on the *ab-initio* bands in both Figs. 5.3 and 5.5 for the unstrained case as well as the 2% strained case. In both cases, one finds that one has a good description of the *ab-initio* band structure within the tight binding model. The wave function corresponding to the highest occupied band at  $\mathbf{K}$  point is found to have 38% weight on Mo  $d_{x^2-y^2}$  and 40% on  $d_{xy}$  within our tight binding model. At  $\Gamma$  point the weight is found to be 64% on Mo  $d_{3z^2-r^2}$  and the remaining is on S  $p_z$  orbitals. We go on to analyze which are the microscopic interactions that are responsible for the system becoming an indirect band gap semiconductor. While at 0% biaxial tensile strain, the VBM at  $\mathbf{K}$  point is 0.12 eV higher than that at  $\Gamma$  point, one finds that under 2% biaxial tensile strain the VBM at  $\Gamma$  point is 0.14 eV higher than that at  $\mathbf{K}$  point. Hence we have a net movement of 0.26 eV of the energy at  $\Gamma$  point with respect to the energy at  $\mathbf{K}$  point. Using the tight binding Hamiltonian for the unstrained case we find that replacing the onsite energies with those obtained in the 2% strained case gives us a relative shift of 0.06 eV, just 25% of the observed shift. Using a Harrison type scaling of the hopping interaction strengths as well as the modified onsite energies does not give us the required shift that one finds in the *ab-initio* calculations. Closer analysis reveals that the hopping interaction strengths have a complicated distance dependence. However it is

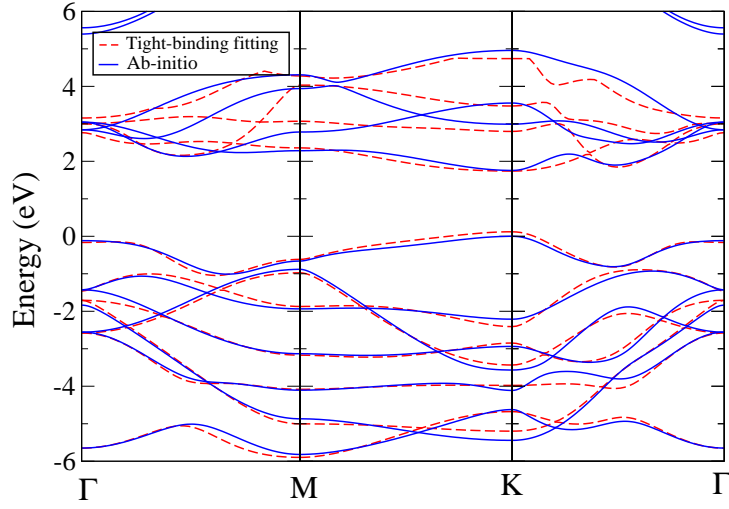


Figure 5.6: Comparison of *ab-initio* band dispersions (solid line) for monolayer MoS<sub>2</sub> at its experimental lattice constant (0% biaxial tensile strain), using GGA potentials and the fitted tight binding bands (dashed line), using a basis consisting of Mo *s,p,d* and S *s,p,d* states. The zero of energy is the valence band maximum.

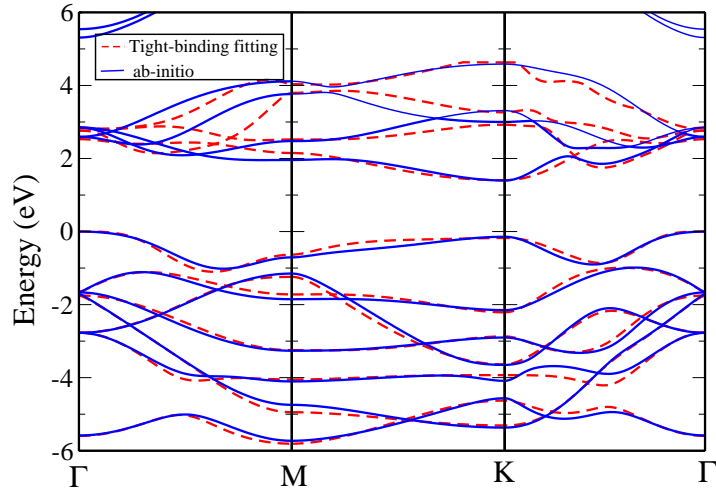


Figure 5.7: Comparison of *ab-initio* band dispersions (solid line) for monolayer MoS<sub>2</sub> at its experimental lattice constant (2% biaxial tensile strain), using GGA potentials and the fitted tight binding bands (dashed line), using a basis consisting of Mo *s,p,d* and S *s,p,d* states. The zero of energy is the valence band maximum.

clear from this analysis that they contribute to 75% of the energy lowering bringing about the change from a direct band gap semiconductor to an indirect band gap one.

We then go on to examine if the deviations from a Harrison-type scaling law [20] found in the tight binding model using maximally localized Wannier functions as the basis, is a consequence of using a limited set of basis states which includes Mo  $d$  and S  $p$  states. In order to examine that we considered a tight binding model with Mo  $s, p, d$  as well as S  $s, p, d$  states in the basis. The *ab-initio* band structure as well as the tight binding band structure are given in Fig. 5.6 for 0% strain. A similar analysis is done for 2% strain also where we kept the Mo  $d$  - S  $p$  as well as Mo  $d$  - Mo  $d$  interactions fixed at their zero strain values and allowed them to scale with distance according to a Harrison-type scaling law. Other parameters are allowed to vary within reasonable limits. The fitted parameters are given in Table 6.1 for the 0% case and in Table 5.2 for the 2% case considered. Here  $E_s$ ,  $E_p$  and  $E_d$  are the onsite energies for the  $s$ ,  $p$  and  $d$  levels on the atoms considered. The hopping interaction strengths have been parametrized in terms of the Slater-Koster parameters for Mo-Mo ( $E(Mo, Mo)$ ), Mo-S ( $E(Mo, S)$ ) and S-S ( $E(S, S)$ ). A comparison of the band structure from the tight binding calculation with the *ab-initio* band structure for 2 % is shown in Fig. 5.7, and a good fit has been obtained. This shows that the strain driven direct to indirect band gap transition can be described in terms of scaling of the interaction strengths assuming a dependence that was first proposed by Harrison.

Table 5.1: Parameters obtained from least-square error fitting of the *ab-initio* band structure onto a tight binding model using *s, p, d* orbitals of Mo and S for monolayer MoS<sub>2</sub> at 0% biaxial tensile strain. The energies are in eV.

	$E_s$	$E_p$	$E_d$
S	3.99	6.91	2.06
Mo	6.85	-3.32	9.01
	$E(Mo,Mo)$	$E(Mo,S)$	$E(S,S)$
<i>ss</i> $\sigma$	-0.83	-2.13	-0.10
<i>sp</i> $\sigma$	1.45	2.23	0.17
<i>sd</i> $\sigma$	-0.13	-0.98	-0.01
<i>pp</i> $\sigma$	0.01	1.72	0.30
<i>pp</i> $\pi$	-0.95	-1.00	-0.20
<i>pd</i> $\sigma$	-0.07	-3.81	-0.89
<i>pd</i> $\pi$	0.02	3.26	0.01
<i>dd</i> $\sigma$	-0.17	-3.28	-0.07
<i>dd</i> $\pi$	0.01	2.34	0.50
<i>dd</i> $\delta$	-0.15	-0.26	-0.97
<i>ps</i> $\sigma$	-1.45	-0.18	-0.17
<i>ds</i> $\sigma$	-0.13	-0.50	-0.00
<i>dp</i> $\sigma$	0.07	2.84	0.89
<i>dp</i> $\pi$	-0.02	-1.05	-0.00

Table 5.2: Parameters obtained from least-square error fitting of the *ab-initio* band structure onto a tight binding model using *s, p, d* orbitals of Mo and S for monolayer MoS<sub>2</sub> at 2% biaxial tensile strain. The energies are in eV.

	$E_s$	$E_p$	$E_d$
S	3.55	6.65	2.18
Mo	6.02	-3.82	8.72
	$E(Mo,Mo)$	$E(Mo,S)$	$E(S,S)$
<i>ss</i> $\sigma$	-0.98	-2.34	-0.01
<i>sp</i> $\sigma$	1.41	2.01	0.20
<i>sd</i> $\sigma$	-0.01	-0.80	-0.01
<i>pp</i> $\sigma$	0.01	1.51	0.41
<i>pp</i> $\pi$	-1.03	-0.94	-0.20
<i>pd</i> $\sigma$	-0.15	-3.91	-0.80
<i>pd</i> $\pi$	0.00	3.39	0.02
<i>dd</i> $\sigma$	-0.17	-3.41	-0.41
<i>dd</i> $\pi$	0.01	2.52	0.33
<i>dd</i> $\delta$	-0.15	-0.16	-0.99
<i>ps</i> $\sigma$	-1.41	-0.40	-0.20
<i>ds</i> $\sigma$	-0.01	-0.22	-0.00
<i>dp</i> $\sigma$	0.15	2.84	0.80
<i>dp</i> $\pi$	-0.01	-1.05	-0.02

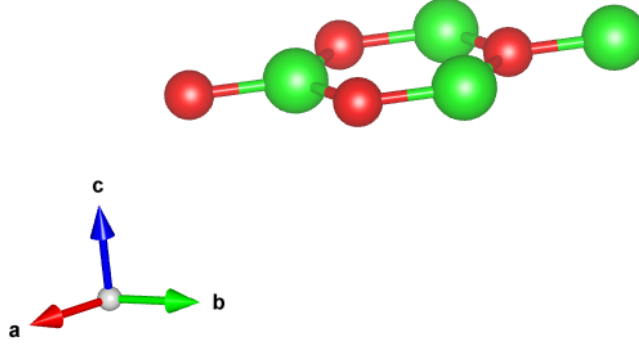


Figure 5.8: Crystal structure of a monolayer of ZnO where Zn and O atoms are shown by green and red colours.

To compare with MoS<sub>2</sub> we considered another layered material, ZnO. This has recently been shown to exist in a metastable phase [27] and few monolayers on various substrates have been found to favor a graphitic phase [33]. The structure of monolayer ZnO is shown in Fig. 5.8. The band dispersions are plotted in Fig. 5.9, along various symmetry directions for monolayer of ZnO. Here also we find that it is a direct band gap material with its VBM at  $\Gamma$  point. The lowest unoccupied band is also at  $\Gamma$  point and we find a band gap of 2.71 eV. This is underestimated from the value of 3.25 eV obtained from hybrid functional calculations, which we compare with in the absence of experimental information for the band gap. However we do not perform hybrid functional calculations as a function of strain as it has been seen earlier [15] that qualitative aspects are captured by LDA+*U* calculations which are computationally less demanding. The large separation of 0.60 eV between the highest occupied band at  $\Gamma$  point and that at  $\mathbf{K}$  point immediately suggests that strain cannot be used as a parameter to tune the band gap so effectively here.

Examining the character of the highest occupied band at  $\Gamma$  point and that at  $\mathbf{K}$  point we find that the band at  $\Gamma$  point is contributed by Zn *d* - O *p* interactions involving the in-plane Zn *d* orbitals and *p<sub>x</sub>/p<sub>y</sub>* orbitals on oxygen. The  $\mathbf{K}$  point on the other hand is contributed by Zn *d<sub>3z<sup>2</sup>-r<sup>2</sup></sub>* orbitals interacting with *p<sub>z</sub>* orbitals on oxygen as is evident from the charge density plotted in Fig. 5.10. Both symmetry points are contributed by interactions between the Zn

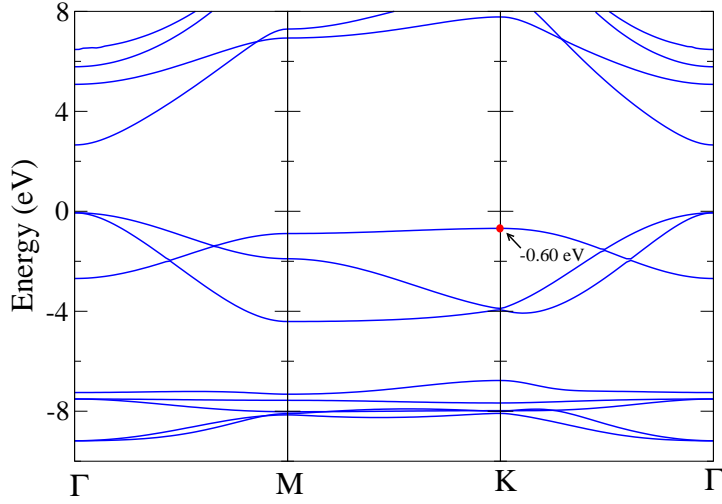


Figure 5.9: *Ab-initio* band dispersions for monolayer ZnO within LDA+ $U$ ,  $U=8$  eV at its experimental lattice constant. The zero of energy is the valence band maximum.

$d$  and O  $p$  orbitals. So as there are similar shifts expected with biaxial tensile strain at both symmetry points, one finds that the strain tunability is small.

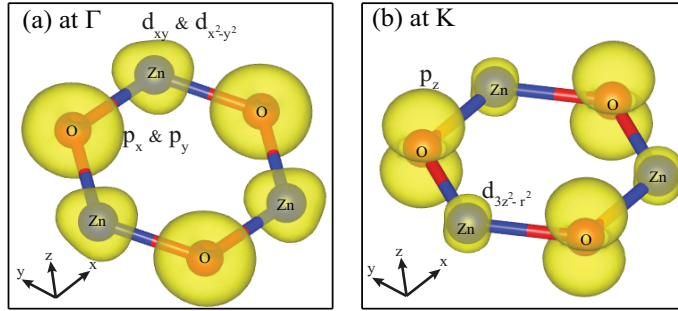


Figure 5.10: The charge density plot for monolayer ZnO for the highest occupied band at (a) $\Gamma$  and (b) at  $\mathbf{K}$  high symmetry points. obtained from *ab-initio* calculations using LDA+ $U$ ,  $U=8$  eV potentials at 0% strain.

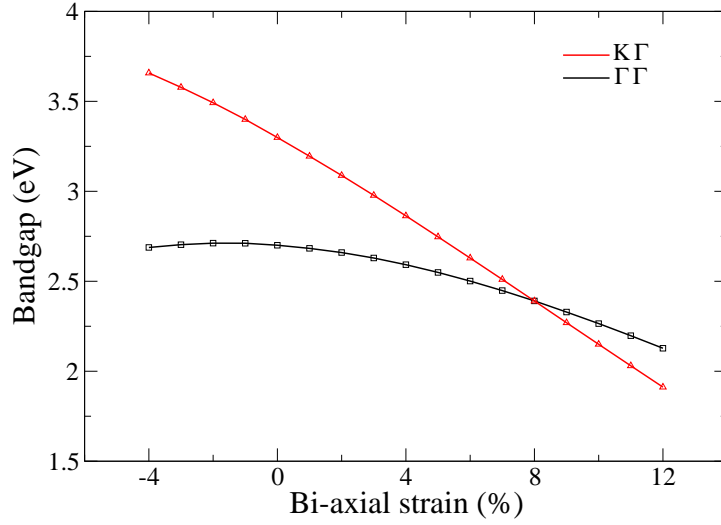


Figure 5.11: The variation of the direct and the indirect band gap for monolayer ZnO at various biaxial tensile strain obtained within *ab-initio* calculations using LDA+U, U=8 eV potentials.

In Fig. 5.11 we have plotted the energy gap as a function of biaxial tensile strain for the case where the highest occupied band at  $\mathbf{K}$  point is considered in addition to the conduction band bottom is at  $\mathbf{\Gamma}$  point. This is denoted as the energy gap  $\mathbf{K}\mathbf{\Gamma}$ . We have also plotted the direct band gap at  $\mathbf{\Gamma}\mathbf{\Gamma}$  between the highest occupied band at  $\mathbf{\Gamma}$  and the lowest unoccupied band also at  $\mathbf{\Gamma}$  point. Upto a biaxial tensile strain of 8% one finds that the direct band gap is smaller than the indirect one. The  $\mathbf{K}\mathbf{\Gamma}$  energy gap becomes the smaller band gap for values of biaxial tensile strain greater than 8%. We have calculated the phonon spectrum at a strain percentage of 10% which is shown in Fig. 5.12 and we find the phonon modes to be positive. This indicates that the structure is stable even when subjected to such a large strain.

The study for MoS<sub>2</sub> and ZnO have provided a simple route to systems in which band gap engineering from a direct to an indirect band gap semiconductor is possible. We consider two other systems MoSe<sub>2</sub> and WSe<sub>2</sub> which have a structure similar to MoS<sub>2</sub> and find that at the experimental lattice parameters, the highest occupied band (VBM) at  $\mathbf{\Gamma}$  and  $\mathbf{K}$  point differ by 0.365 and 0.42 eV (Table 5.3). Hence a modest strain of  $\sim 3\%$  (Table 5.3) is able to bring about

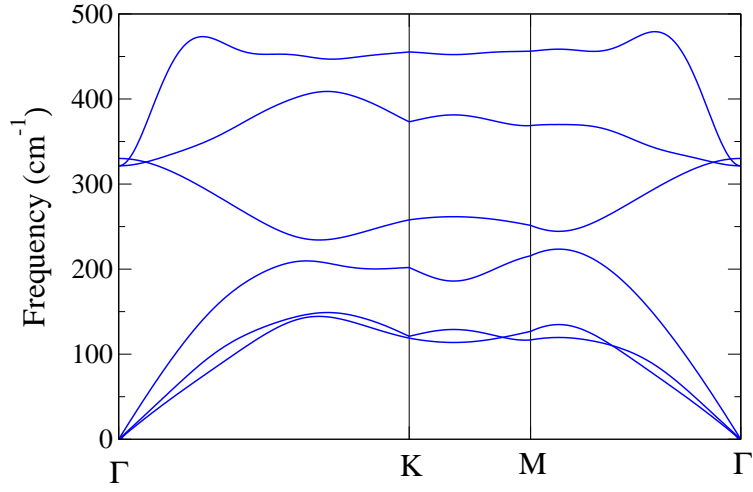


Figure 5.12: The calculated phonon dispersion for ZnO at 10% biaxial tensile strain along various symmetry directions.

Table 5.3: Strain percentage at which the band gap crossover takes place and the energy difference of the VBM/CBM at  $\Gamma$  ( $E(\Gamma)$ ) and  $\mathbf{K}$  ( $E(\mathbf{K})$ ) at 0% strain of MoSe<sub>2</sub>, WSe<sub>2</sub> and BN monolayer. The energies are in eV.

<i>System</i>	<i>Strain Percentage</i>	$E(\Gamma)$ - $E(\mathbf{K})$
MoSe <sub>2</sub> monolayer	$\sim 3\%$	0.365 (VBM)
WSe <sub>2</sub> monolayer	$\sim 3\%$	0.420 (VBM)
BN monolayer	$\sim 2\%$	-0.094 (CBM)

the transition from a direct band gap semiconductor to an indirect band gap one. While at first sight, the differences in the two systems studied could be directly linked to the structure involved, we consider the third case to be BN which has a structure similar to ZnO which we have studied earlier. In contrast to ZnO, here we find that the lowest unoccupied band (CBM) at  $\Gamma$  point is 0.094 eV lower than the CBM at  $\mathbf{K}$  point using the experimental lattice parameters. However from an analysis of the character of these points we find that the  $\Gamma$  point is contributed by interactions between N-*s* states, while one finds that the  $\mathbf{K}$  point emerges from B-*p* interactions. Hence as the hopping interaction strengths scale as  $1/r^{l+l'+1}$ , the CBM at  $\Gamma$  and  $\mathbf{K}$  move at different rates under strain. Hence a transition is found at a modest value of strain of 2%.

## 5.4 Conclusion

We have considered one monolayer of two semiconductors MoS<sub>2</sub> and ZnO both of which exhibit a direct to indirect band gap transition under biaxial tensile strain. While a small biaxial tensile strain of 0.83% drives the transition in MoS<sub>2</sub>, a much larger biaxial tensile strain of 8% is required in the case of ZnO. This is traced to the nature of interactions determining the highest occupied band at  $\Gamma$  and  $\mathbf{K}$  points. While Mo *d* - S *p* interactions contribute to the valence band maximum at  $\Gamma$  point, Mo *d* - Mo *d* interactions contribute to the VBM at  $\mathbf{K}$  point. Strain modifies the hopping interaction strengths and therefore brings about the transformation from a direct band gap material to an indirect band gap one. A scaling of the hopping interaction strengths according to Harrison's scaling law within a tight binding model for MoS<sub>2</sub> is able to capture the effect. In ZnO as the VBM at both symmetry points are determined by Zn *d* - O *p* interactions, the scaling is not as effective and requires a much larger strain to bring about the transition. Hence a simple design principle emerges in the choice of systems for band gap engineering by strain.

# Bibliography

- [1] K. S. Novoselov, A.K. Geim<sup>1</sup>, S.V. Morozov *et al.*, Science **306**, 666 (2004).
- [2] A. H. C. Neto, F. Guinea, N.M.R. Peres *et al.*, Rev. Mod. Phys. **81**, 109 (2009).
- [3] Y. Wu, Y. -M. Lin, A. A. Bol *et al.*, Nature **472**, 74 (2011).
- [4] Y. -M. Lin, K. A. Jenkins, A. Valdes-Garcia *et al.*, Nano Lett. **9**, 422 (2009).
- [5] Y. -M. Lin, C. Dimitrakopoulos, K. A. Jenkins *et al.*, Nature **327**, 662 (2010).
- [6] X. Miao, S. Tongay, M. K. Petterson *et al.*, Nano Lett. **12**, 2745 (2012).
- [7] B. Radisavljevic, A. Radenovic, J. Brivio *et al.*, Nature Nanotec. **6**, 147 (2011).
- [8] Y. Zhang, J. Ye, Y. Matsushashi *et al.*, Nano Lett. **12**, 1136 (2012).
- [9] Z. Yin, H. Li, H. Li *et al.*, ACS Nano **6**, 74 (2012).
- [10] H. Fang, S. Chuang, T. C. Chang *et al.*, Nano Lett. **12**, 3788 (2012).
- [11] G. L. Frey, S. Elani, M. Homyonfer *et al.*, Phys. Rev. B **57**, 6666 (1998).
- [12] C. Lee, H. Yan, L. E. Brus *et al.*, ACS Nano **4**, 2695 (2010).
- [13] A. Splendiani, L. Sun, Y. Zhang *et al.*, Nano Lett. **10**, 1271 (2010).
- [14] W. S. Yun, S. W. Han, S. C. Hong *et al.*, Phys. Rev. B **85**, 033305 (2012).
- [15] B. Rakshit and P. Mahadevan, Appl. Phys. Lett. **102**, 143116 (2013).

- [16] J. Feng, X. Qian, C. -W Huang *et al.*, Nature Photonics **6**, 866 (2012).
- [17] H. Shi, H. Pan, Y.-W. Zhang *et al.*, Phys. Rev. B **87**, 155304 (2013).
- [18] P. Johari and V.B. Shenoy, ACS Nano **6**, 5449 (2012).
- [19] S. Horzum, H. Sahin, S. Cahangirov *et al.*, Phys. Rev. B **87**, 125415 (2013).
- [20] W. A. Harrison, *Electronic structure and the properties of solids: the physics of the chemical bond*, (Dover, New York, USA, 1967).
- [21] G. Kresse and J. Furthmüller, Phys. Rev. B **54**, 11169 (1996).
- [22] R. Murray and B. Evans, J. Appl. Cryst. **12**, 312 (1979).
- [23] G. Kresse and D. Joubert, Phys. Rev. B **59**, 1758 (1999).
- [24] P.E. Blöchl, Phys. Rev. B **50**, 17953 (1994).
- [25] G. Kresse and D. Joubert, "From ultrasoft pseudopotentials to the projector augmented wave method", Phys. Rev. B **59**, 1758 (1999).
- [26] J. Paier, R. Hirschl, M. Marsman *et al.*, J. Chem. Phys. **122**, 234102 (2005).
- [27] C. L. Pueyo, S. Siroky, S. Landsmann *et al.*, Chem. Mater. **22**, 4263 (2010).
- [28] S. Zh. Karazhanov, P. Ravindran, A. Kjekshus *et al.*, Phys. Rev. B **75**, 155104 (2007).
- [29] A. A. Mostofi, J. R. Yates, Y.-S. Lee *et al.*, Comput. Phys. Commun. **178**, 685 (2008).
- [30] C. Franchini, R. Kováčik, M. Marsman *et al.*, J. Phys.: Condens. Matter **24**, 235602 (2012).
- [31] G. B. Liu, W. Y. Shan, Y. Yao *et al.*, Phys. Rev. B **88**, 085433 (2013).
- [32] M. Topsakal, E. Aktürk, and S. Ciraci, Phys. Rev. B **79**, 115442 (2009).
- [33] C. Tusche, H. L. Meyerheim and J. Kirschner, Phys. Rev. Lett. **99**, 026102 (2007).

# Chapter 6

## A Model for the Direct to Indirect Band gap Transition in Monolayer MoSe<sub>2</sub> as a Function of Strain

### 6.1 Introduction

Layered transition metal sulphides and selenides have been widely studied since the 1960s for wide ranging applications which include their use as a dry lubricant [1], in catalysis [2], photovoltaics [3] as well as batteries [4]. The recent interest in graphene [5] [6] [7] has brought the focus onto these materials which have the advantage of being semiconducting in addition to being layered. Interestingly, in each of these materials while the single layer is a direct band gap material [8] [9], the bilayer and beyond become indirect band gap materials [10] [9]. Indirect band gap materials are suitable for various applications such as photovoltaics [3] where one would like to bring about the spatial separation of the generated electron-hole pair. Considering a monolayer of MoS<sub>2</sub> we have shown that a modest strain of 2% [11], is sufficient to bring about the transition from a direct band gap semiconductor to an indirect band gap one. Analyzing the charge density in the unstrained case it is found that the valence band maximum (VBM)

which is at  $\mathbf{K}$  point is contributed by Mo  $d$ -Mo  $d$  interactions while the highest occupied band at  $\mathbf{\Gamma}$  point is contributed by Mo  $d$ -S  $p$  interactions. Under strain one can change the Mo-Mo distances while keeping the Mo-S separation almost unchanged. As the hopping interaction strengths for electrons on orbitals with angular momenta  $l$  and  $l'$  respectively vary as  $1/r^{l+l'+1}$  according to an empirical law referred to as Harrison's scaling law [12], it is shown that a scaling of the hopping interaction strengths with distance could explain the direct to indirect band gap transition. There are several other reports which demonstrate the band gap transformation from direct to indirect in monolayer transition metal sulphides and selenides as a function of strain. For instance, P. Johari *et al.* [13] have shown for MoS<sub>2</sub>, MoSe<sub>2</sub>, WS<sub>2</sub> and other transition metal disulphides and selenides that by applying a modest value of biaxial strain can reduce the band gaps causing a direct( $\mathbf{KK}$ ) to indirect ( $\mathbf{\Gamma K}$ ) band gap and a semiconductor-to-metal transition.

This model was first applied to MoS<sub>2</sub> [11] and is extended to MoSe<sub>2</sub> in the present chapter. The unstrained band structure for this system calculated within *ab-initio* electronic structure calculations is found to reproduce the experimental observation [14] that this system is a direct band gap semiconductor. The VBM is at  $\mathbf{K}$  point and the conduction band bottom (CBM) is also at  $\mathbf{K}$  point. A biaxial strain of 3 % in the case of MoSe<sub>2</sub> is able to bring about a change-over with the band at  $\mathbf{\Gamma}$  point becoming the VBM. We then have a transition from a direct band gap material to an indirect band gap one. In order to model this transition, a tight binding model has been set up for the system. The onsite energies as well as the hopping interaction strengths have been estimated by fitting the *ab-initio* band structure for the unstrained case. The transition metal  $d$ -transition metal  $d$  interaction strengths are allowed to vary with distance according to Harrison's scaling law [12]. This model is able to capture the strain induced direct to indirect band gap transition.

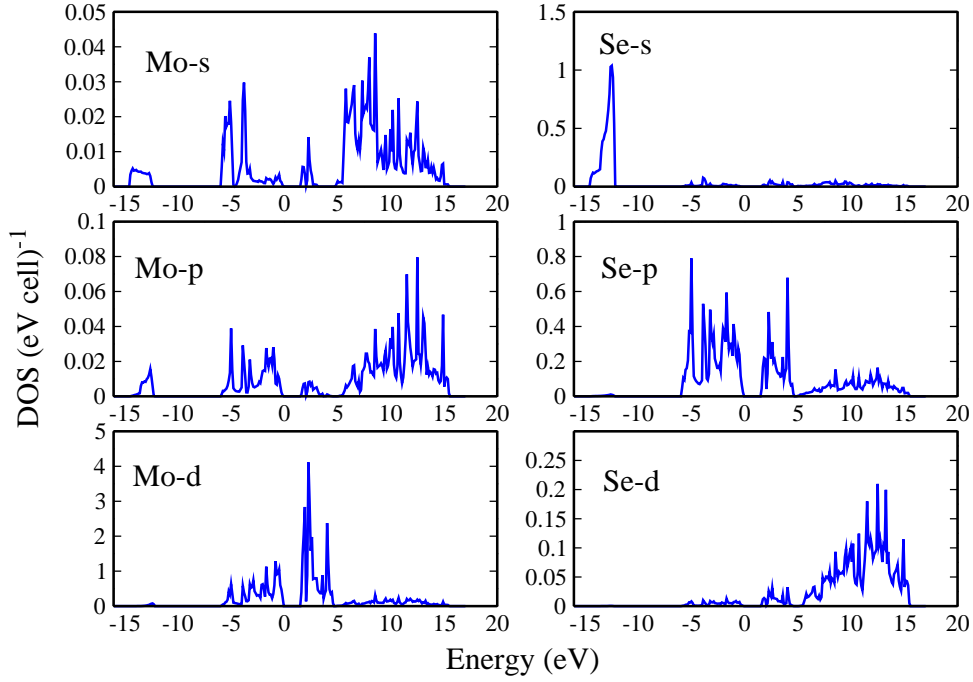


Figure 6.1: The atom and angular momentum projected partial density of states for Mo and Se atoms from *ab-initio* calculations using GGA potentials at 0% strain. The zero of energy corresponds to the valence band maximum.

## 6.2 Methodology

The electronic structure of monolayer MoSe<sub>2</sub> has been calculated within a plane wave implementation of density functional theory using VASP [15] code. The experimental crystal structure [14] has been taken in the case of MoSe<sub>2</sub>. A vacuum of 20 Å is used between successive monolayers to minimize interactions between images in the periodic supercell method that we use for this structure. While the lattice parameters are kept fixed at the experimental values [16], the internal positions are optimized in each case. Projected augmented wave potentials [17] are used to solve the electronic structure self-consistently using a k-points mesh of 12×12×1 with a cutoff energy for the plane wave basis states equal to 280 eV. PBE [18] potentials are used for the exchange-correlation functionals and the calculations are performed as a function of biaxial tensile strain.

For the microscopic analysis of the band gap transformation, in this chapter, we have developed a tight binding model for the monolayer MoSe<sub>2</sub> to map the *ab-initio* results onto this. In order to determine the appropriate basis for the tight binding model, the Mo and Se partial density of states are shown in Fig. 6.1. The zero of energy is the Fermi energy. One finds that the Mo *d* states contribute in the energy window 5 eV below the Fermi energy and upto 5 eV above the Fermi energy. The Mo *s* and Mo *p* states are more extended and so their weight in any given energy window is low. However our earlier work [11] has shown that to get a good description of the *ab-initio* band structure in a wide energy window from 10 eV below the Fermi level to around 5 eV above, one needs to include the the Mo *s, p, d* states in the basis. The Se *s* states are around 12 eV below the Fermi level, with Se *p* states contributing dominantly in the region of interest. Se *d* states are found to contribute in the energy window beyond 5 eV above the Fermi level. We therefore include Se *s, p, d* states in the basis for the tight binding model considered. The tight-binding parameters are determined by a least-square error minimization [19]. Similar to monolayer MoS<sub>2</sub>, for the strained case, a Harrison's type scaling [12] of the hopping integrals of the form  $1/r^{l+l'+1}$  has been assumed for the Mo *d*-Mo *d* interaction for deviations upto 0.1 Å about the distance at which the hopping interaction strength is defined, while the onsite energies are allowed to vary.

### 6.3 Results and Discussion

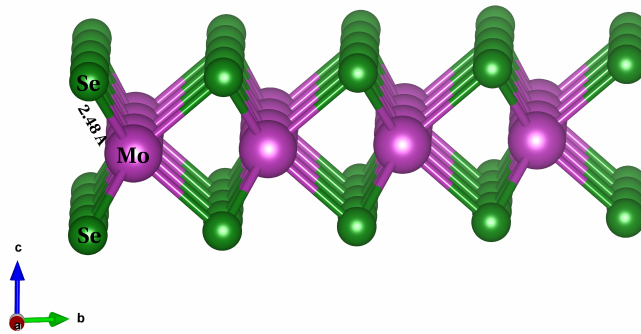


Figure 6.2: Crystal structure of a monolayer of MoSe<sub>2</sub>.

The structure of monolayer MoSe<sub>2</sub> is shown in Fig. 6.2. The Mo-Se and Mo-Mo(S-Se) bond-lengths at the experimental lattice constants [16] are found to be 2.48 Å and 3.25 Å. Under 3 % biaxial tensile strain, the Mo-Se and Mo-Mo (Se-Se) bond-lengths are found to be become 2.52 Å and 3.35 Å. So, the Mo-Se bond-lengths are hardly changing. The *ab-initio* band dispersions for MoSe<sub>2</sub> plotted along various symmetry directions are shown in Fig. 6.3. The calculations capture the semiconducting nature of the compound and find a band gap of 1.59 eV at 0 % strain. This is in reasonable agreement with the experimental value of 1.55 eV [14]. While LDA/GGA calculations are usually found to underestimate the band gap, the agreement is fortuitous.

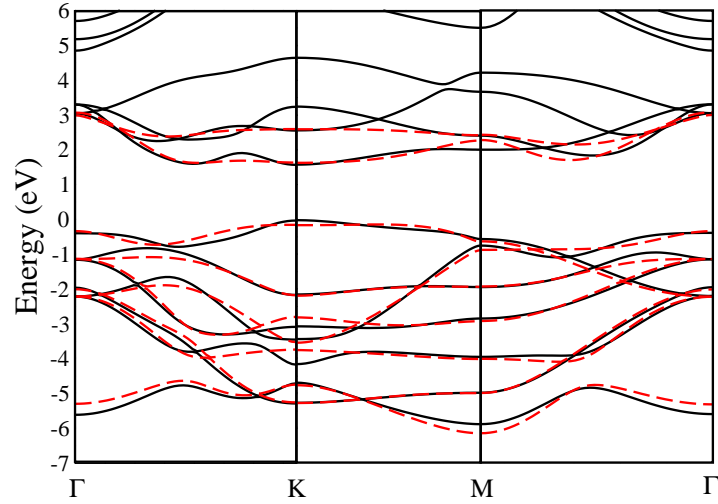


Figure 6.3: Comparison of *ab-initio* band dispersions (solid line) for monolayer MoSe<sub>2</sub> at its experimental lattice constant (0 % biaxial tensile strain), using GGA potentials and the fitted tight binding bands (dashed line), using a basis consisting of Mo *s,p,d* and Se *s,p,d* states. The zero of energy corresponds to the valence band maximum.

The *ab-initio* band structure is fit to a tight binding model discussed earlier in the Methodology section. The parameters entering the tight binding Hamiltonian are determined by a least square error minimization process. Not all bands are considered in this fitting but just all the bands comprising the valence band in the energy window -7 eV to the Fermi energy as well as two bands comprising the conduction band. The *ab-initio* band structure has been shown in

black solid line while the tight binding band structure has been shown in red dashed line in the same figure. The description in this minimal tight binding model is reasonable. The parameters entering the tight binding Hamiltonian are given in Table 6.1. The onsite energies are denoted by  $E_s$  where the subscript corresponds to the orbital involved. For the Mo  $d$  orbitals we found the need to allow for the degeneracy lifting of the  $d$  orbitals. The inter-site hopping interactions have been parametrized in terms of the Slater-Koster parameters and are tabulated for first neighbour Mo-Se sites as well as second neighbour Mo-Mo and Se-Se sites.

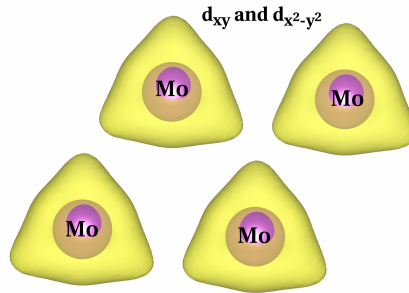


Figure 6.4: The charge density plot for monolayer MoSe<sub>2</sub> for the highest occupied band at  $\mathbf{K}$  point obtained from *ab-initio* calculations using GGA potentials at 0 % strain.

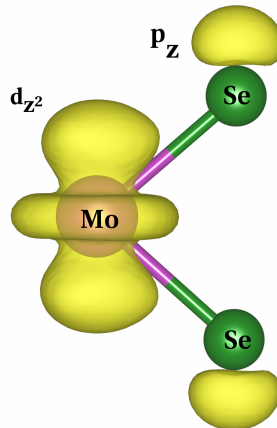


Figure 6.5: The charge density plot for monolayer MoSe<sub>2</sub> for the highest occupied band at  $\Gamma$  point obtained from *ab-initio* calculations using GGA potentials at 0 % strain.

Table 6.1: Parameters obtained from least-squared-error fitting of the *ab-initio* band structure onto a tight binding model using *s, p, d* orbitals of Mo and Se for monolayer MoSe<sub>2</sub> at 0 % biaxial tensile strain. The energies are in eV.

	$E_s$	$E_p$	$E_{d_{xy}}$	$E_{d_{yz}}$	$E_{d_{zx}}$	$E_{d_{x^2-y^2}}$	$E_{d_{z^2}}$
Mo	4.88	8.38	3.76	1.80	1.80	3.76	1.08
Se	-14.55	-4.12	8.45	8.45	8.45	8.45	8.45
	$E(Mo, Mo)$	$E(Mo, S)$	$E(S, S)$				
<i>ss</i> $\sigma$	-0.82	-1.03	-0.20				
<i>sp</i> $\sigma$	0.69	1.84	0.05				
<i>sd</i> $\sigma$	-0.01	-0.72	-0.15				
<i>pp</i> $\sigma$	1.34	1.43	0.97				
<i>pp</i> $\pi$	-0.55	-0.19	-0.13				
<i>pd</i> $\sigma$	-1.29	-1.49	0.00				
<i>pd</i> $\pi$	0.29	3.01	0.49				
<i>dd</i> $\sigma$	-0.54	-3.86	-0.01				
<i>dd</i> $\pi$	0.04	2.31	0.14				
<i>dd</i> $\delta$	-0.01	-0.39	-0.01				
<i>ps</i> $\sigma$	-0.69	-1.20	-0.05				
<i>ds</i> $\sigma$	-0.01	-1.66	-0.15				
<i>dp</i> $\sigma$	0.29	2.56	0.00				
<i>dp</i> $\pi$	-0.29	-0.38	-0.49				

In order to understand the nature of interactions contributing to the VBM at 0 % strain, we have plotted the charge density in Fig. 6.4 corresponding to the eigen value at  $\mathbf{K}$  point. One finds substantial interaction between the in-plane  $d$  orbitals-  $d_{xy}$  and  $d_{x^2-y^2}$  contributing to the eigen value corresponding to the VBM arising from the extended nature of the  $4d$  transition metal atom wave function, so even if separations are as large as  $3.25 \text{ \AA}$ , there is significant interaction. The highest occupied band at  $\Gamma$  point is on the other hand contributed by Mo  $d$ -Se  $p$  interactions involving  $d_{z^2}$  orbitals on Mo and  $p_z$  orbitals on Se which is shown in Fig. 6.5. When we apply biaxial strain, one finds that the Mo- Se bond-length does not try to change, while the Mo- Mo bond is elongated. This immediately suggests a route to modifying the character of the VBM via strain. The Mo  $d$ -Mo  $d$  interactions can be modified when the Mo-Mo separation is increased. The hopping interactions between two orbitals scale inversely with distance according to a power law. Increasing the separation decreases the interaction strength. As the VBM is contributed by antibonding states arising from Mo-Mo interactions, one finds that these states move deeper into the valence band.

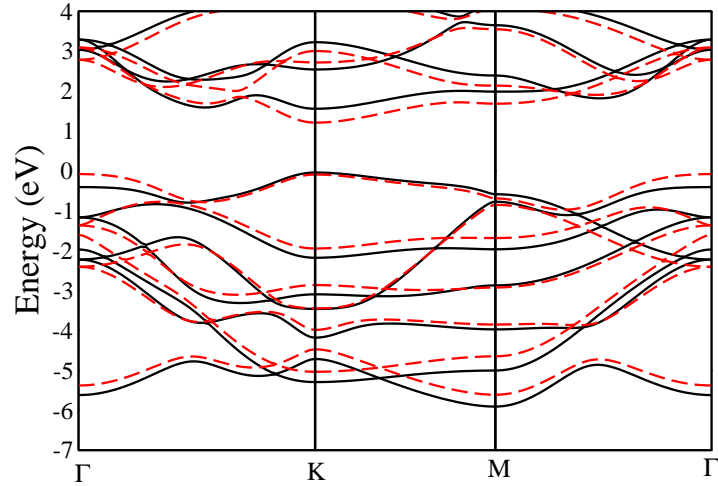


Figure 6.6: Comparison of *ab-initio* band dispersions for monolayer MoSe<sub>2</sub> at its experimental lattice constant at 0 % biaxial tensile strain (solid line) and 3 % biaxial tensile strain (dashed line) using GGA potentials. The zero of energy corresponds to the valence band maximum.

Indeed when we plot the band structure under 3 % strain, we find a crossover of the VBM from  $\mathbf{K}$  to  $\mathbf{\Gamma}$  in Fig. 6.6. In the figure, we superpose the *ab-initio* band dispersions calculated at 0 % strain as well as 3 % strain. As under strain only the second neighbor interaction strengths are affected, one doesn't expect too much change in the band structure with strain. While at first sight, there seem to large differences, shifting the dominantly Se *p* states in the 3 % strain calculation are found to match up with the bands at 0 % strain calculation. Similarly we can shift the bands contributed dominantly by Mo *d* states in the 3 % calculation to those in the unstrained case. This indicates that the large differences emerge from charge transfer between the Mo and Se sites.

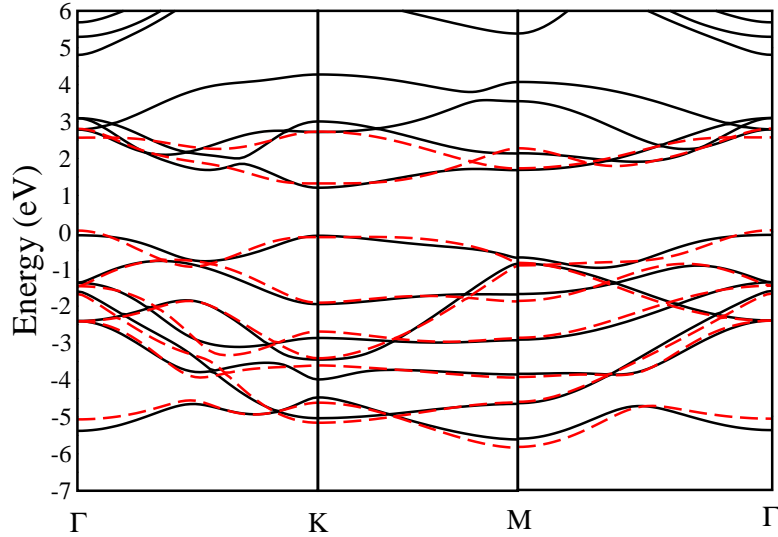


Figure 6.7: Comparison of *ab-initio* band dispersions (solid line) for monolayer  $\text{MoSe}_2$  at its experimental lattice constant (3 % biaxial tensile strain), using GGA potentials and the fitted tight binding bands (dashed line), using a basis consisting of Mo *s, p, d* and Se *s, p, d* states. The zero of energy corresponds to the valence band maximum.

In order to determine the parameters entering the tight binding Hamiltonian at the 3 % strain, we used the extracted parameters at 0 % strain. The onsite energies are allowed to vary, while the hopping interaction strengths are kept fixed at the values of Table 6.1 and are allowed to scale according to Harrison's scaling law [12] discussed earlier. The values of onsite energies

Table 6.2: The onsite energies obtained from least-squared-error fitting of the *ab-initio* band structure onto a tight binding model using *s,p,d* orbitals of Mo and Se for monolayer MoSe<sub>2</sub> at 3 % biaxial tensile strain. The energies are in eV.

	$E_s$	$E_p$	$E_{d_{xy}}$	$E_{d_{yz}}$	$E_{d_{zx}}$	$E_{d_{x^2-y^2}}$	$E_{d_{z^2}}$
Mo	5.23	8.78	4.26	1.99	1.99	4.26	1.54
Se	-14.78	-4.36	6.37	6.37	6.37	6.37	6.37

extracted from the fitting are listed in Table 6.2. The scaling affected the Se-Se as well as Mo-Mo interaction strengths. A comparison of the *ab-initio* band structure and the best fit tight binding band structure are shown in Fig. 6.7. The tight binding model is able to capture the transition from direct into an indirect band gap semiconductor and the valence band maximum is shifted to  $\Gamma$  point.

## 6.4 Conclusion

A monolayer of MoSe<sub>2</sub> is found to be a direct band gap semiconductor. We show, within *ab-initio* electronic structure calculations, that a modest biaxial tensile strain of 3 % is able to drive it into an indirect band gap semiconductor with the valence band maximum (VBM) shifting from  $\mathbf{K}$  point to  $\Gamma$  point. we have set up a realistic tight binding model to discuss the electronic structure of MoSe<sub>2</sub> under strain. The model is able capture the direct to indirect band gap transition with strain.

# Bibliography

- [1] K. H. Hu, X. G. Hu, and X. J. Sun, *Appl. Surf. Sci.* **256**, 2517 (2010).
- [2] W. K. Ho, J. C. Yu, J. Lin *et al.*, *Langmuir* **20**, 5865 (2004).
- [3] E. Fortin and W. Sears, *J. Phys. Chem. Solids* **43**, 881 (1982).
- [4] C. Feng, J. Ma, H. Li *et al.*, *Mater. Res. Bull.* **44**, 1811 (2009).
- [5] K. S. Novoselov, A. K. Geim, S. V. Morozov *et al.*, *Science* **306**, 666 (2004).
- [6] A. H. C. Neto, F. Guinea, N. M. R. Peres *et al.*, *Rev. Mod. Phys.* **81**, 109 (2009).
- [7] Y. Wu, Y. M. Lin, A. A. Bol *et al.*, *Nature* **472**, 74 (2011).
- [8] C. Lee, H. Yan, L. E. Brus *et al.*, *ACS Nano* **4**, 2695 (2010).
- [9] A. D. Yoffe, *Annu. Rev. Mater. Sci.* **3**, 147 (1973).
- [10] G. L. Frey, S. Elani, M. Homyonfer *et al.*, *Phys. Rev. B* **57**, 6666 (1998).
- [11] R. Das, B. Rakshit, S. Debnath and P. Mahadevan, *Phys. Rev. B* **89**, 115201 (2014).
- [12] W. A. Harrison, *Electronic structure and the properties of solids: the physics of the chemical bond*, (Dover, New York, USA, 1967).
- [13] P. Johari and V.B. Shenoy, *ACS Nano* **6**, 5449 (2012).
- [14] S. Tongay, J. Zhou, C. Ataca, K. Lo *et al.*, *Nano Lett.* **12**, 5576 (2012).
- [15] G. Kresse and J. Furthmüller, *Phys. Rev. B* **54**, 11169 (1996).

- [16] T. Böker, R. Severin, A. Müller *et al.*, Phys. Rev. B **64**, 235305 (2001).
- [17] G. Kresse and D. Joubert, Phys. Rev. B **59**, 1758 (1999).
- [18] J. Paier, R. Hirschl, M. Marsman *et al.*, J. Chem. Phys. **122**, 234102 (2005).
- [19] P. Mahadevan, N. Shanthi and D.D. Sarma, Phys. Rev B **54**, 11 199 (1996).

# Chapter 7

## Understanding of the Changeover from Direct to Indirect Band Gap in MoSe<sub>2</sub> and MoS<sub>2</sub> as a Function of Thickness

### 7.1 Introduction

The layered transition-metal dichalcogenides (TMDs) have been investigated for over fifty years now. However, recent interest in this class of materials has been spurred by possible applications in nanoelectronics, photovoltaics, catalysis to name a few [1] [2] [4] [3]. Further advances in the isolation of one or more layers by a process of exfoliation [5] has led to the exploration of the properties of these materials as a function of thickness. Analogous to the nanomaterials where one finds a size dependence of the band gap [6] [7] [8], we find thickness dependent changes in the electronic structure of the layered transition metal dichalcogenides. Additionally one finds a thickness dependent band gap which changes character. The bulk band gap of MoS<sub>2</sub> is found to be an indirect one of 1.3 eV [9] which increases to 1.6 eV in the bilayer limit [10]. The nature of the band gap changes and becomes a direct one of 1.9 eV at the monolayer limit [11]. The fact that the monolayers of transition metal dichalcogenides have a direct band gap is evident

from the sharp peak that one finds in the photoluminescence spectra [12]. MoSe<sub>2</sub> also has an indirect band gap of 1.1 eV [13] in the bulk limit whereas in the monolayer limit it has a direct band gap of about 1.66 eV [14]. There are two types of MX<sub>2</sub> (M = Mo, W, Ti etc., X = S, Se, etc.) sandwiches depending on the coordination of the transition metal atom with the chalcogens. One is 1T-MX<sub>2</sub> where the coordination is octahedral and the other is 2H-MX<sub>2</sub> which is trigonal prismatic. The 1T structure is not as stable as the 2H configuration for the group-VIB TMDs [15]. Additionally there can be several ways in which the monolayers can be stacked. However the coupling between the layers is believed to be arising from van der Waals (vdW) interaction and is consequently weak.

The band gap dependence as a function of thickness is believed to arise from quantum confinement effect with a weak component if any coming from inter-layer interactions. Kuc and coworkers [16] considered MoS<sub>2</sub> and WSe<sub>2</sub> and calculated the electronic structure as a function of thickness. They found that for both materials the fundamental band gap originates from the transition from the top of the valence band at  $\Gamma$  to the bottom of the conduction band halfway between  $\Gamma$  and  $\mathbf{K}$  (referred to as  $\mathbf{T}$  point). This is the case as the thickness is varied from two monolayers to the bulk limit. The optical band gap which is at  $\mathbf{K}$  point on the other hand remains unchanged with a variation in the number of layers. An analysis of the charge density at the valence band maximum (VBM) at  $\Gamma$  as well as the conduction band minimum (CBM) at  $\mathbf{T}$  point reveals that this is contributed by orbitals pointing to the other layer, suggestive of a dominant contribution from inter-layer interactions at these k-points. They however conclude that quantum confinement effects drive the band gap transition from indirect to direct as the number of monolayers is decreased. Padilha and co-workers [17] considered an internal reference for the band gap calculations for MoS<sub>2</sub> performed as a function of thickness. Aligning the energy eigen values with respect to this internal reference, they found that the position of the VBM at  $\Gamma$  increases with respect to vacuum. The CBM at  $\mathbf{K}$  point however remained constant. This clearly shows the effect of quantum confinement on the electronic structure. Zhang and Zunger [18] have examined the evolution of the electronic structure as a function of thickness. They conclude that the indirect to direct band gap transition with thickness has contributions

from both quantum confinement as well as inter-layer interactions and neither alone can be separated out as a cause.

In this chapter, we have studied the variation of the band gap in MoSe<sub>2</sub>, in the bilayer and monolayer limit. The band structures obtained from *ab-initio* electronic structure calculations are found to reproduce the experimental observation [10] that this system is a direct band gap semiconductor in the monolayer limit. But, as we move on to the bilayer limit, the system becomes an indirect band gap material. In our calculations, we find that the CBM shifts from **K** to **T** point as we move on from the monolayer to the bilayer. The VBM on the other hand shifts from **K** to **Γ** point. As discussed earlier, there are two competing effects which bring about the crossover from a direct to an indirect band gap as a function of thickness. The first one is the inter-layer interaction and the other one is the quantum confinement. In order to understand which is the dominant effect in bringing about the band gap crossover, our approach has been to examine the evolution of the electronic structure of MoSe<sub>2</sub> within a tight binding model. We mapped the *ab-initio* band structure onto a tight binding model using Mo *d* and Se *p* as the basis states. Maximally localized Wannier functions are used for the radial parts of these basis functions. The bilayer band structure we find, can be represented by considering the monolayer tight binding Hamiltonian and additionally introducing interactions between the two layers. This model also captures the direct to indirect band gap transition that one finds as a function of thickness in both the materials. Hence a dominant role in bringing about the direct to indirect band gap transition with thickness is played by the inter-layer interactions. Hence our analysis suggests a negligible role played by quantum confinement effects in the electronic structure changes as a function of thickness. The ideas arrived at for MoSe<sub>2</sub> are then tested for another system of MoS<sub>2</sub>, with success in this case also.

## 7.2 Methodology

The electronic structure calculations of bilayer MoSe<sub>2</sub> is carried out within a plane wave implementation of density functional theory (DFT) using the VASP [19] code. We have taken the 2H

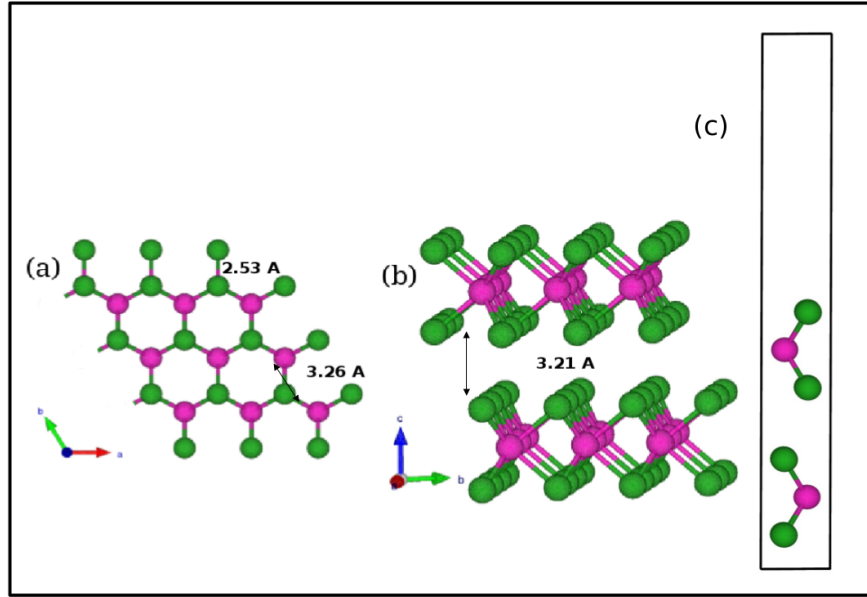


Figure 7.1: Crystal structure of a 2H bilayer of MoSe<sub>2</sub> where magenta and green atoms are Mo and Se atoms respectively. In this figure (a) and (b) show the top and side view of this structure and (c) shows the unit cell.

stacking of MoSe<sub>2</sub> shown in Fig. 7.1 as it is found to be the most stable structure [20]. While, the lattice constants are kept at the experimental values of  $a=3.299$  Å and  $c=12.939$  Å [21], all the atoms are allowed to relax through a total energy minimization that is guided by the calculated atomic forces. A vacuum of 20 Å is used along  $z$  direction to minimize the interaction among the periodic images. Projected augmented wave [22] [23] potentials are used to solve the electronic structure self-consistently using a  $k$ -points mesh of  $12 \times 12 \times 1$  with a cutoff energy for the plane wave basis states equal to 280 eV. Perdew-Burke-Ernzerhof (PBE) [24] potentials are used for the exchange-correlation functionals. The bilayer band structures have also been examined by using local density approximation (LDA). There is a weak van der Waals interaction between the layers which has an effect in the determination of the inter-layer distances. A dispersion correction based on Grimmes DFT-D2 method [25] is used on top of the PBE potentials. All results in this chapter use dispersion corrected LDA/PBE potentials.

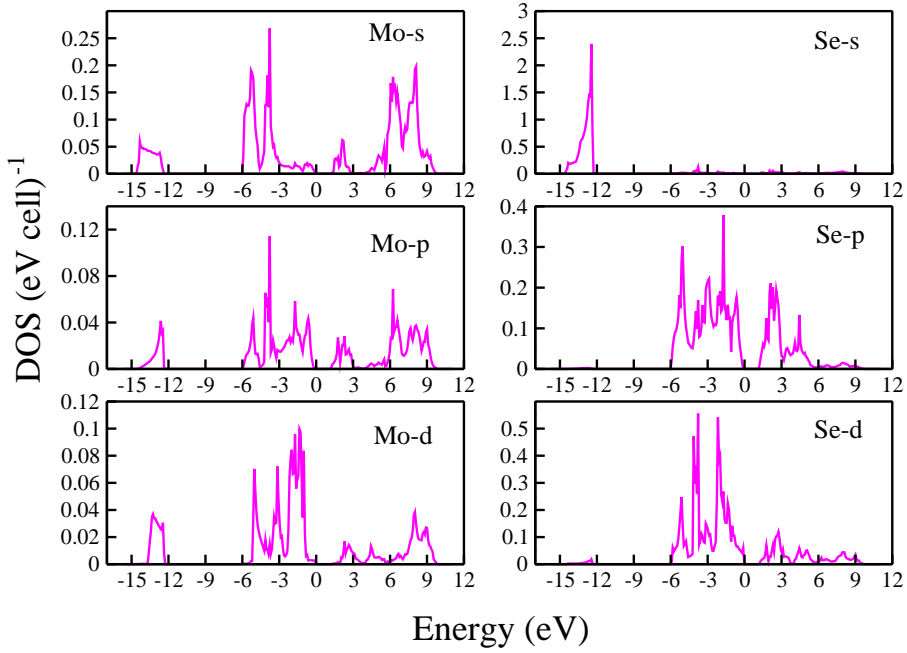


Figure 7.2: The atom and angular momentum projected partial density of states for Mo and Se atoms from *ab-initio* calculations using GGA potentials. Zero of energy corresponds to the Fermi energy.

In this chapter, we have developed a tight binding model for the bilayer  $\text{MoSe}_2$  so that the DFT results can be mapped onto this for further analysis. In order to determine the appropriate basis functions for the tight binding model of bilayer  $\text{MoSe}_2$ , the projected density of states (PDOS) is calculated which is shown in Fig. 7.2. The zero of the energy in Fig. 7.2 corresponds to the VBM. The PDOS shows that the dominant contribution is coming from Mo  $d$  and Se  $p$  states while non-zero contribution is coming from other states. So, we setup the tight binding model with Mo  $d$  and Se  $p$  states in the basis. In this model, the maximally localized Wannier functions [26] represent the most natural choice for the radial parts of the basis functions. Technically, the degree of localisation and the symmetry of these Wannier functions can be controlled in the projection procedure. All on-site energies and hopping interaction strengths in this case are determined from the interface of VASP to Wannier90 [27]. Even if we get an excellent mapping of the *ab-initio* band structure within the tight binding model Hamiltonian,

the extracted values of the hopping interaction strengths are dependent on the pair of orbitals considered which make a mapping onto a consistent set of Slater-Koster parameters difficult.

To get a good description within a Slater-Koster type parametrization scheme, we have developed another tight binding model with Mo  $s, p, d$  as well as Se  $s, p, d$  states as basis functions suggested by our earlier work of monolayer MoSe<sub>2</sub> [28]. The onsite energies considered in this model are those which we extracted from the tight binding fitting of bilayer MoSe<sub>2</sub> using Wannier functions as basis functions. The hopping interaction strengths however, are obtained from the tight binding fitting of the *ab-initio* band structure of monolayer MoSe<sub>2</sub> [28] by a least-square-error minimization procedure [29] and are used as the in-plane hopping interaction strengths for the case of the bilayer MoSe<sub>2</sub>. The in-plane hopping interaction strengths are set as fixed parameters while the inter-layer hopping parameters are determined by a least-square-error minimization procedure in fitting the *ab-initio* bilayer band structure. A Harrison's type scaling law [30] of the hopping integrals of the form  $1/r^{l+l'+1}$  has been assumed for deviations upto 0.2 Å about the distance at which the hopping interaction strength is defined. The ideas built from our analysis for MoSe<sub>2</sub> is used to examine the crossover of band gap as a function of thickness of MoS<sub>2</sub>. The lattice constants used for MoS<sub>2</sub> are  $a=3.16$  Å and  $c=12.296$  Å [31].

### 7.3 Results and Discussion

In the 2H structure of bilayer MoSe<sub>2</sub> shown in Fig. 7.1, each molecular sheet (monolayer) can be viewed as three layer stacking of Mo and Se atoms where Mo atoms are sandwiched between layers of Se atoms. The Se atoms generate a trigonal prismatic crystal field. The stacking has the Mo atom in one layer above that in the layer beneath (as shown in panel (c)) However the Mo-Se motif is rotated by 180° in the layer above with respect to the layer beneath. The monolayers in the unit cell interact with each other through van der Waals forces which is much weaker than the in-plane covalent bonds. The inter-layer separation obtained from the optimization with vdW interaction is 3.21 Å. In the optimized structure, the shortest in-plane

Mo-Se and Mo-Mo (Se-Se) distances are 2.53 Å and 3.26 Å respectively whereas the shortest inter-layer Mo-Se and Se-Se distances are found to be 4.87 Å and 3.72 Å respectively.

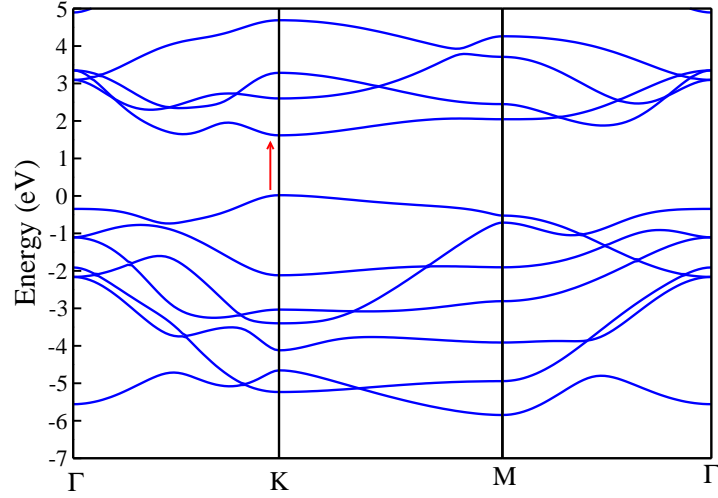


Figure 7.3: The *ab-initio* band dispersion for monolayer MoSe<sub>2</sub> at its experimental lattice constant using GGA potentials. The arrow indicates that band gap is direct. The zero of energy is the valence band maximum.

The *ab-initio* band dispersions of monolayer MoSe<sub>2</sub> with GGA is plotted along various symmetry directions in Fig. 7.3. From the figure it can be clearly seen that in monolayer MoSe<sub>2</sub>, both VBM and CBM are at **K** point which make it a direct band gap semiconductor with a band gap of 1.59 eV [28]. The experimental band gap is found to be 1.66 eV [14]. The agreement between experiment and theory is fortuitous. The k-point association of the VBM and CBM are consistent with earlier reports in the literature [32].

Now, in Fig. 7.4 the *ab-initio* band dispersion of bilayer MoSe<sub>2</sub> with GGA is plotted. The figure shows that the VBM in the bilayer is shifted from **K** to  $\Gamma$  point and the CBM on the other hand is shifted from **K** to **T** point which leads to an indirect band gap of 1.25 eV. This band gap is underestimated compared to the experimental band gap of 1.55 eV [10]. Theoretical studies of the bilayer transition metal dichalcogenides (MoSe<sub>2</sub>, MoS<sub>2</sub>) suggest that the k-point association of the VBM and CBM depend on whether dispersion-corrected potentials are used

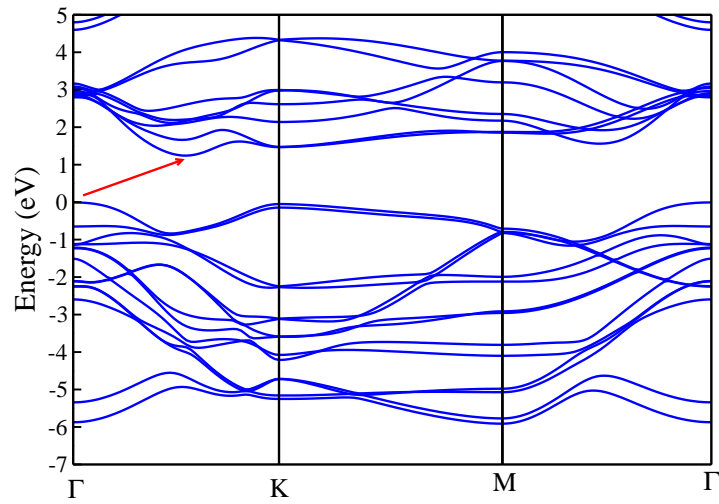


Figure 7.4: The *ab-initio* band dispersion for bilayer MoSe<sub>2</sub> at it's experimental lattice constant using GGA potentials. The arrow indicates that band gap is indirect. The zero of energy is the valence band maximum.

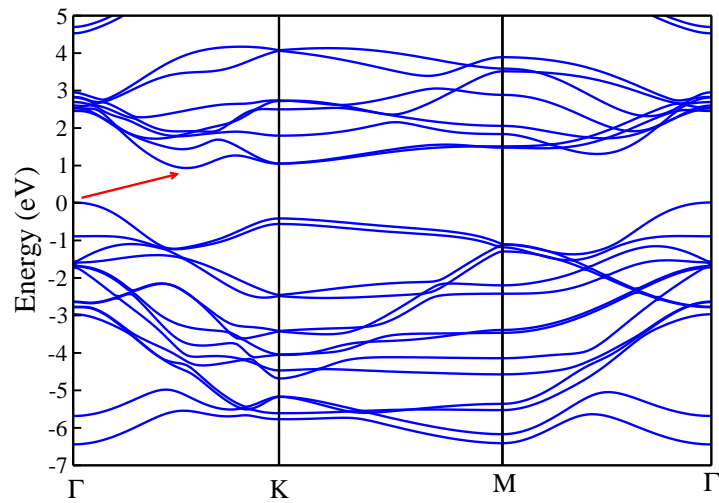


Figure 7.5: The *ab-initio* band dispersion for bilayer MoSe<sub>2</sub> at it's experimental lattice constant using LDA potentials. The arrow indicates that band gap is indirect. The zero of energy is the valence band maximum.

or not. For instance, L. Debbichi *et al.* [32] have shown that bilayers of MoS<sub>2</sub> and MoTe<sub>2</sub> have an indirect band gap with the VBM located at  $\Gamma$  and the CBM at  $\mathbf{T}$  using GGA for the exchange-correlation functionals and Tkatchenko-Scheffler (DFT-TS) for incorporating the vdW interaction. The same trend of VBM and CBM is observed in free-standing bilayer MoSe<sub>2</sub> by A. J. Bradley [33] using the *ab-initio* GW method including the effect of vdW which agrees well with their experimental results. On the other hand, S. W. Han *et al.* [34] have shown that VBM and CBM of MoS<sub>2</sub> shift from  $\mathbf{K}$  to  $\Gamma$  and  $\mathbf{T}$  point as one goes from monolayer to the bulk performing in full-potential linearized augmented plane wave (FLAPW) method using GGA. According to them, for bilayer, the CBM at  $\mathbf{T}$  is slightly higher than at  $\mathbf{K}$ . So, the k-points making up the VBM and CBM of bilayer MoSe<sub>2</sub>, observed in our calculation agrees well with the literature. We have also plotted the band structure of bilayer MoSe<sub>2</sub> using LDA in Fig. 7.5 to show that the band structure remain qualitatively unchanged even if the exchange-correlation functional differs.

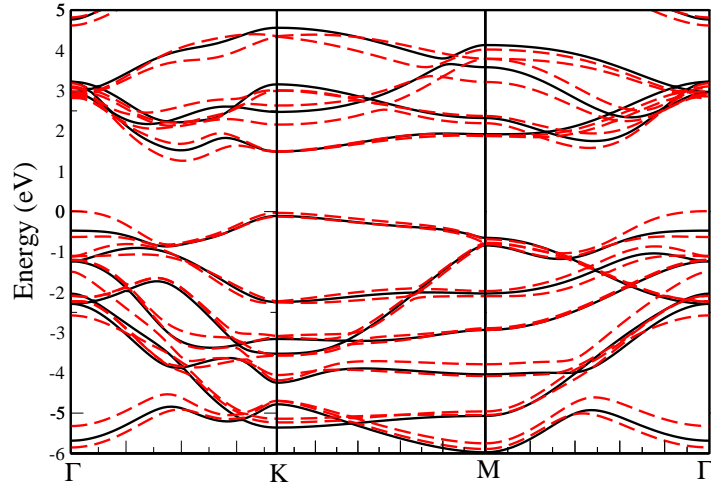


Figure 7.6: Comparison of *ab-initio* band dispersions for monolayer MoSe<sub>2</sub> (black solid line) and bilayer MoSe<sub>2</sub> (red dashed line) at its experimental lattice constant using GGA potentials. The zero of energy is the valence band maximum.

The comparison of *ab-initio* band dispersions of monolayer and bilayer MoSe<sub>2</sub> is plotted along various symmetry directions in Fig. 7.6. These two band structures are similar in every

direction except at the position of the VBM and CBM. Looking at the figures it is clear that the difference of lowest unoccupied bands at  $\mathbf{K}$  and the  $\mathbf{T}$  point is found to be -0.031 eV and 0.234 eV for monolayer and bilayer MoSe<sub>2</sub> respectively. It is known that bilayer MoSe<sub>2</sub> differs from monolayer only in one respect which is the presence of inter-layer interactions between the layers. So, the small difference between the above two band structures implies that this inter-layer interactions are very weak.

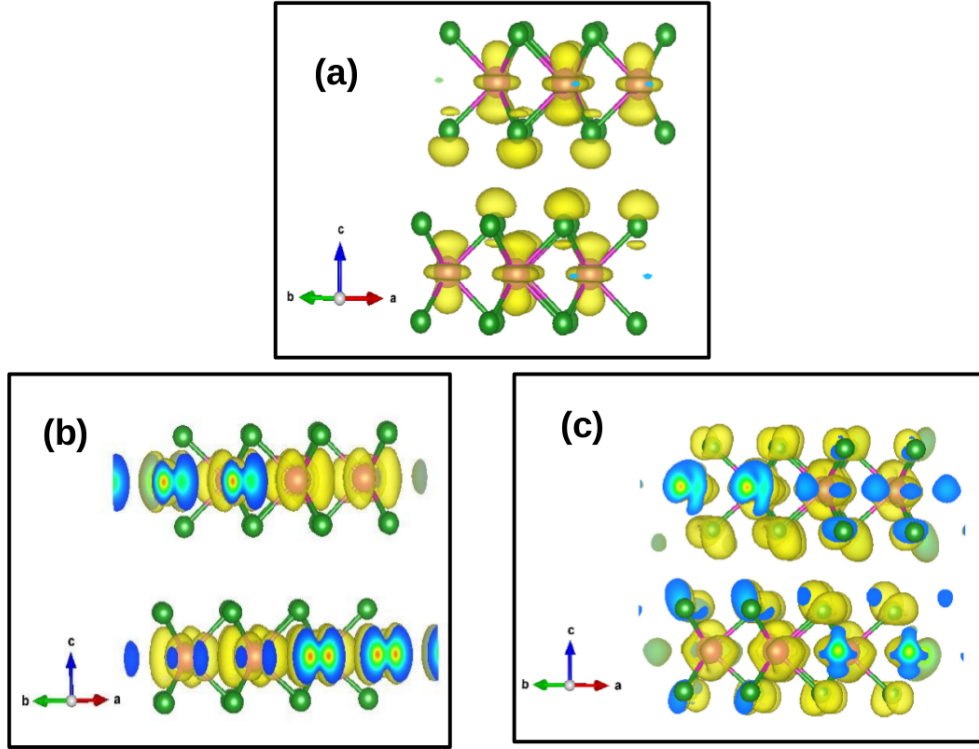


Figure 7.7: The charge density plot for bilayer MoSe<sub>2</sub> for the highest occupied band at (a)  $\Gamma$  and and for the lowest unoccupied band at (b)  $\mathbf{K}$  and (c)  $\mathbf{T}$  symmetry points obtained from *ab-initio* calculations using GGA potentials.

Now, to understand the nature of interactions of the VBM for bilayer MoSe<sub>2</sub>, we have plotted the charge density at  $\Gamma$  in Fig. 7.7(a). This shows that the VBM is contributed by Mo  $d_{z^2}$  and Se  $p_z$  orbitals in each monolayer are pointing to each other. On the other hand, to examine the character of the lowest unoccupied at  $\mathbf{K}$  and that band at  $\mathbf{T}$ , we have plotted the charge densities in Figs. 7.7(b) and 7.7(c) respectively. From the plots, one finds that the lowest

unoccupied band at  $\mathbf{T}$  emerges mainly from the interactions between Mo  $d_{z^2}$  orbitals while at  $\mathbf{K}$  point, it is derived mainly from the interactions of Mo  $d_{xy}$ ,  $d_{x^2-y^2}$  and Se  $p_x$ ,  $p_y$  orbitals. So, from the charge density analysis, it can be inferred that the inter-layer interactions play a major role in bringing about the direct to indirect band gap crossover from monolayer to bilayer MoSe<sub>2</sub>.

In order to understand the role of various microscopic interactions in bringing about the direct to indirect band gap crossover in MoSe<sub>2</sub> as a function of thickness, we have carried out a tight binding calculation with Mo  $d$  and Se  $p$  states as basis functions to map the *ab-initio* band structure of both monolayer and bilayer structures using VASP to Wannier90 interface. The fitted tight binding bands are superposed on the *ab-initio* bands in Figs. 7.8 and 7.9 along various symmetry directions for monolayer [28] and bilayer MoSe<sub>2</sub> respectively. In both the cases, it is clearly seen that we have an excellent mapping of the *ab-initio* band structures onto the tight binding model which suggests a good description of the *ab-initio* band structure within a tight binding model. The onsite energies extracted from these fittings are listed in Table 7.1 for monolayer and bilayer MoSe<sub>2</sub>. The energies of all the orbitals in table 7.1 are given with respect to the Se  $p_x$  orbital in each case of monolayer and bilayer as this orbital is in plane and is least affected by the quantum confinement effects. From these energies, one finds that all Mo  $d$  and Se  $p$  states of bilayer move higher than the respective states in monolayer except the Se  $p_z$  orbital. It can be observed that the Se  $p_z$  state of bilayer MoSe<sub>2</sub> is pushed to deeper energies due to the charge transfer between the layers. However, these changes are very small. This result implies that there is a negligible effect of quantum confinement effect in the band gap crossover from direct to indirect.

So far, we have observed that the inter-layer interaction and the charge transfer between the layers are the two effects which brings about the transformation from direct to indirect band gap semiconductor in MoSe<sub>2</sub> as a function of thickness. Now, we need to understand which is the dominant effect of the above mentioned effects for bringing about the band gap transformation in MoSe<sub>2</sub> as a function of thickness. To get a quantitative idea of the effect of inter-layer interaction, we have switched off all the inter-layer interactions in the real space Hamiltonian of bilayer MoSe<sub>2</sub> obtained from VASP to Wannier90 interface. Surprisingly, we find that, after

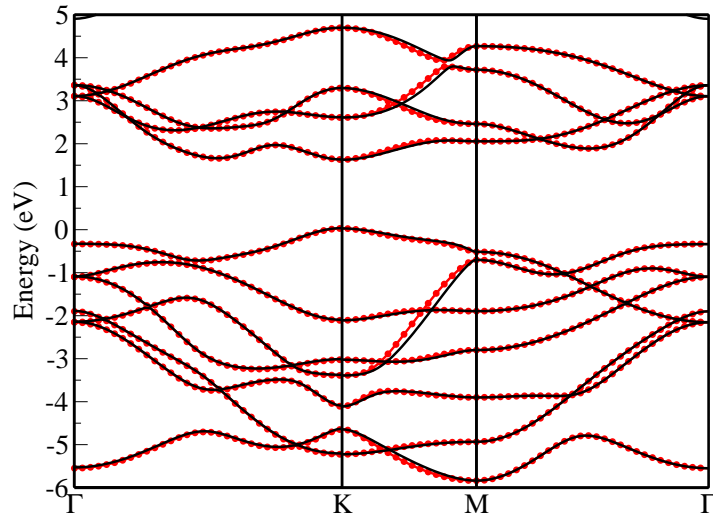


Figure 7.8: Comparison of *ab-initio* band dispersions (black solid lines) for monolayer MoSe<sub>2</sub> at its experimental lattice constant, using GGA potentials and the fitted tight binding bands (line with red circle), using a basis consisting of Mo *d* and Se *p* states. Here the radial part of the tight binding basis functions correspond to maximally localized Wannier functions. The zero of energy is the valence band maximum.

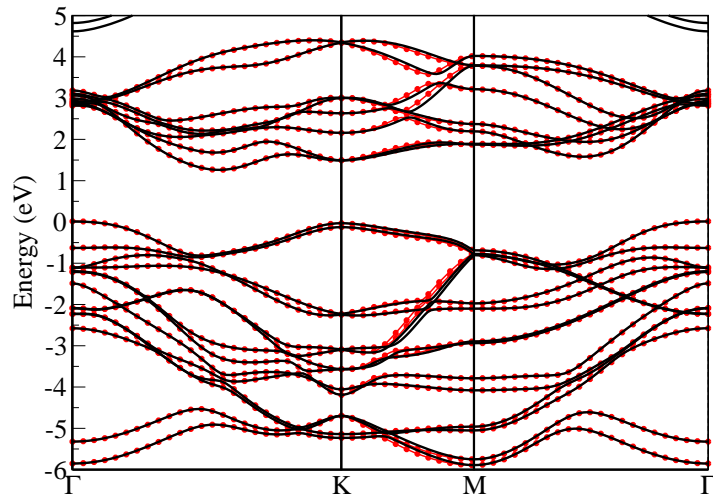


Figure 7.9: Comparison of *ab-initio* band dispersions (black solid line) for bilayer MoSe<sub>2</sub> at its experimental lattice constant, using GGA potentials and the fitted tight binding bands (line with red circle), using a basis consisting of Mo *d* and Se *p* states. Here the radial part of the tight binding basis functions correspond to maximally localized Wannier functions. The zero of energy is the valence band maximum.

Table 7.1: Onsite energies obtained from tight binding fitting of the *ab-initio* band structure a basis consisting of Mo *d* and Se *p* for monolayer and bilayer MoSe<sub>2</sub>. The respective Se *p<sub>x</sub>* is taken as reference for this energies and these in eV.

Orbitals	Monolayer MoSe <sub>2</sub>	Bilayer MoSe <sub>2</sub>
Se- $E_{p_x}$	0.00	+0.01
Se- $E_{p_y}$	0.00	0.0
Se- $E_{p_z}$	-0.33	-0.38
Mo- $E_{d_{xy}}$	+1.46	+1.51
Mo- $E_{d_{yz}}$	+2.28	+2.31
Mo- $E_{d_{zx}}$	+2.28	+2.31
Mo- $E_{d_{x^2-y^2}}$	+1.46	+1.52
Mo- $E_{d_{z^2}}$	+1.20	+1.27

switching off the inter-layer interaction, the band structure of the bilayer almost exactly matches with the band structure of monolayer MoSe<sub>2</sub> shown in Fig. 7.10. The lowest unoccupied band at the **T** point is raised by 0.25 eV and as a consequence of this, the energy difference of lowest unoccupied band at **K** and the **T** point is found to be -0.016 eV shown in Fig. 7.10 was 0.234 eV including the inter-layer interaction of bilayer MoSe<sub>2</sub>. which is very close to the above mentioned energy difference in the case of monolayer MoSe<sub>2</sub> (-0.031 eV). For further analysis, all the onsite energies in the real space Hamiltonian of bilayer MoSe<sub>2</sub> are replaced by the respective onsite energies of monolayer MoSe<sub>2</sub> and this brings about further movement of lowest unoccupied band at **T** point in the the upward direction by 0.019 eV. Hence, the above mentioned energy difference becomes -0.033 eV which is almost exactly equal to that energy difference in monolayer MoSe<sub>2</sub>. These analysis of bilayer MoSe<sub>2</sub> confirm that the crossover from direct to indirect band gap in MoSe<sub>2</sub> as a function of thickness is dominantly driven by the effect of the inter-layer interaction ( $\sim 92\%$ ) with a very small ( $\sim 8\%$ ) effect of charge transfer.

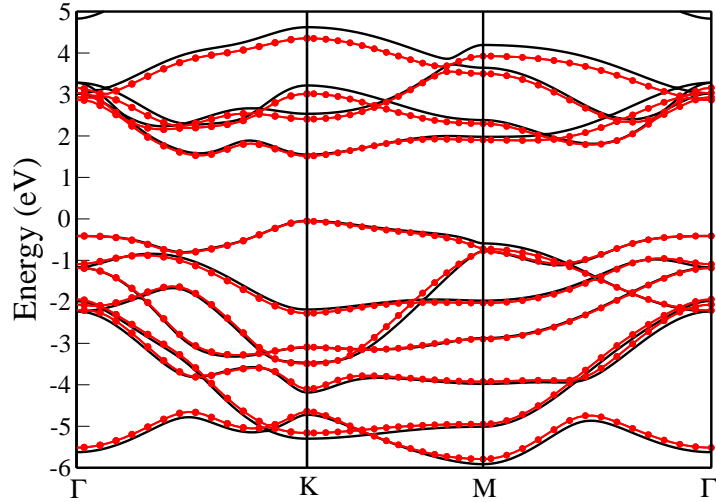


Figure 7.10: Comparison of *ab-initio* band dispersion of monolayer MoSe<sub>2</sub> (black solid line) at its experimental lattice constant, using GGA potentials and band structure of bilayer MoSe<sub>2</sub> (red line) when the inter-layer hopping interactions are switched off. The zero of energy is the valence band maximum.

Closer analysis reveals that the extracted hopping interaction strengths from these tight binding fitting of monolayer and bilayer MoSe<sub>2</sub> have a complicated distance dependence which do not allow a mapping onto a set of Slater-Koster parameters. To determine the appropriate inter-layer hopping interaction strengths of bilayer MoSe<sub>2</sub>, we consider a tight binding model with Mo *s, p, d* and Se *s, p, d* states in the basis. The onsite energies of bilayer MoSe<sub>2</sub> listed in Table 7.1, are considered in this model and are kept as fixed parameters. The hopping interaction strengths determined from the tight binding fitting of monolayer MoSe<sub>2</sub> [28] are used as the in-plane hopping parameters for this model and are also kept fixed as the in-plane environment is same for monolayer and bilayer. Now, the inter-layer hopping interaction strengths for Mo-Mo, Mo-Se and Se-Se are determined by a least-square-error minimization process. A comparison of the band structure from the tight binding fitting calculation with the band structure from *ab-initio* are shown in Figs. 7.11 and 7.12 for both monolayer [28] and bilayer MoSe<sub>2</sub> respectively. From the Figs. 7.11 and 7.12, this can be seen that the description of the minimal tight binding model is reasonable. The inter-layer hopping interaction strengths from this model are listed

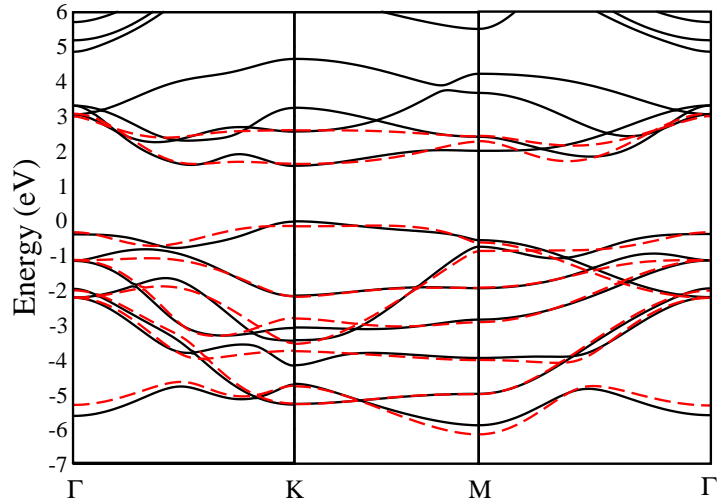


Figure 7.11: Comparison of *ab-initio* band dispersions (black solid line) for monolayer MoSe<sub>2</sub> at its experimental lattice constant using GGA potentials and the fitted tight binding bands (red dashed line), using a basis consisting of Mo *s,p,d* and Se *s,p,d* states. The zero of energy is the valence band maximum.

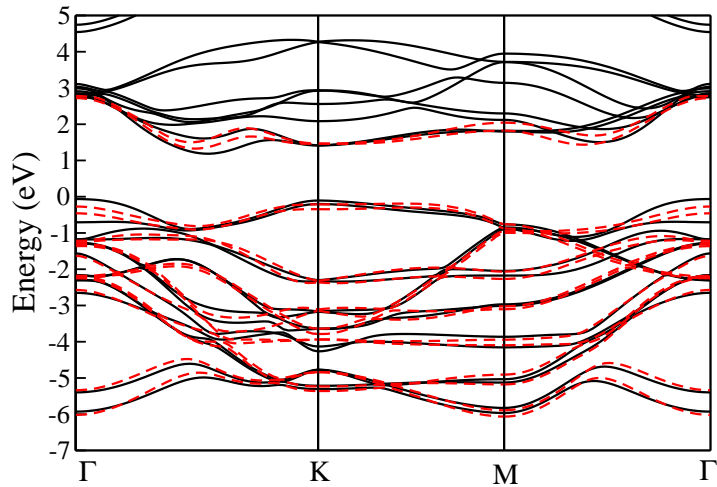


Figure 7.12: Comparison of *ab-initio* band dispersions (black solid line) for bilayer MoSe<sub>2</sub> at its experimental lattice constant using GGA potentials and the fitted tight binding bands (red dashed line), using a basis consisting of Mo *s,p,d* and Se *s,p,d* states. The zero of energy is the valence band maximum.

Table 7.2: Parameters obtained from least-square-error fitting of the *ab-initio* band structure onto a tight binding model using *s, p, d* orbitals of Mo and Se for bilayer MoSe<sub>2</sub>. The radial part of the tight binding basis functions correspond to maximally localized Wannier functions. The distances between the neighbors are given in brackets in unit of Å. The energies (E) are in eV.

	E(Mo,Se)(5.88)	E(Se,Se)(3.72)	E(Se,Se)(4.97)	E(Se,Se)(5.93)
<i>ppσ</i>	0.00	0.45	0.02	0.01
<i>ppπ</i>	0.00	-0.04	-0.00	-0.01
<i>pdσ</i>	-0.94	0.00	0.00	0.00
<i>pdπ</i>	0.10	0.00	0.00	0.00
<i>dpσ</i>	0.25	0.00	0.00	0.00
<i>dpπ</i>	-0.01	0.00	0.00	0.00

in Table 7.2. So, this shows that direct to indirect band gap crossover in MoSe<sub>2</sub> as a function of thickness can be described in terms of scaling of the interaction according to Harrison's law.

Similar analysis has been done for MoS<sub>2</sub> which has the structure same as MoSe<sub>2</sub>. In the optimized structure of bilayer, the shortest in-plane Mo-S and Mo-Mo (S-S) distances are 2.41 Å and 3.16 Å respectively. The inter-layer distance obtained from the optimization with vdW interaction is 3.14 Å. The *ab-initio* band dispersions of monolayer and bilayer MoS<sub>2</sub> with GGA are plotted along various symmetry directions in Figs. 7.13 and 7.14.

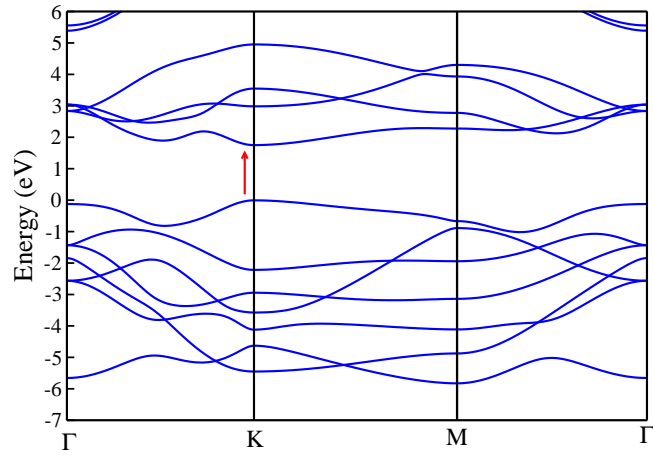


Figure 7.13: The *ab-initio* band dispersion for monolayer MoS<sub>2</sub> at its experimental lattice constant using GGA potentials. The arrow indicates that band gap is direct. The zero of energy is the valence band maximum.

Similar to the case of monolayer MoSe<sub>2</sub>, Fig. 7.13 show that monolayer MoS<sub>2</sub>, is a direct band gap semiconductor with both the VBM and CBM at **K** point using GGA as exchange-correction functional. The obtained band gap from our calculation is 1.76 eV which is almost close to the experimental band gap of 1.9 eV [11]. On the other hand, bilayer MoS<sub>2</sub> has an indirect band gap of 1.37 eV with the VBM and CBM at  $\Gamma$  and **T** points respectively shown in 7.14 using GGA. The band structure of bilayer MoS<sub>2</sub> with LDA shown in Fig. 7.15 is qualitatively same as with GGA.

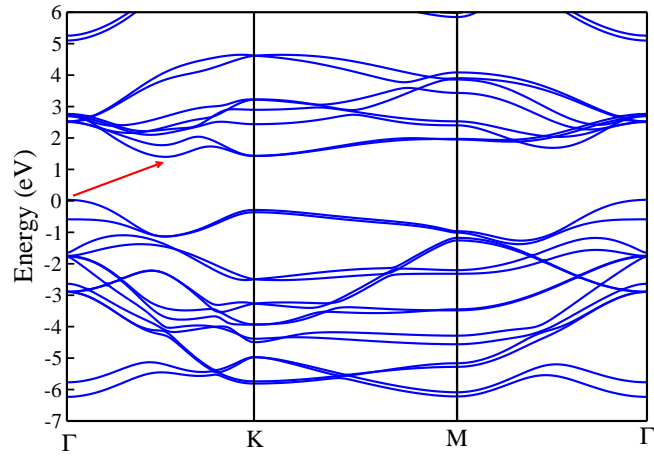


Figure 7.14: The *ab-initio* band dispersion for bilayer MoS<sub>2</sub> at its experimental lattice constant using GGA potentials. The arrow indicates that band gap is indirect. The zero of energy is the valence band maximum.

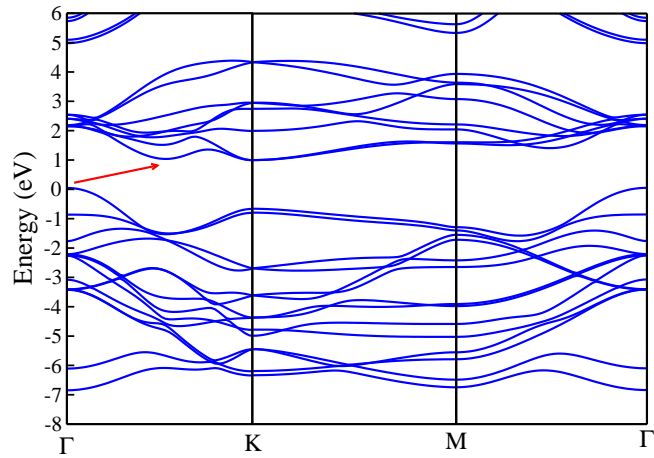


Figure 7.15: The *ab-initio* band dispersion for bilayer MoS<sub>2</sub> at its experimental lattice constant using LDA potentials. The arrow indicates that band gap is indirect. The zero of energy is the valence band maximum.

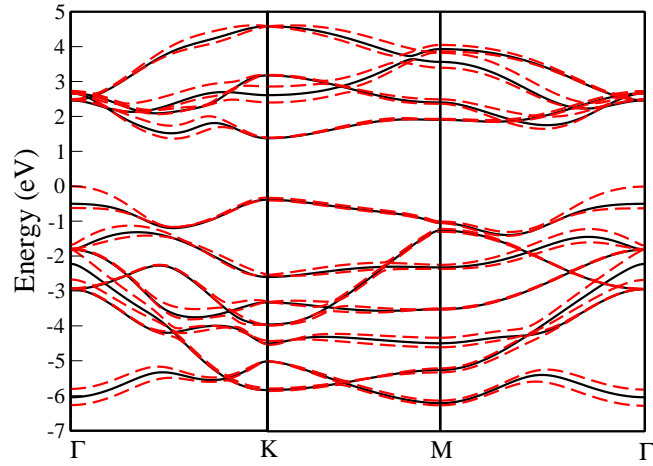


Figure 7.16: Comparison of *ab-initio* band dispersions for monolayer MoS<sub>2</sub> (black solid line) and bilayer MoS<sub>2</sub> (red dashed line) at its experimental lattice constant using GGA potentials. The zero of energy is the valence band maximum.

The comparison of *ab-initio* band dispersions of monolayer and bilayer MoS<sub>2</sub> is plotted along various symmetry directions in Fig. 7.16. Similar to MoSe<sub>2</sub>, these two band structures of MoS<sub>2</sub> are matching with each other almost in every directions except at the positions of VBM and CBM which implies that the inter-layer interactions are very weak. The Fig. 7.16 show that the difference of lowest unoccupied bands at **K** and the **T** point is found to be -0.149 eV and 0.031 eV for monolayer and bilayer MoS<sub>2</sub> respectively.

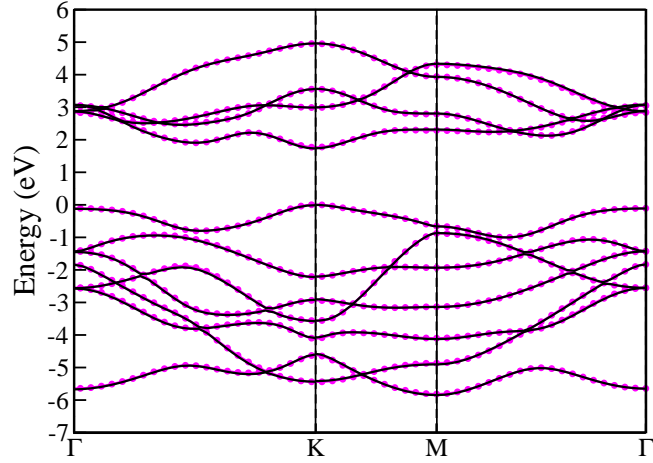


Figure 7.17: Comparison of *ab-initio* band dispersions (black solid line) for monolayer MoS<sub>2</sub> at its experimental lattice constant, using GGA potentials and the fitted tight binding bands (line with red circle), using a basis consisting of Mo *d* and S *p* states. Here the radial part of the tight binding basis functions correspond to maximally localized Wannier functions. The zero of energy is the valence band maximum.

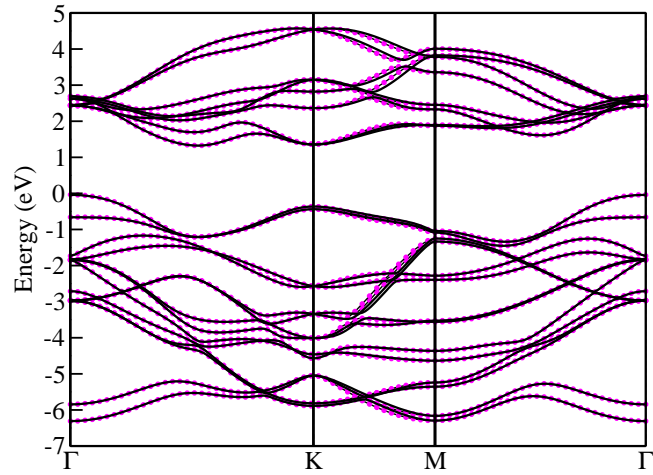


Figure 7.18: Comparison of *ab-initio* band dispersions (black solid line) for bilayer MoS<sub>2</sub> at its experimental lattice constant, using GGA potentials and the fitted tight binding bands (line with red circle), using a basis consisting of Mo *d* and S *p* states. Here the radial part of the tight binding basis functions correspond to maximally localized Wannier functions. The zero of energy is the valence band maximum.

The *ab-initio* band structures fitted with tight binding model considering Mo *d* and S *p* Wannier functions as basis functions for monolayer [35] and bilayer MoS<sub>2</sub> are plotted along various symmetry directions in Figs. 7.17 and 7.18. Now, similar to MoSe<sub>2</sub>, to quantify the effect of inter-layer interactions, those interactions are switched off in the real space Hamiltonian. As expected, after switching off the inter-layer interactions, the band structure of the bilayer almost exactly matches with the band structure of monolayer MoS<sub>2</sub> shown in Fig. 7.19. This results from a movement of the lowest unoccupied band in upward direction at the **T** point by

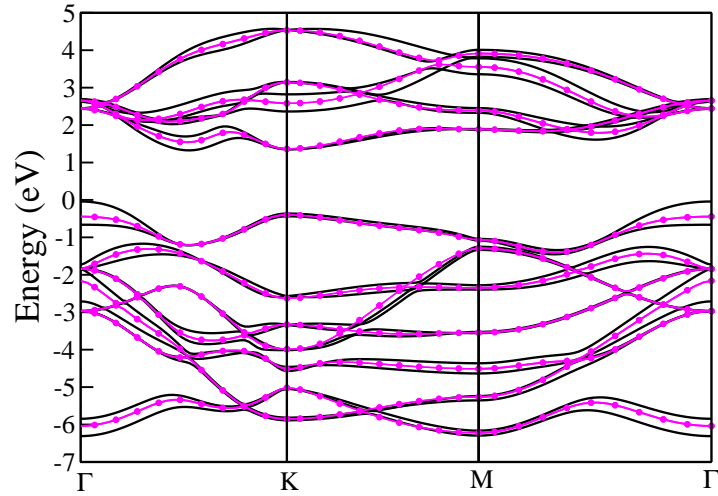


Figure 7.19: Comparison of *ab-initio* band dispersion (red dashed line) for monolayer MoS<sub>2</sub> at its experimental lattice constant, using GGA potentials and the bilayer bands (magenta line) when the inter-layer hopping interactions are switched off. The zero of energy is the valence band maximum.

the amount of 0.168 eV of bilayer MoS<sub>2</sub> shown in Fig. 7.19. The CBM is then shifted from the point **T** to **K**. The above mentioned energy difference in bilayer MoS<sub>2</sub> almost reaches the value of -0.137 eV which is very close to the above mentioned energy difference in monolayer MoS<sub>2</sub> (-0.149 eV). So, these analysis confirms that inter-layer interaction alone is able to drive the direct to indirect band gap transformation in MoS<sub>2</sub> as a function of thickness whereas the quantum confinement effect hardly plays any role.

## 7.4 Conclusion

We have examined the electronic structure of a monolayer as well as a bilayer of MoSe<sub>2</sub> and MoS<sub>2</sub>. Considering a tight binding model we are able to reproduce the band structure calculated within *ab-initio* calculations. Using the extracted parameters, we are able to predict the contribution from inter-layer interactions and charge transfer effects leading to the crossover from direct to indirect band gap as a function of thickness.

# Bibliography

- [1] G. Eda and S. A. Maier, *ACS Nano* **7**, 5660 (2013).
- [2] Q. H. Wang, K. Kalantar-Zadeh, A. Kis *et al.*, *Nat. Nanotechnol.* **7**, 699 (2012).
- [3] W. K. Ho, J. C. Yu, J. Lin *et al.*, *Langmuir* **20**, 5865 (2004).
- [4] E. Fortin and W. Sears, *J. Phys. Chem. Solids* **43**, 881 (1982).
- [5] J. N. Coleman, M. Lotya, A. O'Neill *et al.*, *Science* **331**, 568 (2011).
- [6] R. C. Jin, Y. W. Cao, C. A. Mirkin *et al.*, *Science* **294**, 1901 (2001).
- [7] M. B. Sigman, A. Ghezelbash, T. Hanrath *et al.*, *J. Am. Chem. Soc.* **125**, 16050 (2003).
- [8] S. Ithurria, M. D. Tessier, B. Mahler *et al.*, *Nature Mater.* **10**, 936 (2011).
- [9] G. L. Frey, S. Elani, M. Homyonfer *et al.*, *Phys. Rev. B* **57**, 6666 (1998).
- [10] S. Tongay, J. Zhou, C. Ataca *et al.*, *Nano Lett.* **12**, 5576 (2012).
- [11] K. F. Mak, C. Lee, J. Hone *et al.*, *Phys. Rev. Lett.* **105**, 136805 (2010).
- [12] W. Jin, P.-C. Yeh, N. Zaki *et al.*, *Phys. Rev. Lett.* **111**, 106801 (2013).
- [13] T. Böker, R. Severin, A. Müller *et al.*, *Phys. Rev. B* **64**, 235305 (2001).
- [14] J. S. Ross, S. Wu, H. Yu *et al.*, *Nat. Commun.*, **4**, 1474 (2013).
- [15] X. Qian, J. Liu, L. Fu and J. Li, arXiv:1406.2749 (2014).

- [16] A. Kuc, N. Zibouche and T. Heine, Phys. Rev. B **83**, 245213 (2011).
- [17] J. E. Padilha, H. Peelaers, A. Janotti *et al.*, Phys. Rev. B **90**, 205420 (2014).
- [18] L. Zhang and A. Zunger, Nano Lett. **15**, 949 (2015).
- [19] G. Kresse and J. Furthmüller, Phys. Rev. B **54**, 11169 (1996).
- [20] Q. Liu, L. Li, Y. Li *et al.*, J. Phys. Chem. C, **116**, 21556 (2012).
- [21] A. A. Al-Hilli and B. L. Evans, J. Cryst. Growth **15**, 93 (1972).
- [22] G. Kresse and D. Joubert, Phys. Rev. B **59**, 1758 (1999).
- [23] P.E. Blöchl, Phys. Rev. B **50**, 17953 (1994).
- [24] J. Paier, R. Hirschl, M. Marsman *et al.*, J. Chem. Phys. **122**, 234102 (2005).
- [25] S. Grimme, J. Comput. Chem. **27**, 1787 (2006).
- [26] A. A. Mostofi, J. R. Yates, Y.-S. Lee *et al.*, Comput. Phys. Commun. **178**, 685 (2008).
- [27] C. Franchini, R. Kováčik, M. Marsman *et al.*, J. Phys.: Condens. Matter **24**, 235602 (2012).
- [28] R. Das and P. Mahadevan, Pramana-J. Phys. **84**, 1033 (2015).
- [29] P. Mahadevan, N. Shanthi and D. D. Sarma, Phys. Rev. B **54**, 11199 (1996).
- [30] W A Harrison, *Electronic structure and the properties of solids: The physics of the chemical bond* (Dover, New York, USA, 1967).
- [31] L. Liu, S. B. Kumar, Y. Ouyang *et al.*, IEEE Trans. Electron Devices **58**, 3042 (2011).
- [32] L. Debbichi, O. Eriksson and S. Lebègue, Phys. Rev. B **89**, 205311 (2014).
- [33] A. J. Bradley, M. M. Ugeda, F. H. da Jornada *et al.*, Nano Lett. **15**, 2594 (2015).
- [34] S. W. Han, H. Kwon and S. Keun Kim, Phys. Rev. B **84**, 045409 (2011).
- [35] R. Das, B. Rakshit, S. Debnath *et al.*, Phys. Rev. B **89**, 115201 (2014).

